

71-26,261

BOYKIN, Wilber Ray, 1933-
LOW ENERGY SCATTERING OF ^3He AND ^4He FROM A
POLARIZED ^3He GAS TARGET.

Rice University, Ph.D., 1971
Physics, nuclear

University Microfilms, A XEROX Company, Ann Arbor, Michigan

RICE UNIVERSITY

Low Energy Scattering of ^3He and ^4He
from a Polarized ^3He Gas Target

by

Wilber Ray Boykin

A THESIS SUBMITTED
IN PARTIAL FULFILLMENT OF THE
REQUIREMENTS FOR THE DEGREE OF

Doctor of Philosophy

Thesis Director's signature:

Stephen D. Baker

Houston, Texas

May, 1971

To

Mary Ann

Timothy and Melissa

Table of Contents

	Page
I. Introduction	
A. Summary of Recent Experiments Involving ^3He - ^4He and ^3He - ^3He Scattering	1
B. Preview of the Experiment	8
II. Experimental Apparatus	
A. Optical Pumping	
1. Brief Theory of Optical Pumping	11
2. Optical Pumping Apparatus	14
B. Target Cell	
1. Target Cell Description	15
2. Entrance Foil and Target Energy Loss Corrections	18
3. Target Cell Cleaning and Filling	19
C. Detectors and Electronics	21
III. Experimental Results	
A. Optically Measured Target Polarization	23
B. Elastic Scattering of ^4He from a Polarized ^3He Gas Target	
1. Experimental Asymmetry and Reaction Analyzing Power	29
2. Phase Shift Analysis of the ^3He - ^4He Elastic Scattering Data	
a. Method	38
b. Initial Conditions for the Phase Shift Searches	42
c. Discussion of the Phase Shifts	43
d. Effect of Polarization Data on the Phase Shift Analysis	49

	Page
e. Effect of Systematic Cross Section and Polarization Data Errors on the Phase Shifts	50
3. Nuclear Level Parameters	51
C. Scattering of ^3He from a Polarized ^3He Gas Target	
1. ^3He - ^3He Elastic Scattering	57
2. ^3He - ^3He Inelastic Scattering	58
IV. Conclusions and Suggestions for Future Work . .	66
APPENDIX A. Optical Measurement of Target Polarization	
1. Method	A1
2. Calculation of p from $\langle \delta I / I \rangle$	A9
3. Discussion of Optical Pumping Parameters .	A10
APPENDIX B. Experimental Asymmetries	
1. General Information	B1
2. Calculation of Experimental Asymmetry A . .	B4
3. Instrumental Asymmetry A_0	B8
4. Magnetic Field Asymmetry A_M	B9
5. Modified Solid Angle Asymmetry $A_{\Omega M}$	B10
6. Weighted Average and Weighted Average Error for Duplicate Measurements	B11
7. Background Correction	B12
APPENDIX C. Phase Shift Analysis: Elastic Scattering of Charged Spin $\frac{1}{2}$ Particles from Spin 0 Particles	
1. Differential Cross Section Equations . . .	C1
2. Spin Polarization Equations	C14

	Page
APPENDIX D. Single Level Parameterization of the Phase Shifts	
1. Variational Method for Determining the Theoretical Phase Shifts	D1
2. Calculation of the Phase Shifts from the Parameter Vector $\vec{P} = \vec{P}(\gamma^2, E_R, r)$ and the Solutions to the Schroedinger Equation	
a. Solutions to Schroedinger Equation . . .	D6
(1). Vanishing Coulomb Field	D7
(2). Nonvanishing Coulomb Field and ρ Small	D9
(3). Nonvanishing Coulomb Field and ρ Large	D11
b. Calculation of Theoretical Phase Shifts	D15
APPENDIX E. Results of Some Optical Pumping Tests on Cells Containing Aluminum and Brass Parts	E1
APPENDIX F. Energy Calibration for the Experiment .	F1
References	S1
Acknowledgements	S7

List of Figures

Figure No.	Page
1. Partial Energy Level Diagram of ${}^3\text{He}$ Atom . . .	12
2a. Reaction Analyzing Power for ${}^3\vec{\text{He}}({}^4\text{He}, {}^4\text{He}){}^3\text{He}$, $\theta_{\text{cm}} = 71.6^\circ$	33
2b. Reaction Analyzing Power for ${}^3\vec{\text{He}}({}^4\text{He}, {}^3\text{He}){}^4\text{He}$, $\theta_{\text{cm}} = 120.0^\circ$	34
3. Contour Map of ${}^3\text{He}$ Spin Polarization	37
4. χ^2 vs. $P_{3/2}$ Phase Shift, $E_{{}^3\text{He lab}} = 4.64 \text{ MeV}$.	40
5. $S_{1/2}$ Phase Shift for ${}^3\vec{\text{He}}({}^4\text{He}, {}^4\text{He}){}^3\text{He}$	45
6. P-wave Phase Shifts for ${}^3\vec{\text{He}}({}^4\text{He}, {}^4\text{He}){}^3\text{He}$. . .	46
7. $F_{5/2}$ Phase Shift for ${}^3\vec{\text{He}}({}^4\text{He}, {}^4\text{He}){}^3\text{He}$	47
8. $F_{7/2}$ Phase Shift for ${}^3\vec{\text{He}}({}^4\text{He}, {}^4\text{He}){}^3\text{He}$	48
9. Contours of Constant χ^2 Used to Determine ${}^2P_{1/2}$ Level Parameters in ${}^7\text{Be}$	55
10. Contours of Constant χ^2 Used to Determine ${}^2P_{3/2}$ Level Parameters in ${}^7\text{Be}$	56
11. Reaction Analyzing Power for ${}^3\vec{\text{He}}({}^3\text{He}, {}^3\text{He}){}^3\text{He}$, $\theta_{\text{cm}} = 60.0^\circ$	63
12. Reaction Analyzing Power for ${}^3\vec{\text{He}}({}^3\text{He}, p){}^5\text{Li}$ (ground state), $\theta_{\text{lab}} = 30.0^\circ$	64
13. Optical Pumping Light Level Diagram	A4
14. Idealized Optical Pumping Signals	A5
15. Scattering Geometry for Polarized Target Experiments	B3
16. Spectrum with Level Background	B13

List of Tables

Table No.	Page
1. Target Polarization Data for ${}^3\text{He}({}^4\text{He}, {}^4\text{He}){}^3\text{He}$	25
2. Target Polarization Data for ${}^3\text{He}({}^3\text{He}, {}^3\text{He}){}^3\text{He}$	26
3. Target Polarization Data for ${}^3\text{He}({}^3\text{He}, p){}^5\text{Li}$ (ground state)	28
4a. Experimental Asymmetry and Reaction Analyzing Power for ${}^3\text{He}({}^4\text{He}, {}^4\text{He}){}^3\text{He}$, $\theta_{\text{cm}} = 71.6^\circ$. . .	31
4b. Experimental Asymmetry and Reaction Analyzing Power for ${}^3\text{He}({}^4\text{He}, {}^3\text{He}){}^4\text{He}$, $\theta_{\text{cm}} = 120.0^\circ$. . .	32
5. S, P, and F Phase Shifts and Errors for ${}^3\text{He}({}^4\text{He}, {}^4\text{He}){}^3\text{He}$	44
6. Nuclear Level Parameters for ${}^2\text{P}_{1/2}$ and ${}^2\text{P}_{3/2}$ States in ${}^7\text{Be}$	54
7. Experimental Asymmetry and Reaction Analyzing Power for ${}^3\text{He}({}^3\text{He}, {}^3\text{He}){}^3\text{He}$, $\theta_{\text{cm}} = 60.0^\circ$. . .	60
8. Experimental Asymmetry and Reaction Analyzing Power for ${}^3\text{He}({}^3\text{He}, p){}^5\text{Li}$ (ground state), $\theta_{\text{lab}} = 30.0^\circ$	62
9. Relative Electric Dipole Transition Probabilities Between Magnetic Sublevels $2{}^3\text{S}_1 - 2{}^3\text{P}_0$ in ${}^3\text{He}$	A11
10. Constants Used in Computing Target Polarization	A11
11. Numbers of Scattered Particles as a Function of Magnetic Field Direction, Target Polarization Direction, and Scattering Angle	B6
12. Vector Addition Coefficients for Spin $\frac{1}{2}$ + Spin 0	C12

I. INTRODUCTION

A. Summary of Recent Experiments Involving ^3He - ^4He and ^3He - ^3He Scattering

A summary of experiments in recent years which utilized polarized beams and targets has been given in an earlier work.¹⁾ The present discussion is intended to reference the majority of the ^3He - ^4He and ^3He - ^3He scattering experiments over approximately the past two decades and will be presented in more or less chronological order. In many cases an experiment covered several reactions and in such instances only the pertinent reactions will be cited.

Early ^3He - ^4He experiments were directed toward determination of differential cross sections and investigation of states in the compound nucleus ^7Be . Frequently phase shift analyses were reported for the ^3He - ^4He scattering. Work commenced on inelastic ^3He - ^4He reactions in later years and has since turned toward use of ^3He - ^4He reactions as polarization analyzers.

Such an example of the early work was that of Miller and Phillips²⁾ who scattered ^3He from ^4He at ^3He bombarding energies of 3.0 to 5.5 MeV. They report phase shifts similar to those of later authors but their p-wave splitting is $p_{1/2} > p_{3/2}$, the opposite of that in subsequent articles.^{15,16)} Phillips and Miller³⁾ give the first polarization map for ^3He particles scattered from the reaction $^4\text{He}(^3\text{He}, ^3\text{He})^4\text{He}$ in the 3.0-5.5 MeV bombarding energy range. It should also be noted that the sign of the polarization reported by Phillips

and Miller is opposite to the Basel Convention.⁴⁾ Another reference, Chiba et al.,⁵⁾ reports scattering ^4He from ^3He at bombarding energies of 27.5 to 32.0 MeV.

Phillips et al.⁶⁾ have reported the first use of a polarized ^3He gas target in a nuclear scattering experiment, $^3\text{He}(^4\text{He}, ^4\text{He})^3\text{He}$. Their target was polarized by the method of optical pumping, which has been reported in the literature.⁷⁻⁹⁾ Tombrello and Parker¹⁰⁾ have scattered ^3He from ^4He over the ^3He bombarding energy range of 4 to 12 MeV. They report a very small p-wave splitting and it, like that of Miller and Phillips,²⁾ is $p_{1/2} > p_{3/2}$. They also give the results of a single level parameterization of the $^2\text{F}_{5/2}$ state in ^7Be and a polarization map calculated from the derived phase shifts.

Holmgren and Johnson¹¹⁾ have measured the total cross section for the $^3\text{He}(^4\text{He}, \gamma)^7\text{Be}$ reaction over the 480-1320 keV bombarding energy range and have derived expressions for the cross section in terms of the bombarding energy. Parker and Kavanagh¹²⁾ also used the reaction $^3\text{He}(\alpha, \gamma)^7\text{Be}$ with mono-energetic α -particles between 0.42 and 5.80 MeV to determine the total capture cross section and the branching ratio between the cascade and the crossover transitions as functions of energy. Tombrello and Parker¹³⁾ have used the ^3He - ^4He elastic scattering phase shifts to compute a theoretical cross section for the reaction $^3\text{He}(\alpha, \gamma)^7\text{Be}$. They report good agreement with experiment. Nagatani et al.¹⁴⁾ have measured the absolute cross section for the $^3\text{He}(\alpha, \gamma)^7\text{Be}$ reaction at

center-of-mass energies between 164 and 225 keV and report agreement with the results of Parker and Kavanagh.¹²⁾

Barnard et al.¹⁵⁾ report the scattering of ^3He from ^4He in the ^3He bombarding energy range of 2.5 to 5.7 MeV. They found two sets of phase shifts which differed only in the p-wave splitting, though both sets fit their data about equally well. Differential cross sections and a polarization map are also given, along with parameters for the ground and first two excited states in ^7Be . Spiger and Tombrello¹⁶⁾ have also scattered ^3He from ^4He for bombarding energies between 5 and 18 MeV. They report differential cross section data, a phase shift analysis, and a polarization map. Parameters for several states in ^7Be and ^7Li are also given. Their phase shifts agree with those of the present work ($p_{3/2} > p_{1/2}$). Early phase shift analyses of ^3He - ^4He elastic scattering gave the opposite p-wave splitting.^{2,10)}

Ivanovich et al.¹⁷⁾ report differential cross section data for the reaction $^3\text{He}(\alpha, \alpha)^3\text{He}$ for α -bombarding energies of 5.9 to 7.9 MeV. They have also deduced resonance parameters for the $^2F_{7/2}$ levels in ^7Be and ^7Li .

Schwandt et al.¹⁸⁾ have elastically scattered ^3He from ^4He for ^3He bombarding energies between 27.2 and 42.8 MeV. They have compared the results of their phase shift analysis with the predictions of the resonating group method and report that the resonating group method only qualitatively describes ^3He - ^4He elastic scattering near 40 MeV. Bacher et al.¹⁹⁾ and Jacobs and Brown²⁰⁾ have elastically scattered

^3He from ^4He over a large angular region at ^3He bombarding energies of 18-70 MeV and 17.8-30 MeV, respectively. Brown and co-workers²¹⁾ have measured the energy dependence of the $^3\text{He}+^4\text{He}$ differential cross section at $\theta_{\text{cm}} = 173.2^\circ$ and have observed a resonance structure similar to that predicted by resonating group calculations. Vincent et al.²²⁾ have elastically scattered 42 MeV α -particles from ^3He to measure the differential cross section over the angular range of $\theta_{\text{cm}} = 20^\circ$ to 170° . Cahill and Martens²³⁾ report a similar experiment for α -particle energies between 43.4 and 58.2 MeV.

Armstrong et al.²⁴⁾ used a double scattering experiment to measure the polarization of ^3He elastically scattered from ^4He for ^3He bombarding energies between 7.8 and 13.0 MeV. They report several regions of large ^3He polarization.

Hardy et al.²⁵⁾ have scattered ^4He from a ^3He gas target which was polarized by the method of optical pumping. They report good agreement with the results of reference 24). A polarization map based on their derived phase shifts is also given. The equivalent ^3He laboratory energy range was 5.7 to 13.5 MeV. "Equivalent ^3He laboratory energy" is defined as the ^4He bombarding energy (after corrections for energy loss in the target entrance foil) multiplied by the ratio of the ^3He mass to that of ^4He and is written " $E_{^3\text{He lab}}$."

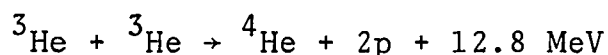
There are two other references to ^3He and ^4He scattering from polarized ^3He targets, Hardy et al.²⁶⁾ and Boykin, Baker, and Hardy.²⁷⁾ These two experiments were performed

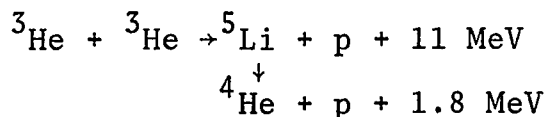
in the equivalent ^3He laboratory energy range of 3.3 to 13.5 MeV.

McEver et al.²⁸⁾ report a double scattering experiment at $E_{^4\text{He}} = 17.3$ MeV similar to that of reference 24) in which ^4He particles are scattered from a ^3He gas target. The recoiling ^3He particles then undergo a second scattering from a ^4He gas target. Both references 24) and 28) suggest the use of this double scattering technique as a polarization analyzer in nuclear scattering experiments.

In the several ^3He - ^4He experiments reported here it should be kept in mind that only two, references 6) and 25-26) used a polarized ^3He target. Phillips²⁹⁾ has given a summary of experiments reported through 1965 which used polarized ^3He targets. Some of these experiments utilized neutrons and protons as projectiles.

Early work in ^3He - ^3He scattering was directed toward determining decay modes in ^3He - ^3He capture and total capture cross section. Some measurements of differential elastic cross sections have been made. Later work has concentrated quite heavily on inelastic reactions in search of information about the existence of the diproton. Good et al.³⁰⁾ appear to have reported the first experiment indicating the decay modes resulting from ^3He - ^3He capture. Their experiment was carried out at a ^3He bombarding energy of 300 keV and suggested the following:





Almgvist and co-workers³¹⁾ report observing the two ${}^3\text{He}$ particles break up into a ${}^5\text{Li}$ particle and a proton for a ${}^3\text{He}$ bombarding energy of 240 keV. Good et al.³²⁾ have extended the results of their previous study of ${}^3\text{He}$ - ${}^3\text{He}$ capture to 800 keV and confirm the two modes of disintegration for the compound nucleus.

Bredin et al.³³⁾ have elastically scattered ${}^3\text{He}$ from ${}^3\text{He}$ at the center-of-mass energies of 12.7 and 14.35 MeV and have also done some work on the inelastic reaction ${}^3\text{He}({}^3\text{He}, \text{p}){}^5\text{Li}$ (ground state). Bransden and Hamilton³⁴⁾ have performed ${}^3\text{He}$ - ${}^3\text{He}$ elastic scattering at laboratory energies of 20-29 MeV. Gammel et al.³⁵⁾ and Leland et al.³⁶⁾ have measured the differential cross sections for ${}^3\text{He}+{}^3\text{He}$ elastic scattering at 20 and 25 MeV bombarding energy and 12-25 MeV, respectively. Tombrello and Bacher³⁷⁾ have measured differential cross sections for ${}^3\text{He}$ - ${}^3\text{He}$ elastic scattering between 3 and 12 MeV bombarding energy. Ivanovich et al.¹⁷⁾ also give differential cross section for ${}^3\text{He}$ - ${}^3\text{He}$ elastic scattering at 9 and 11 MeV bombarding energy. Similar measurements were made by Van Nen-Min et al.³⁸⁾ in the 500-1700 keV bombarding energy range. Bacher et al.³⁹⁾ give the differential cross sections for ${}^3\text{He}$ - ${}^3\text{He}$ elastic scattering between 18 and 80 MeV for a number of angles. Bacher and co-workers⁴⁰⁾ have compared their experimental ${}^3\text{He}$ - ${}^3\text{He}$ differential cross sections with the results of the

resonating group method and report good agreement between 11.9 and 18.9 MeV. Jenkin et al.⁴¹⁾ have also measured the differential cross section for ${}^3\text{He}$ - ${}^3\text{He}$ elastic scattering between 17.9 and 32.0 MeV at several angles.

In recent years quite a few articles have appeared based on the reaction ${}^3\text{He}({}^3\text{He}, 2p){}^4\text{He}$. From data taken at 15 MeV bombarding energy, Zurmuhle⁴²⁾ reports that this reaction proceeds predominantly through the ground state and first excited state of ${}^5\text{Li}$. He found no evidence for a strong p-p final state interaction. Aldridge et al.⁴³⁾ also report evidence that this reaction decays through the ${}^5\text{Li}$ ground state. Their data were taken at 4.90 MeV bombarding energy. Bacher and Tombrello⁴⁴⁾ have also observed the ${}^3\text{He}({}^3\text{He}, 2p){}^4\text{He}$ reaction at 3-18 MeV ${}^3\text{He}$ bombarding energy. Blackmore and Warren⁴⁵⁾ have also performed this experiment at 1.15 and 5 MeV ${}^3\text{He}$ incident energy in an attempt to see the p-p final state interaction. In a subsequent article⁴⁶⁾ these authors report observing the p-p final state interaction corresponding to the formation of the singlet state of the diproton. The ${}^3\text{He}$ laboratory energy in this latter experiment was 1.5 MeV.

In contrast to the ${}^3\text{He}({}^3\text{He}, 2p){}^4\text{He}$ experiments, Harrison et al.⁴⁷⁾ observed the reaction ${}^3\text{He} + {}^3\text{He} \rightarrow {}^6\text{Be}^* + \gamma$ at 90° for ${}^3\text{He}$ bombarding energies of 0.86 to 11.8 MeV. They report a total reaction cross section for transitions to the first excited state of ${}^6\text{Be}$ which varies smoothly from 0.4 to $9.3 \mu\text{b}$ over this energy range. Because of this low cross section

the authors conclude that this reaction is of negligible astrophysical importance compared to the ${}^3\text{He}({}^3\text{He}, 2p){}^4\text{He}$ reaction.

Artjomov and co-workers⁴⁸⁾ have observed the ${}^3\text{He}({}^3\text{He}, \alpha)2p$ reaction at a bombarding energy of 26 MeV. They report difficulty in understanding which process takes place in the reaction--the two particle quasi-stable system or the three particle final state interaction.

Slobodrian et al.⁴⁹⁾ report obtaining good fits to spectra from the ${}^3\text{He}({}^3\text{He}, \alpha)2p$ reaction at 43.7 and 53.0 MeV using p-p scattering parameters. In another article these same authors⁵⁰⁾ find that the ${}^3\text{He}+{}^3\text{He}$ reaction does not excite sharp states in ${}^3\text{He}$ with a differential cross section larger than 120 $\mu\text{b}/\text{sr}$ below 30 MeV excitation.

Tombrello and Slobodrian⁵¹⁾ state that the triton spectra obtained from ${}^3\text{He}({}^3\text{He}, t)3p$ at 44 MeV bombarding energy are featureless for laboratory angles between 6° and 25° . The spectra show no indication of either a 3p final state interaction or a strong sequential decay mode.

B. Preview of the Experiment

As reported in the foregoing summary, quite a lot of work has been done on both the ${}^3\text{He}-{}^4\text{He}$ and the ${}^3\text{He}-{}^3\text{He}$ reactions. Energy levels, though not discussed here, are fairly well known for both systems.⁵²⁾ Data on decay modes for compound nuclei formed by these reactions have been

compiled. Cross section data are available for a wide range of angles and energies.

With the two exceptions previously noted^{6,25,26)} all of the experiments involving ^3He - ^4He scattering used unpolarized targets. These two polarized target experiments covered only two laboratory angles (45° and 33°) and a limited equivalent ^3He laboratory energy range (4.9, 7.33 and 5.7-13.5 MeV). A phase shift analysis was performed in only the second experiment^{25,26)} and other phase shift analyses of ^3He - ^4He elastic scattering did not have the benefit of polarization data. To date there have been no reports of the scattering of ^3He from a polarized ^3He target.

In review of the small amount of data available for the scattering of ^3He and ^4He from a polarized ^3He target, the present experiment offered an opportunity to supplement and improve the existing data on these two reactions. The two primary objectives of the experiment were to determine the ^3He - ^4He elastic scattering phase shifts and to look for any polarization effects in ^3He - ^3He elastic scattering using, in both cases, a ^3He gas target polarized by the method of optical pumping.

The reactions observed were $^3\vec{\text{He}}(^4\text{He}, ^4\text{He})^3\text{He}$, $^3\vec{\text{He}}(^4\text{He}, ^3\text{He})^4\text{He}$ at equivalent ^3He laboratory energies of 3.30 to 6.86 MeV and $^3\vec{\text{He}}(^3\text{He}, ^3\text{He})^3\text{He}$, $^3\vec{\text{He}}(^3\text{He}, p)^5\text{Li}$ (ground state) at ^3He bombarding energies of 4.33 to 9.83 MeV. The energy values quoted have been corrected for entrance foil

losses. All data were taken at the laboratory angle of $30.0^\circ \pm 1.1^\circ$ rms deviation (computed in Section II.B.1.).

The results of the experiment were satisfying because there is reason to believe that the ^3He - ^4He elastic scattering phase shifts have been more precisely determined than in previous analyses. Reasonable errors have been assigned to the phase shifts. A single level parameterization of the derived p-wave phase shifts using R-matrix theory has given reasonable values of the nuclear reaction radius and ratio of the reduced width to the Wigner limit,⁵³⁾ along with errors in these quantities, for the ground state and first excited state in ^7Be . The experimental asymmetry (Appendix B.) for ^3He - ^4He elastic scattering at $\theta_{\text{cm}} = 71.6^\circ$ changes sign near the resonance at 5.2 MeV; at $\theta_{\text{cm}} = 120.0^\circ$ the asymmetry is small and generally slightly positive. The experimental asymmetry for the ^3He - ^3He elastic scattering at $\theta_{\text{cm}} = 60.0^\circ$ is small and approximately consistent with zero over the energy region studied. The experimental asymmetry for the breakup protons produced by the inelastic reaction $^3\text{He}(\vec{^3\text{He}}, p)^5\text{Li}$ (ground state) is not clearly defined and more data would be required in order to draw a definite conclusion.

The remainder of this thesis is divided into two main parts. The first (Chapters II-IV) is concerned with a description of the experiment and discussion of the data analysis and results, while the second part (Appendixes A-F) gives derivations of mathematical relations used in the analysis and details of computational procedures.

II. EXPERIMENTAL APPARATUS

A. Optical Pumping

1. Brief Theory of Optical Pumping

The ^3He gas target was polarized by the method of optical pumping which has been reported at length in the literature,^{7-9,54-64)} and hence the following discussion is intended only to briefly summarize the theory.

A weak rf discharge maintains a supply of metastable 2^3S_1 atoms in the ^3He target cell. A ^4He lamp, excited by 10-15 W of 100 MHz rf energy, provides 1.08μ wavelength resonance radiation. This light is circularly polarized by passing it through a linear polarizer followed by a quarter wave plate. The circularly polarized light is of the proper wavelength to induce transitions between the 2^3S_1 and the 2^3P_0 atomic energy levels. Figure 1 shows the pertinent 2^3S_1 and 2^3P_0 levels and their splitting into sublevels. Application of the selection rule $\Delta m_F = +1$ for transitions induced by right hand circularly polarized light (abbreviated RHCP) results in selective excitation of 2^3S_1 metastable atoms in low magnetic sublevels ($m_F = -1/2$ and $-3/2$) to the 2^3P_0 level. Decay back to all the 2^3S_1 sublevels is by the selection rule $\Delta m_F = 0, \pm 1$. The net result is that transitions into and out of the $m_F = -1/2$ and $-3/2$ sublevels of 2^3S_1 occur but only transitions into the $m_F = +1/2$ and $+3/2$ sublevels of 2^3S_1 occur. Thus the population of the

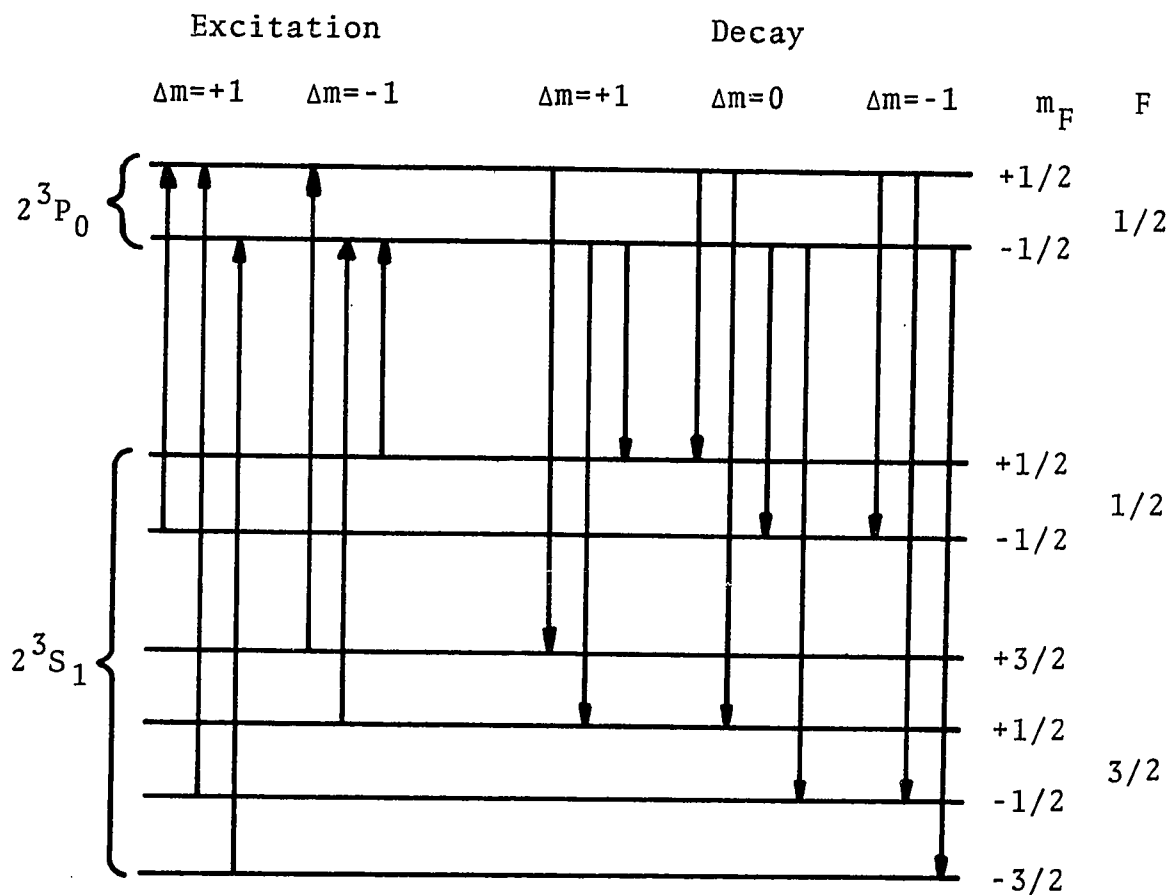


Figure 1. Partial Energy Level Diagram of ${}^3\text{He}$ Atom in External Magnetic Field Showing Transitions Involved in the Optical Pumping Process. (Not to scale.)

higher sublevels increases at the expense of the lower sublevels. A parallel argument applies when LHCP incident light is used. In this case the excitation selection rule is $\Delta m_F = -1$ and the population of the lower sublevels increases at the expense of the higher sublevels.

Figure 1 illustrates the mechanism just described. Transitions corresponding to the two selection rules applicable to the $2^3S_1 - 2^3P_0$ excitation are shown, $\Delta m_F = +1$ for RHCP pumping light and $\Delta m_F = -1$ for LHCP pumping light. The selection rule applicable to the $2^3P_0 - 2^3S_1$ decay is the same for both cases, $\Delta m_F = 0, \pm 1$, and is also shown.

The polarization of the metastable ^3He atoms is transferred to the ground state atoms through metastability exchange collisions.⁸⁾ This can occur because ^3He has spin $\frac{1}{2}$, and due to conservation of spin angular momentum, the magnetic quantum number of a ground state atom can change by ± 1 with a corresponding change of ∓ 1 for the metastable atom. The metastable atom can then be repolarized by optical pumping and the process repeated.

This brief description of optical pumping has not touched on such questions as the effect of magnetic field gradients, relaxation times, relaxation mechanisms, pumping times, and metastability exchange cross section. These factors, as well as a more thorough description of the optical pumping process in general, are discussed in references 7-9, 54-64).

2. Optical Pumping Apparatus

The optical pumping apparatus is very similar to that described by Baker et al.⁶⁵⁾ The 100 kHz rf oscillator used to create metastable ^3He atoms is described in reference 66). The 100 MHz rf oscillator for the ^4He lamp is described by Findley⁶⁷⁾ and is similar to that of Salomaa.⁶⁸⁾ The circular polarizer⁶⁹⁾ consisted of a linear polarizer followed by a quarter wave plate. The two were mounted with their optical axes inclined at 45° relative to one another so that a 90° rotation of the quarter wave plate resulted in changing the sense of the emerging circularly polarized light. A concave mirror was used to focus the pumping light onto the cell. The ^3He polarization can be related to the pumping light absorbed by the ^3He metastable atoms (Appendix A). To monitor the light absorption (actually changes in transmitted light are measured) a lead sulfide detector⁷⁰⁾ was used. The output from this detector (a d.c. signal proportional to the transmitted light intensity) was fed through a bridge circuit to a chart recorder. An idealized example of the light absorption signal is shown in Figure 14, Appendix A.

An external magnetic field of the order of a few gauss was supplied by a pair of helmholtz coils 66 cm in diameter. It was noticed that the magnetic field direction could have a noticeable effect on the light level of the ^4He lamp. By moving the lamp and mirror relative to the cell these effects could be minimized. Air cooling was necessary for

the ^4He lamp, the polarizer, and the electron tubes in the ^4He lamp oscillator. Further discussion of the effects of component location in the optical pumping apparatus and the effects of ^4He lamp pressure on the pumping light is found in reference 71).

B. Target Cell

1. Target Cell Description

The target cell was a two-inch diameter pyrex glass spherical bulb with $\frac{1}{4}$ in. I.D. Sentinel brand⁷²⁾ glass pipe as beam entry, exit, and scattering arms. (Appendix E gives the results of tests on other cell designs.) The two scattering arms were located at $\pm 30.0^\circ$ with respect to the beam exit. The design is the same as that of Baker et al.⁶⁵⁾ except their target cell used four scattering arms instead of two. The beam entry and exit arms were 1.0 in. long and the scattering arms were 1.98 in. long. In order to make certain that the scattering arms were located at the desired angle, a special jig was fabricated for use during manufacture of the cell. This jig consisted of removable support rods located at the proper positions for the four arms. The rod O.D. and the arm I.D. were matched as closely as possible to minimize error in positioning the arms. This device allowed the scattering arms to be located at $30.0^\circ \pm 0.2^\circ$. This tolerance was calculated from a knowledge of the scattering arm length and the amount of play between the scattering arm and the support rod at each end of the scattering arm.

Scattered particle collimation was effected by a rectangular crimp in the scattering arm at the point of attachment to the spherical bulb and by a tantalum disc with a rectangular aperture at the outer end of the scattering arm. The glass collimator was 0.09 in. \times 0.25 in., the metal one was 0.06 in. \times 0.24 in., and their separation was 2.33 in. This geometry allowed particles to be accepted at a maximum laboratory angular deviation of 1.9° . If one assumes a triangular distribution of the scattered particles about the central angle the laboratory rms deviation is 0.8° .

The beam collimator consisted of two circular apertures $3/32$ in. in diameter at a separation of 11.3 in. This permitted a maximum angular spread of 0.5° in the laboratory. By assuming a triangular distribution of the incident beam about zero degrees, the laboratory rms deviation is 0.2° .

The multiple scattering in the aluminum entrance foil can be estimated from the following equation⁷³⁾

$$\langle \theta^2 \rangle^{1/2} = k \log \beta$$

where

$$k = 1.818 \times 10^{-3} z^2 t E^{-2}$$

$$\log \beta = 9.259 + \log t.$$

Here z is the charge number of the incident particle, t is the foil thickness in mils, E is the incident energy in MeV, and θ is the center-of-mass angle for the incident particle scattering from aluminum. Due to the relative masses

of ^3He and ^4He and ^{27}Al , the center-of-mass and laboratory angles will be approximately equal and $\langle\theta^2\rangle^{1/2}$ will be taken as the laboratory rms deviation due to entrance foil scattering. For the maximum and minimum values of the bombarding energy $\langle\theta^2\rangle^{1/2} = 0.3^\circ$ and 0.6° , respectively, in both the ^3He and ^4He scattering.

The various laboratory rms angular deviations have been added in quadrature to give a combined value of 1.0° and 1.1° for the maximum and minimum values of bombarding energy in the experiment. In the center-of-mass system these correspond to 2.0° and 2.2° , respectively, for ^3He - ^3He scattering and to 2.5° and 2.8° , respectively, for ^3He - ^4He scattering.

An rf shield was provided for each of the particle detectors. It was quite similar to that shown in reference 65) except that the solid state detector was mounted on an adapter which fitted directly onto a vacuum feed through (Amphenol UG-657/U) threaded into the closed end of the shield. The shield was evacuated by a port fastened to its side and was thus held in place by atmospheric pressure. A rubber O-ring provided a seal between the rf shield and the aluminum flange supporting the foil assembly.

Aluminum foils 0.00035 in. thick were used as windows on all four arms of the cell. An improved design⁷⁴⁾ was used to mount the foil windows which allowed leak testing prior to installation on the cell arms. This represents considerable improvement over the previous method of sealing the foil window directly to the glass arm.^{65,71)} The new design

consisted of mounting the foil between two $\frac{1}{4}$ in. thick aluminum plates (which had $\frac{1}{4}$ in. diameter holes through their centers to admit particles), leak testing the assembly and then attaching it to the end of the cell arm as shown in reference 65). Indium⁷⁵ wire gaskets were used between the foil and the inner aluminum disc and between the inner aluminum disc and the glass arm. Indium has the advantage that it does not outgas nearly as much as rubber but it also has the disadvantage of a relatively low melting point of 156.4° C. This will be discussed further in the cell cleanup procedure, Section III.B.3.

The foil windows were cut using a 0.517 ± 0.002 in. diameter die. Each foil was then weighed several times on a balance calibrated to read in micrograms. The foil weight w was taken as the average of the several weighings and the standard deviation σ of the readings was used as the error in w . The total error in the foil weight is given by

$$dW = W[(\sigma/w)^2 + (dA/A)^2]^{\frac{1}{2}}$$

where W and dW are in mg/cm^2 , w and σ are in mg , and A and dA are in cm^2 . The foil weights ranged from 2.262 to 2.335 mg/cm^2 with total errors ranging from 0.018 to 0.029 mg/cm^2 .

2. Entrance Foil and Target Energy Loss Corrections

Energy loss in the entrance foil was computed by numerical integration using the trapezoidal rule. The energy loss derivatives dE/dX for aluminum were taken from reference 76). Fifty integration steps of equal size were found to give

values of energy lost in the foil which compared well with those obtained from range-energy relations.⁷⁷⁾

The energy lost by the projectiles inside the target was calculated from dE/dX values for helium⁷⁶⁾ and found to be less than 5 keV for the lowest energy α -particles. Since this loss is small compared to the entrance foil loss and is also smaller than the uncertainty in the bombarding energy (20 keV) it was neglected.

The proton resonance at 4.681 MeV in the $^{40}\text{Ca}(p,p)^{40}\text{Ca}$ reaction was used as the energy calibration for the experiment. The calibration and the uncertainty in the bombarding energy are discussed in Appendix F.

3. Target Cell Cleaning and Filling

Prior to assembly of the cell the glass parts were washed thoroughly with a low residue cleanser (Alconox) and distilled water. This was followed by a rinse in high purity acetone or isopropyl alcohol. The glass stopcock on the cell filling tube was assembled with a light application of Apiezon T high vacuum stopcock grease. The stopcock was located approximately $1\frac{1}{2}$ -2 in. from the spherical bulb and the presence of stopcock grease at this point did not appear to have any serious contaminating effect on the ^3He gas.

The aluminum parts--foils, foil holder discs, and indium gaskets--were all washed thoroughly in high purity acetone followed by a wash in high purity isopropyl alcohol. The parts were allowed to air dry and the foils were assembled

between the two discs using 0.025 in. diameter indium wire gaskets. Six equally spaced screws held the two discs and the foil together. Each foil assembly was then leak tested and accepted if there was no indication of a leak on the most sensitive scale of the helium leak detector.

Cleaning the cell prior to filling it with ^3He is a lengthy process requiring typically five to seven days for a new cell. The procedure is to evacuate the cell using a vacuum system capable of attaining pressures lower than 5×10^{-7} torr (1 torr = 1 mm Hg). The cell can be cleaned by heating while under a vacuum⁶⁾ but care must be exercised so as not to melt the indium gaskets. Running a ^4He discharge inside the cell appears to be about as efficient as any cleaning process thus far attempted. The cell is filled with 1/4-3/4 torr of ^4He and a discharge is ignited by a spark from a Tesla coil⁷⁸⁾ and maintained by about 10 W of rf energy.⁷⁹⁾ The discharge spectrum as viewed through a spectroscope is a continuum and quickly extinguishes due to impurities. The cell is evacuated and the process repeated. After numerous discharges over a period of several hours with little change in the spectrum, a significant and almost sudden improvement in the cell cleanliness takes place--some of the background spectrum disappears. Several such cycles or plateau regions of cell cleanliness are seen before only the characteristic helium spectrum remains. During the cleaning process it is necessary to ionize the gas in the cell arms by using a Tesla coil wired across the arms on opposite sides of the cell. If

this is not done the spherical part of the cell will clean up but the arms will still contain excessive impurities and polarization cannot be achieved. It is necessary to monitor the temperature at the cell arms because sufficient energy is supplied by the rf source to raise the arm temperature above the indium melting point. Before filling the cell one must be certain that it is clean. A good rule of thumb is that the cell must sustain the ^4He discharge for $\frac{1}{2}$ hour with only the helium lines and no background visible at the end of this period. Then the cell is evacuated to less than 1.5×10^{-7} torr and filled to 4-5 torr of $^3\text{He}^{80)}$ through a liquid helium cold trap. Under these conditions the cell will usually work.

C. Detectors and Electronics

Ortec silicon surface barrier detectors were used in the experiment. For the elastic scattering of ^3He and ^4He 50 mm^2 sensitive area \times 100 micron depletion depth detectors were used and for the inelastic ^3He scattering $50 \text{ mm}^2 \times 2000$ micron depletion depth detectors were used. These had threads to match Microdot cable connectors, which was a convenient feature. Bias was set on each detector as recommended by the manufacturer and these were operated in a vacuum as previously described in Section II.B.1. The detector output was fed directly into Tennelec model 214 preamplifiers. Power for the preamplifiers and bias for the detectors was provided by a Tennelec model 901 RM power supply. Output from the preamplifiers was sent directly to a TMC 400 channel analyzer. The

beam passing through the cell was stopped in air by a 0.050 in. tantalum plate at the end of the beam exit arm. The beam current was integrated by a Brookhaven Electronics Corp. model 1000 current integrator and recorded by an Ortec model 431 timer-scaler. An attempt was made to keep all data runs about the same length to obtain approximately equal statistics in each run. Experience in the latter part of the experiment showed that shorter data runs were preferable in order to minimize the effects of beam wander and the subsequent necessity for cell realignment.

The collected spectra were printed by the on-line computer and recorded on magnetic tape for analysis at a later time.

III. EXPERIMENTAL RESULTS

A. Optically Measured Target Polarization

The optically measured target polarization p and error Δp were computed from optical pumping light absorption signals $\langle \delta I/I \rangle$ and error $\Delta \langle \delta I/I \rangle$ using the method explained in Appendix A. The error Δp does not include any systematic contribution due to uncertainty in the proper value for the parameter f used in computing the target polarization. Values of f between 0.5 and 1.0 have been reported.^{8,62-64)} In the present work a median value of $f = 0.7$ was used. Baker et al.⁶⁵⁾ have shown that this can result in a systematic error of $\pm 15\%$ in p compared to using $f = 0.5$ and 1.0 , respectively. Thus the values of p and Δp could be multiplied by a constant whose value is between 0.85 and 1.15. Appendix A also describes the technique used in measuring $\langle \delta I/I \rangle$ and explains the equations used in determining p from $\langle \delta I/I \rangle$. The required constants are also listed.

In the data tabulation which follows $\langle \delta I/I \rangle$, $\Delta \langle \delta I/I \rangle$, and p , Δp are listed in chronological order for each data run. The time given is in elapsed hours from the start of each run. In some cases the time was reinitialized during a run; this was done whenever there was an extended interruption due to technical difficulties. Each time point represents data taken at one energy and is a composite of four separate data collection periods as explained in Appendix B. Since the time required to collect all the data at a single energy

Tables 1-3. Optically Measured Target Polarization Data for a ^3He Gas Target Polarized by the Method of Optical Pumping. Optical pumping light absorption signals $\langle\delta I/I\rangle$, $\Delta\langle\delta I/I\rangle$ and target polarization p , Δp are listed in chronological order for each run. Time is in elapsed hours from the beginning of the run. The sequence numbers are assigned to allow correlation with data in Tables 4a, 4b, 7, and 8. The target polarization error Δp does not include any systematic error discussed in the text. Each table is identified by run numbers and the nuclear experiment being carried out during the run. The value of f is also given. Points at which the target cell was recleaned and refilled due to low polarization are identified and the ^3He pressure in mm Hg is given.

Table 1. Target Polarization Data, Runs 2 and 5, ${}^3\text{He}({}^4\text{He}, {}^4\text{He}){}^3\text{He}$, $f = 0.7$. These data correspond to the asymmetry and reaction analyzing power data given in Tables 4a and 4b.

<u>Seq.</u>	<u>Time</u>	<u>$\langle \delta I / I \rangle$</u>	<u>$\Delta \langle \delta I / I \rangle$</u>	<u>P</u>	<u>ΔP</u>	<u>Remarks</u>
				<u>Run 5</u>		
1	44.65	0.5137	0.0182	0.1002	0.0028	Cell and time continued from Run 4
2	47.68	0.5948	0.0228	0.1124	0.0033	
3	50.88	0.5697	0.0119	0.1090	0.0016	
4	53.37	0.5382	0.0166	0.1041	0.0026	
5	55.30	0.4254	0.0261	0.0859	0.0043	
6	0.	0.6597	0.0141	0.1221	0.0022	Cell refilled
7	2.50	0.7847	0.0194	0.1393	0.0025	
8	5.03	0.6404	0.0144	0.1191	0.0020	
				<u>Run 2</u>		
1	0.	0.8188	0.0501	0.1441	0.0066	Cell refilled, 5.9 mm
2	4.33	0.8484	0.0503	0.1478	0.0069	
3	8.20	0.7548	0.0128	0.1356	0.0017	
4	13.63	0.7158	0.0181	0.1300	0.0023	
5	18.82	0.6954	0.0175	0.1274	0.0024	
6	22.42	0.6840	0.0171	0.1255	0.0024	
7	25.95	0.6771	0.0156	0.1244	0.0022	
8	28.57	0.7126	0.0173	0.1295	0.0024	
9	31.07	0.6931	0.0247	0.1269	0.0033	
10	32.45	0.7395	0.0715	0.1332	0.0097	
11	39.23	0.6298	0.0232	0.1179	0.0033	
12	43.33	0.6635	0.0167	0.1227	0.0023	
13	45.50	0.6909	0.0169	0.1265	0.0021	
14	48.75	0.6629	0.0211	0.1226	0.0030	
15	51.63	0.6438	0.0196	0.1197	0.0028	

Table 2: Target Polarization Data, Runs 1 and 3, $^3\text{He}(^3\text{He}, ^3\text{He})^3\text{He}$, $f = 0.7$. These data correspond to the asymmetry and reaction analyzing power data in Table 7.

Seq.	Time	$\langle \delta I / I \rangle$	$\Delta \langle \delta I / I \rangle$	p	Δp	Remarks
				Run 1		
1	0°	0.6834	0.0177	0.1254	0.0025	New cell, 5.5 mm
2	7.17	0.7477	0.0145	0.1345	0.0017	
3	10.58	0.6941	0.0204	0.1270	0.0026	
4	15.33	0.7145	0.0179	0.1297	0.0025	
5	21.13	0.6943	0.0182	0.1271	0.0026	
6	23.90	0.6434	0.0201	0.1196	0.0029	Cell refilled, 6.0 mm
7	28.83	0.6207	0.0160	0.1165	0.0025	
8	32.17	0.5796	0.0168	0.1101	0.0023	
9	34.08	0.5862	0.0198	0.1112	0.0028	
10	38.50	0.6200	0.0167	0.1164	0.0023	
11	56.72	0.8957	0.0150	0.1547	0.0023	
12	61.58	0.7810	0.0139	0.1387	0.0019	
13	65.58	0.7101	0.0156	0.1291	0.0022	
14	70.23	0.6819	0.0134	0.1251	0.0018	
15	74.82	0.6999	0.0144	0.1280	0.0020	
16	80.33	0.6138	0.0516	0.1154	0.0075	
17	84.25	0.5962	0.0185	0.1127	0.0029	
18	88.70	0.6326	0.0147	0.1184	0.0020	
19	93.97	0.6428	0.0146	0.1195	0.0020	
20	98.65	0.6570	0.0227	0.1217	0.0030	Cell refilled, 6.1 mm
21	101.67	0.5952	0.0245	0.1125	0.0035	
22	109.50	0.7315	0.0213	0.1324	0.0030	
23	116.67	0.5835	0.0229	0.1107	0.0033	
24	120.47	0.5868	0.0213	0.1112	0.0030	
25	123.38	0.6834	0.0462	0.1254	0.0067	
26	130.65	0.6736	0.0164	0.1243	0.0023	
27	133.33	0.6584	0.0179	0.1219	0.0025	
28	137.28	0.6672	0.0236	0.1233	0.0034	

Table 2. Run 1, Continued.

<u>Seq.</u>	<u>Time</u>	<u>$\delta I/I$</u>	<u>$\Delta \delta I/I$</u>	<u>p</u>	<u>Δp</u>	<u>Remarks</u>
29	140.03	0.6453	0.0179	0.1199	0.0025	
30	142.97	0.6965	0.0200	0.1274	0.0028	
31	147.33	0.6585	0.0453	0.1220	0.0066	
<u>Run 3</u>						
1	0.	0.9618	0.0397	0.1651	0.0062	Cell refilled, 6.0 mm
2	3.07	0.7813	0.0188	0.1387	0.0026	
3	3.97	0.6888	0.0208	0.1262	0.0027	
4	5.97	0.6244	0.0275	0.0071	0.0040	
5	8.15	0.6234	0.0357	0.1169	0.0053	
6	17.95	0.6732	0.0217	0.1243	0.0031	Cell refilled, 6.4 mm
7	20.37	0.7189	0.0268	0.1304	0.0037	
8	22.30	0.5964	0.0271	0.1127	0.0040	
9	25.07	0.6798	0.0339	0.1248	0.0048	
10	27.20	0.5892	0.0477	0.1116	0.0069	
11	29.50	0.5106	0.0302	0.0997	0.0047	
12	30.90	0.5895	0.0298	0.1116	0.0044	
13	38.37	0.6056	0.0332	0.1142	0.0047	
14	42.07	0.6343	0.0281	0.1187	0.0041	

Table 3. Target Polarization Data, Run 4, $^3\text{He}(^3\text{He},p)^5\text{Li}$ (ground state), $f = 0.7$. These data correspond to the asymmetry and reaction analyzing power data in Table 8.

<u>Seq.</u>	<u>Time</u>	<u>$\langle \delta I / I \rangle$</u>	<u>$\Delta \langle \delta I / I \rangle$</u>	<u>P</u>	<u>Δp</u>	<u>Remarks</u>
1	0.	0.5440	0.0607	0.1050	0.0093	Cell refilled, 4.7 mm
2	0.	0.5656	0.0152	0.1084	0.0021	Cell refilled, 4.7 mm
3	2.23	0.5803	0.0151	0.1102	0.0021	
4	3.63	0.5546	0.0140	0.1067	0.0022	
5	4.78	0.5833	0.0157	0.1107	0.0021	
6	0.	0.4903	0.0266	0.0966	0.0044	Cell refilled, 5.2 mm
7	0.	0.6484	0.0409	0.1204	0.0059	Cell refilled, 5.3 mm
8	1.95	0.5344	0.0260	0.1035	0.0041	
9	4.23	0.5365	0.0302	0.1038	0.0047	
10	6.40	0.5017	0.0369	0.0984	0.0060	
11	8.63	0.4935	0.0293	0.0971	0.0049	
12	11.00	0.5106	0.0204	0.0998	0.0032	Cell and time carried over to Table 1, Run 5

could be several hours, the time shown is that at the mid-point of the four data collection periods. The sequence numbers allow correlation of p with the experimental asymmetry A and reaction analyzing power P_3 in subsequent tables. From the listing of time the decline of target polarization as a function of cell age can be seen.

B. Elastic Scattering of ^4He from a
Polarized ^3He Gas Target

1. Experimental Asymmetry and Reaction Analyzing Power

The experimental Asymmetry A and reaction analyzing power P_3 for the elastic scattering of ^4He from a polarized ^3He gas target have been measured at the center-of-mass angles 71.6° and 120.0° for 13 bombarding energies between 5.75 and 10.01 MeV, corresponding to the equivalent ^3He laboratory energy range of 3.30 to 6.86 MeV, accurate to ± 20 keV. To clarify the nomenclature, A is sometimes referred to as laboratory or experimental asymmetry or left-right scattering asymmetry and P_3 as polarization or polarization data. To avoid confusion the optically measured target polarization p in Section III.A. will be referred to as "target polarization."

The equations required in computing A , P_3 , their errors, and the weighted average for duplicate measurements at a given energy are found in Appendix B. A general discussion of the asymmetries is also given there. Tables 4a and 4b give the values of A and P_3 along with their errors. The error ΔA

Tables 4a and 4b. Experimental Asymmetry and Reaction Analyzing Power P_3 for ^4He Elastically Scattered from a Polarized ^3He Gas Target. The sequence numbers allow correlation of A and P_3 with the target polarization p in Table 1. The equivalent ^3He Laboratory energy in MeV is shown, accurate to ± 20 keV. Where several data exist at a single energy point a weighted average (denoted by $\langle \rangle$) is computed for A, the statistical error ΔA , P_3 and ΔP_3 . ΔP_3 does not include any systematic error discussed in Section III.A. Each table is identified by its run number, the center-of-mass angle, and the nuclear reaction being carried out during the run.

Table 4a. Experimental Asymmetry and Reaction Analyzing Power, Runs 2 and 5, ${}^3\text{He}({}^4\text{He}, {}^4\text{He}){}^3\text{He}$, $\theta_{\text{cm}} = 71.6^\circ$. The corresponding target polarization data are given in Table 1.

Seq.	Energy	A	$\langle A \rangle$	ΔA	$\langle \Delta A \rangle$	P ₃	$\langle P_3 \rangle$	ΔP_3	$\langle \Delta P_3 \rangle$
<u>Run 5</u>									
8	3.30	-0.0053		0.0068		-0.0447		0.0572	
3	3.51	-0.0026		0.0043		-0.0246		0.0399	
4		0.0002		0.0032		0.0026		0.0307	
5		0.0006		0.0033		0.0072		0.0384	
6		0.0103		0.0051		0.0845		0.0419	
7		-0.0087		0.0051		-0.0626		0.0397	
1	3.88	-0.0080	0.0001	0.0031	0.0017	-0.0804	0.0001	0.0310	0.0167
2		0.0004	-0.0032	0.0027		0.0041	-0.0283	0.0245	0.0192
<u>Run 2</u>									
4	4.37	-0.0114		0.0031		-0.0884		0.0239	
5	4.46	-0.0082		0.0042		-0.0645		0.0334	
6	4.64	-0.0279		0.0024		-0.2228		0.0339	
7	4.79	-0.0314		0.0042		-0.2527		0.0343	
8	4.95	-0.0620		0.0042		-0.4790		0.0340	
9	5.09	-0.0766		0.0044		-0.6041		0.0388	
1	5.21	-0.0809		0.0044		-0.5971		0.0338	
2		-0.0852		0.0046		-0.5768		0.0415	
3		-0.0827		0.0046		-0.5739		0.0416	
10	6.04	0.0460	-0.0829	0.0039	0.0026		-0.5847		0.0221
14	6.46	0.0407		0.0049		0.3458		0.0391	
15		0.0528		0.0054		0.3324		0.0408	
11	6.86	-0.0040	0.0462	0.0042	0.0036	0.4417	0.3801	0.0464	0.0306
12		0.0558		0.0057		-0.0345		0.0360	
13		0.0491		0.0054		0.4546		0.0472	
			0.0263		0.0028	0.3883		0.0434	0.0239

Table 4b. Experimental Asymmetry and Reaction Analyzing Power, Runs 2 and 5, ${}^3\vec{\text{He}}({}^4\text{He}, {}^3\text{He}){}^4\text{He}$, $\theta_{\text{cm}} = 120.0^\circ$. The corresponding target polarization data are given in Table 1.

Seq.	Energy	\underline{A}	$\underline{\langle A \rangle}$	$\underline{\Delta A}$	<u>Run 5</u>		$\underline{P_3}$	$\underline{\langle P_3 \rangle}$	$\underline{\Delta P_3}$	$\underline{\langle \Delta P_3 \rangle}$
8	3.30	0.0174		0.0163			0.1464		0.1375	
3	3.51	0.0055		0.0105			0.0509		0.0966	
4		0.0075		0.0088			0.0728		0.0847	
5		0.0150		0.0090			0.1752		0.1059	
6		0.0100		0.0142			0.0822		0.1166	
7		0.0311		0.0162			0.2239		0.1166	
			0.0116		0.0048			0.1113		0.0455
1	3.88	0.0153		0.0071			0.1535		0.0716	
2		0.0104		0.0065			0.0930		0.0587	
			0.0127		0.0048			0.1173		0.0453
<u>Run 2</u>										
4	4.37	0.0041		0.0067			0.0322		0.0519	
5	4.46	0.0052		0.0088			0.0405		0.0687	
6	4.64	0.0116		0.0077			0.0932		0.0614	
7	4.79	0.0097		0.0063			0.0784		0.0514	
8	4.95	0.0018		0.0050			0.0146		0.0391	
9	5.09	0.0102		0.0039			0.0810		0.0309	
1	5.21	0.0302		0.0024			0.2231		0.0185	
2		-0.0114		0.0026			-0.0774		0.0182	
3		-0.0120		0.0026			-0.0837		0.0185	
			0.0032		0.0014			0.0191		0.0106
10	6.04	-0.0456		0.0159			-0.3425		0.1220	
14	6.46	0.0130		0.0175			0.1065		0.1430	
15		-0.0192		0.0178			-0.1605		0.1491	
			-0.0028		0.0125			-0.0214		0.1032
11	6.86	-0.0113		0.0106			-0.0958		0.0906	
12		0.0017		0.0138			0.0143		0.1130	
13		0.0198		0.0139			0.1570		0.1105	
			0.0600		0.0072			0.0081		0.0595

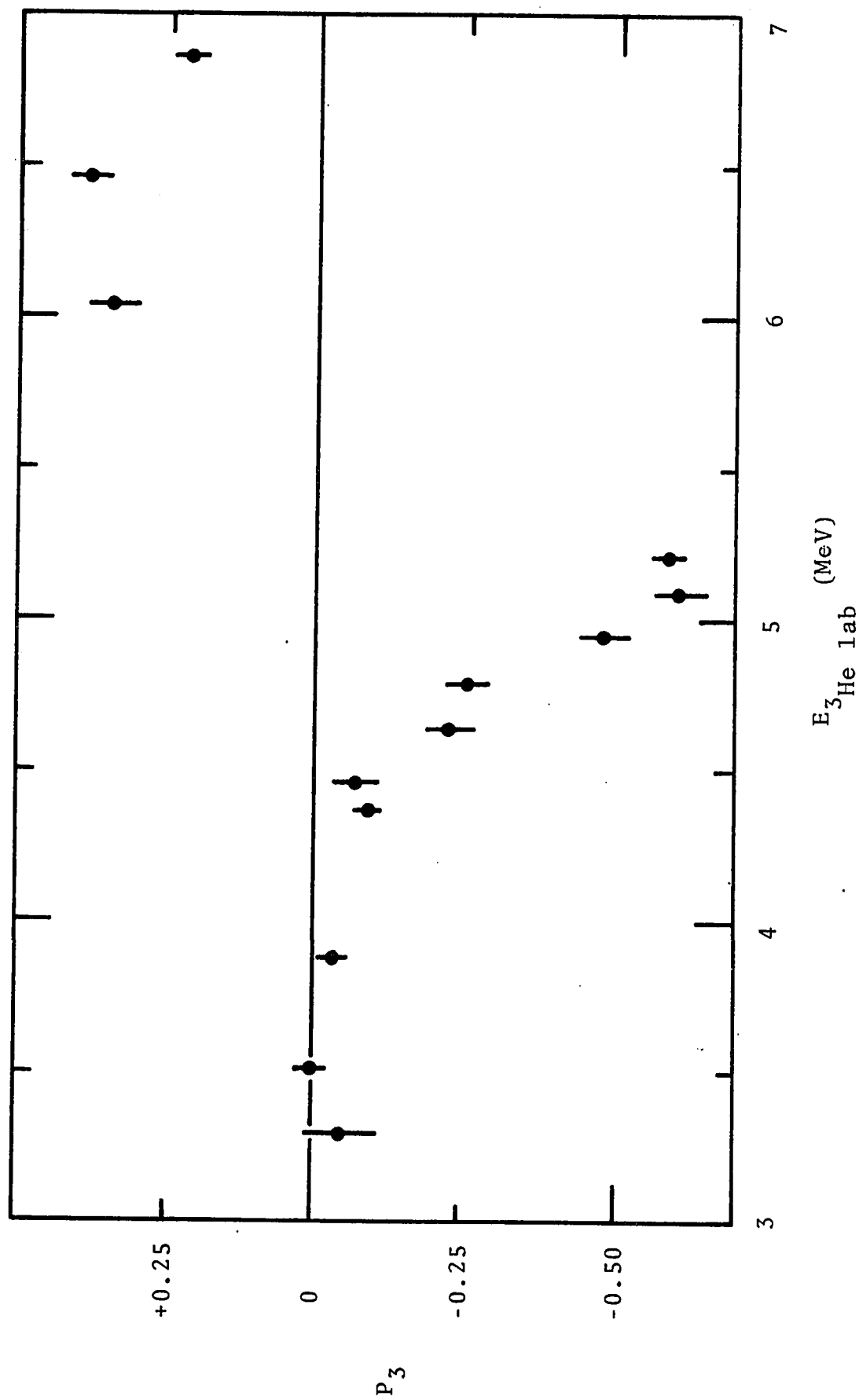


Figure 2a. Reaction Analyzing Power vs. Equivalent ${}^3\text{He}$ Laboratory Energy for ${}^4\text{He}$ Elastically Scattered from a Polarized ${}^3\text{He}$ Gas Target, $\theta_{\text{cm}} = 71.6^\circ$.

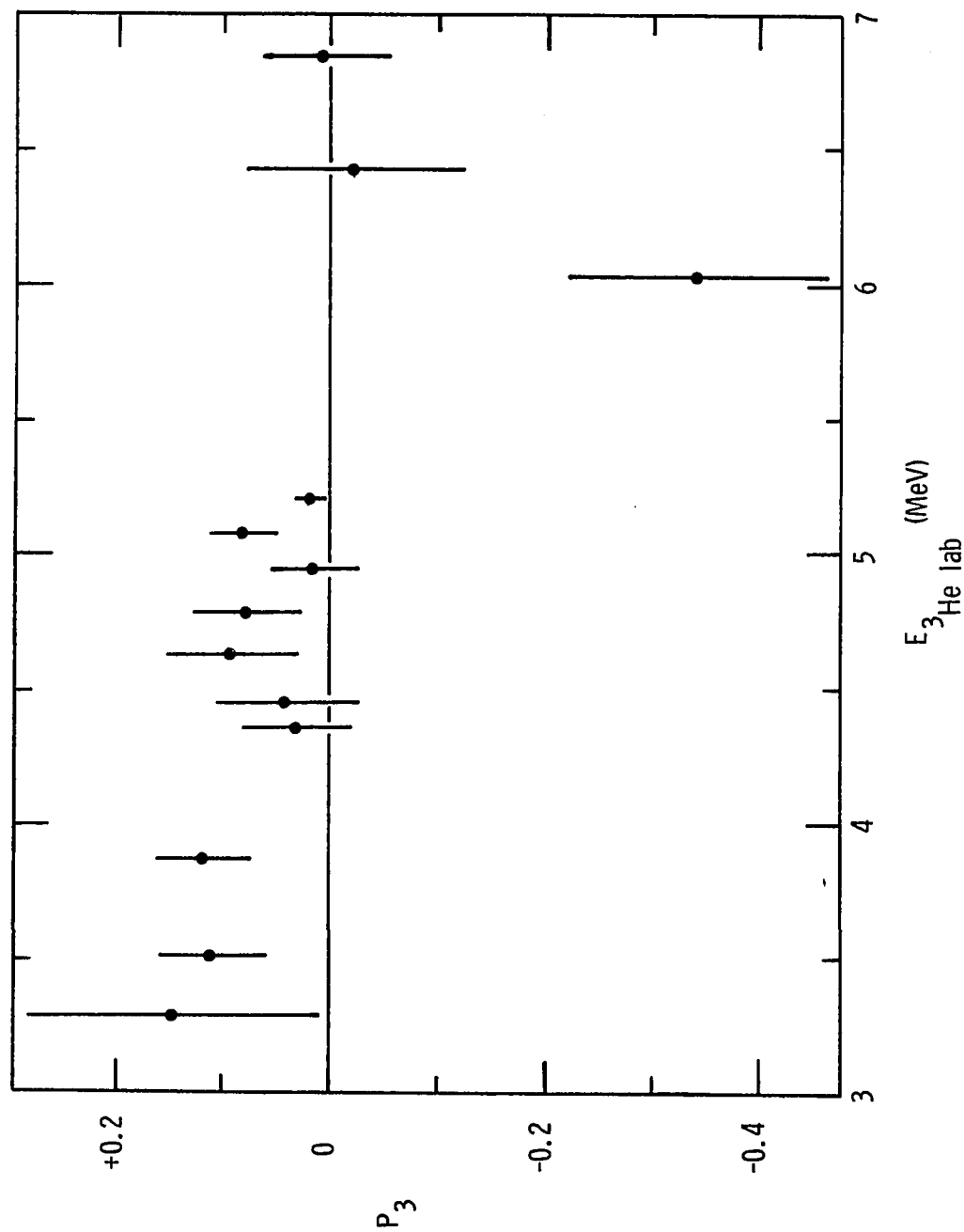


Figure 2b. Reaction Analyzing Power vs. Equivalent ^3He Laboratory Energy for ^4He Elastically Scattered from a Polarized ^3He Gas Target, $\theta_{\text{cm}} = 120.0^\circ$.

is the statistical error in A and the error ΔP_3 is the result of adding in quadrature the statistical error ΔA and the error in the optically measured target polarization, Δp . P_3 with error bars $\pm \Delta P_3$ is plotted as a function of equivalent ^3He laboratory energy in Figures 2a and 2b. The error ΔP_3 does not include any systematic contribution due to uncertainty about the proper value of the parameter f used in computing the target polarization p . As discussed in Section III.A. this systematic error can be as much as $\pm 15\%$ in p , resulting in a $\pm 15\%$ error in P_3 . The effects of systematic errors will be discussed further in Section III.B.2.e.

No correction for background was made because the background events represented a small fraction of the total events under a given peak. This fraction remained nearly constant during the four data collection periods at each energy and was no more than 1.5% of the total events for the ^3He - ^4He elastic scattering. A 1.5% background results in a negligible change in A and P_3 compared to the statistical errors in these quantities. This effect would be systematic and would have no noticeable effect on the ^3He - ^4He elastic scattering phase shifts, as is shown in Section III.B.2.e.

The values of P_3 in Tables 4a and 4b have been compared where data exists with the spin polarization maps given by Barnard et al.,¹⁵⁾ Spiger and Tombrello,¹⁶⁾ and Hardy et al.²⁵⁾ These maps were generated using the derived phase shifts from the ^3He - ^4He elastic scattering experiments reported by the authors. Barnard's low energy P_3 data agree with the current

work while the data of Spiger and that of Hardy are smaller (more negative) than the higher energy values in Tables 4a and 4b.

From the results of the present experiment a spin polarization map has also been generated, Figure 3. The phase shifts used to generate the polarization map were obtained as follows. For the s-wave the hard sphere phase shifts for a radius of 2.8 fm were used. The single level parameterization discussed in Section III.B.2. provided the p-wave values. Since the single level formula would not provide a satisfactory fit to the f-waves (also discussed in Section III.B.3.), a least squares technique was used to fit the $f_{5/2}$ phase shifts with a fourth degree polynomial. A satisfactory polynomial fit to the $f_{7/2}$ phase shifts could not be found over the entire energy range, but a fourth degree polynomial would fit the phase shifts below 5.0 MeV, and the data provided by it were used. From 5.0 to 7.0 MeV interpolated values of the $f_{7/2}$ phase shift were used. The errors introduced in the interpolation should be no greater than the error bars shown in Figure 8 between 5.0 and 5.21 MeV and between 6.0 and 7.0 MeV. But between 5.21 and 6.0 MeV. these errors are estimated to be from 5° to 15° because of the absence of data in this region. In all cases the phase shifts below the lowest energy of the experiment (3.30 MeV) were provided by the hard sphere, single level, or polynomial fitting procedures. For comparison the locations of the data in Tables 4a and 4b are indicated on the polarization map, Figure 3.

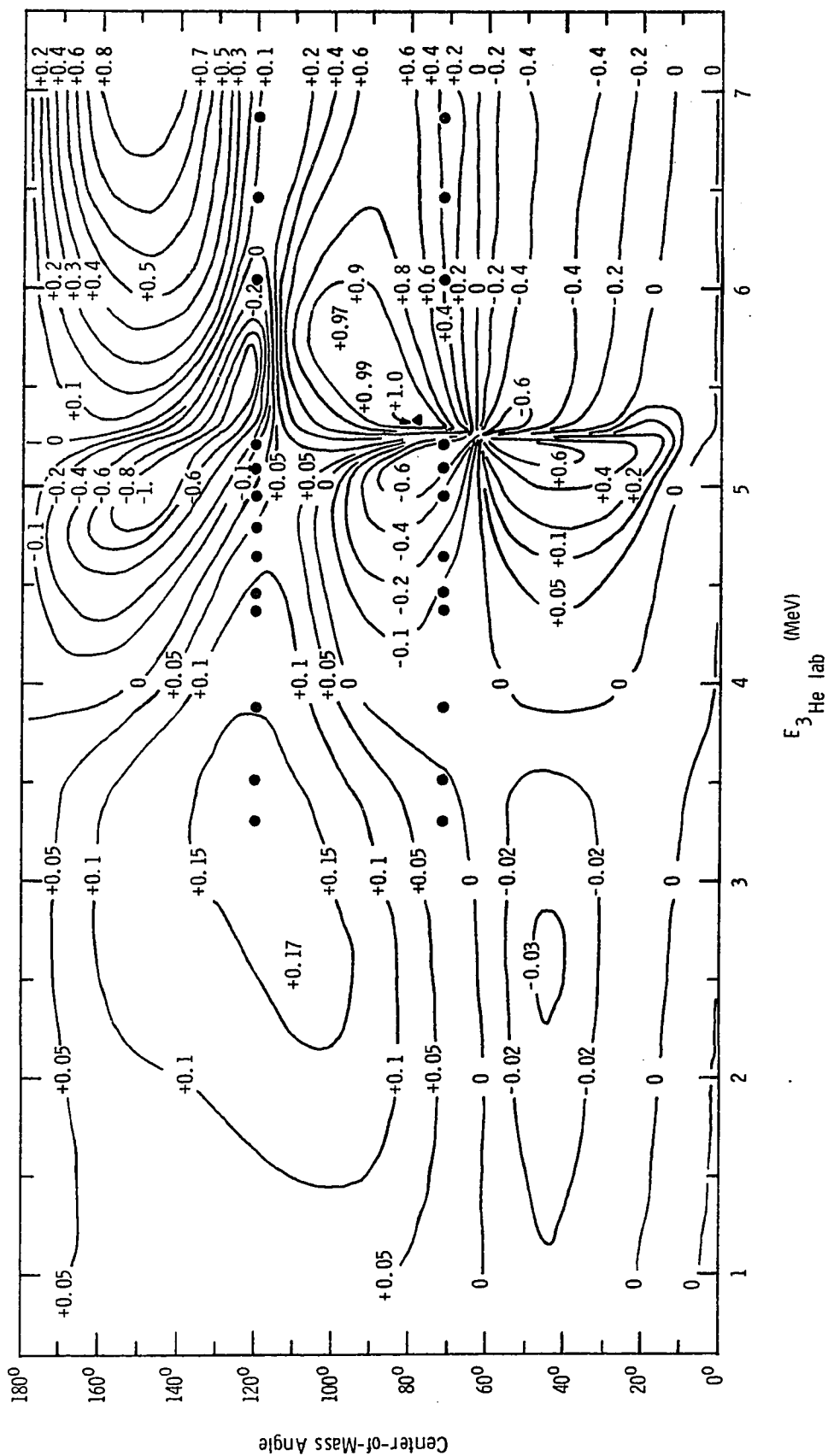


Figure 3. Contour Map of ^3He Spin Polarization (Basel Convention) as a Function of Equivalent ^3He Laboratory Energy and Center-of-Mass Angle. The numbers not labeling a contour are the calculated values of the polarization at the locations of their decimal points. The solid circles represent points at which the experimental asymmetry was measured in the current work. See Tables 4a and 4b.

The instrumental asymmetry A_0 gives an indication of the deviation of the experiment from complete symmetry. Its departure from zero is a measure of the effects of changes in the experimental configuration such as beam wander that have not been explicitly included in the mathematical treatment. The maximum value of A_0 for the ^4He - ^3He elastic scattering was 1.4%, which is acceptable.

2. Phase Shift Analysis of the ^3He - ^4He Elastic Scattering Data

a. Method

The fact that ^3He - ^4He scattering represents the scattering of a spin $\frac{1}{2}$ particle from a spin 0 particle greatly simplifies the analysis because only one ℓ -value is permitted for each value of the total angular momentum and parity. To perform the phase shift analysis a computer program was employed which used the differential cross section and polarization formulas derived in Appendix C. The program was required to minimize the value of χ^2 :

$$\chi^2 = \sum_{i=1}^N \left(\frac{D(\theta_i)_{\text{exp}} - D(\theta_i)_{\text{calc}}}{\epsilon(\theta_i)} \right)^2$$

where N is the number of data points, $D(\theta_i)$ is a differential cross section of polarization datum at the center-of-mass angle θ_i , and $\epsilon(\theta_i)$ is the experimental error associated with the experimental datum $D(\theta_i)_{\text{exp}}$.

The phase shifts for $\ell \geq 4$ were set to zero because even at higher energies there is no indication that these depart significantly from zero. The d-waves were also fixed at zero because they too are small at higher energies and there are no known d-states in the ${}^7\text{Be}$ system. (The d-waves will be discussed further in Section III.B.2.c.) Thus the variable parameters were the five real parts of the s-, p-, and f-wave phase shifts since the energy range of the experiment was below the ${}^3\text{He}$ - ${}^4\text{He}$ threshold.

The method used in determining the phase shifts was to hold one phase shift constant and allow the program to vary the other four. When the minimum value of χ^2 had been found for this set of values of the one fixed and four variable phase shifts, the fixed phase shift was incremented by 0.1° and the procedure repeated. This gave another minimum value of χ^2 corresponding to the second set of values for the five phase shifts in question. In this manner a large set of minimum values of χ^2 and matching phase shifts were computed. From this set of minimum χ^2 -values and corresponding phase shifts the acceptable value δ_0 of the phase shift was found. The acceptable value is defined as that corresponding to the smallest χ^2 of the set, namely χ_0^2 . A graphic illustration of this procedure is provided by the solid curve in Figure 4. This particular example is that of χ^2 vs. the $p_{3/2}$ phase shift at $E_{{}^3\text{He lab}} = 4.64$ MeV. The acceptable value of the phase shift corresponds to the lowest point on the curve and in this example $\delta_0 = 157.5^\circ$ at $\chi_0^2 = 3.62$.

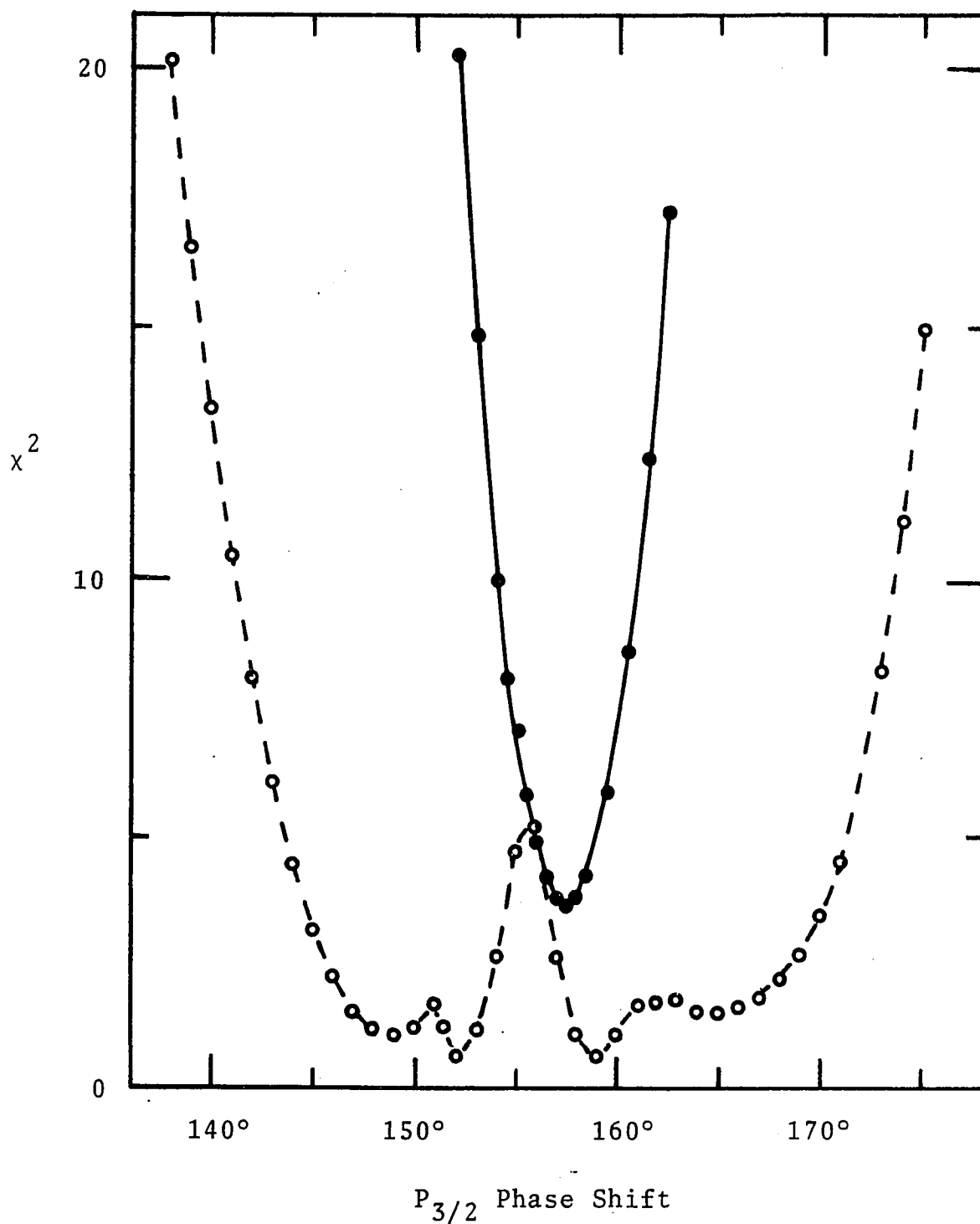


Figure 4. χ^2 vs. $P_{3/2}$ Phase Shift at $E_{^3\text{He lab}} = 4.64$ MeV. The solid curve was generated using both cross section and polarization data and the dashed curve was generated using cross section data only. The curves serve only to connect the data points.

The phase shift error was assigned in the following manner. The likelihood of a given fit to the experimental data can be estimated by ⁸¹⁾

$$L \propto \exp(-\frac{1}{2}\chi^2)$$

and for the best fit δ_0 , L is taken as

$$L_0 = \exp(-\frac{1}{2}\chi_0^2). \quad (1)$$

The error in the phase shift is defined as that value which reduces the likelihood function L_0 to a value L_1 corresponding to a value δ_1 of the phase shift one standard deviation away from the best fit δ_0 . Thus

$$L_1 = L_0 \exp(-\frac{1}{2}) = \exp[-\frac{1}{2}(\chi_0^2 + 1)] = \exp(-\frac{1}{2}\chi_1^2) \quad (2)$$

where

$$\chi_1^2 = \chi_0^2 + 1. \quad (3)$$

The phase shift error is then given by

$$\Delta\delta = \frac{1}{2}|\delta_H - \delta_L|$$

where δ_H and δ_L are the two values of the phase shift corresponding to χ_1^2 . Plots such as Figure 4 were then used to determine $\Delta\delta$. In the example shown in Figure 4 $\chi_1^2 = 4.62$, $\delta_H = 158.7^\circ$, $\delta_L = 156.3^\circ$, and $\Delta\delta = 1.2^\circ$.

It should be noted that the phase shift error determined by the foregoing method does not include any contribution from systematic errors discussed in Section III.B.2.e.

b. Initial Conditions for the Phase
Shift Searches

The data used in the phase shift analysis consisted of the cross section data of Barnard et al.¹⁵⁾ for $E_{\text{He lab}} \leq 5.21$ MeV and that of Spiger and Tombrello¹⁶⁾ for energies above this, the polarization data P_3 at $\theta_{\text{cm}} = 71.6^\circ$ and 120.0° from the present experiment and that of Hardy⁷⁴⁾ at $\theta_{\text{cm}} = 87.0^\circ$ and Hardy et al.²⁵⁾ at $\theta_{\text{cm}} = 114.0^\circ$. At $\theta_{\text{cm}} = 71.6^\circ$, 87.0° , and 120.0° data were available at all 13 equivalent ^3He laboratory energies in the 3.30-6.86 MeV range of the experiment but at $\theta_{\text{cm}} = 114.0^\circ$ only the two highest energy data were available, 6.46 and 6.86 MeV. The beginning values of the phase shifts were taken from references 15) and 16) in the same manner as the cross section data. Linear interpolation was performed on the cross section and polarization data taken from references 15, 16, 25, and 74) where necessary to obtain values at the desired energies. Any error introduced by this process should be small compared to the experimental errors because the data were not rapidly changing and the points were closely spaced.

The choice of initial phase shift values for the searches tends to bias somewhat the final results because these phase shifts were known to fit the cross section data. This could have had the effect of beginning the search procedure at or near a minimum in χ^2 -space. In an attempt to locate other χ^2 -minima the range of each of the fixed phase shifts was extended to at least its value at $\delta_0 \pm 15^\circ$. In

the majority of the cases χ^2 continued to increase as the phase shift in question was increased or decreased from its value δ_0 at χ_0^2 . In the few cases where this was not so there were multiple minima, usually two but not more than three. Of these multiple minima cases the worst one was such that the likelihood function for the second minimum was down by a factor $\exp(-7/8)$ from L_0 .

c. Discussion of the Phase Shifts

The results of the phase shift searches are given in Table 5 and are plotted in Figures 5-8. The s-wave phase shifts resemble hard sphere scattering for a radius of 2.8 fermis (1 fermi = 10^{-13} cm) and are plotted in Figure 5. The data above 4.79 MeV do not specify the phase shifts as accurately as at lower energies, as evidenced by the larger error bars.

The p-wave phase shifts are shown in Figure 6. The splitting is the same as that reported in earlier studies, Barnard et al.¹⁵⁾ and Spiger and Tombrello,¹⁶⁾ namely $p_{3/2} > p_{1/2}$. The splitting up to 5.21 MeV is clear, but at higher energies the data again do not specify the phase shifts as well as at lower energies. Various starting phase shifts were used for the p-wave searches, including $p_{1/2} > p_{3/2}$ and $p_{1/2} < p_{3/2}$. In all cases the search procedure resulted in the reported splitting. This is an improvement over the results of Barnard et al.¹⁵⁾ who reported finding two sets of phase shifts, one with $p_{1/2} > p_{3/2}$ and

Table 5. S, P, and F Phase Shifts and Errors for ^4He Elastically Scattered from a Polarized ^3He Gas Target. The equivalent ^3He laboratory energy in MeV is given, accurate to ± 20 keV. The d-waves were set to zero. The errors shown do not include any contribution from systematic errors discussed in Sections III.B.1. and III.B.2.e. Phase shifts and errors are in degrees.

$E_{^3\text{He lab}}$	$S_{1/2}$	$P_{1/2}$	$P_{3/2}$	$F_{5/2}$	$F_{7/2}$
3.30	-22.8 \pm 1.8	161.7 \pm 3.0	165.4 \pm 1.4	0.4 \pm 0.9	2.0 \pm 0.9
3.51	-23.6 0.9	160.9 1.3	163.7 1.0	2.2 0.7	2.1 0.6
3.88	-27.4 0.9	158.5 1.6	161.7 1.2	1.8 0.8	3.0 0.6
4.37	-30.3 1.1	156.1 1.6	157.8 1.2	3.1 0.8	6.7 0.7
4.46	-30.6 1.1	155.8 1.8	157.8 1.3	4.6 0.8	7.3 0.8
4.64	-32.8 1.7	152.8 2.1	157.5 1.2	4.6 1.0	10.1 1.1
4.79	-33.8 1.1	150.7 1.9	156.9 1.6	5.3 0.8	14.8 1.1
4.95	-40.0 6.0	149.7 2.8	153.5 2.4	3.1 1.8	23.4 3.7
5.09	-48.8 7.1	145.5 4.7	153.2 2.7	3.5 1.3	40.2 4.3
5.21	-37.7 4.8	149.1 2.5	153.4 1.9	-2.8 3.1	77.9 4.0
6.04	-50.0 5.3	143.2 2.2	140.6 1.8	8.2 2.4	163.4 2.5
6.46	-44.8 5.2	138.9 2.9	139.6 2.0	15.1 2.8	169.4 1.8
6.86	-48.2 8.8	138.8 3.6	139.9 3.8	17.3 4.1	173.5 3.4

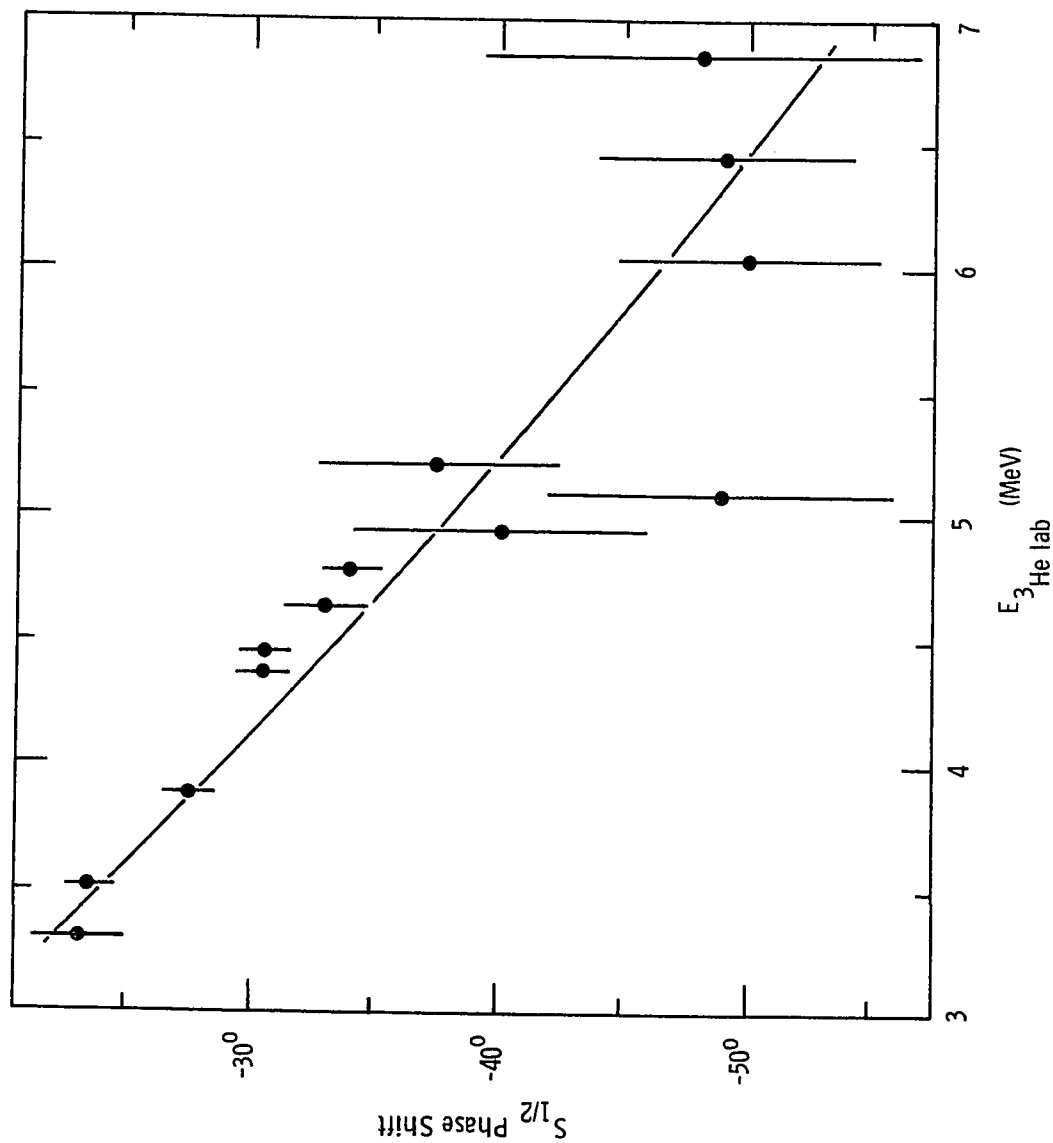


Figure 5. $S_{1/2}$ Phase Shift vs. Equivalent ^3He Laboratory Energy for ^4He Elastically Scattered from a Polarized ^3He Gas Target. The smooth curve represents hard sphere phase shifts for a radius of 2.8 fm.

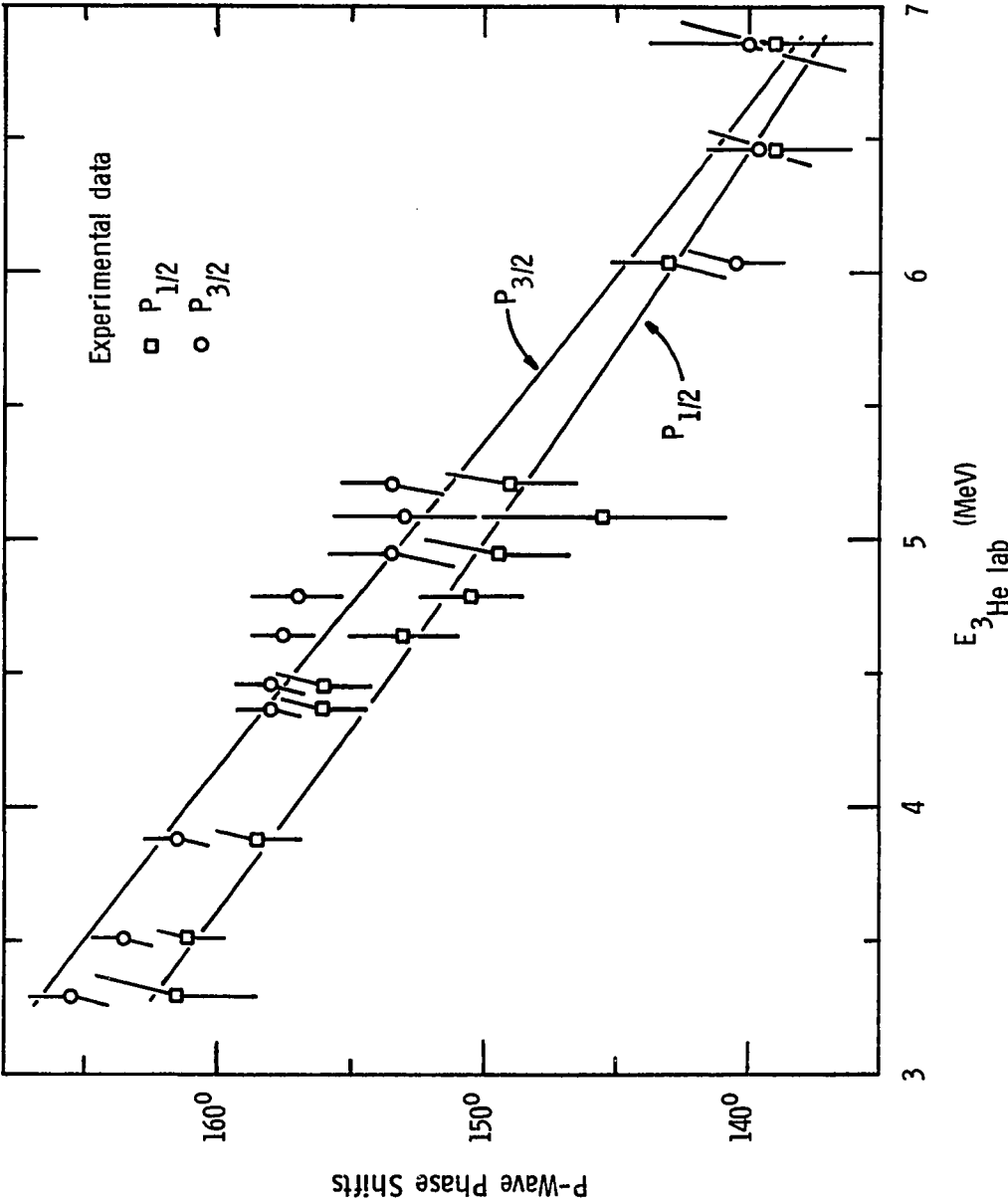


Figure 6. P-Wave Phase Shifts vs. Equivalent ^3He Laboratory Energy for ^4He Elastically Scattered from a Polarized ^3He Gas Target. The smooth curves represent least squares fits to the experimental data using the single level formula of Lane and Thomas which is given in Appendix D.

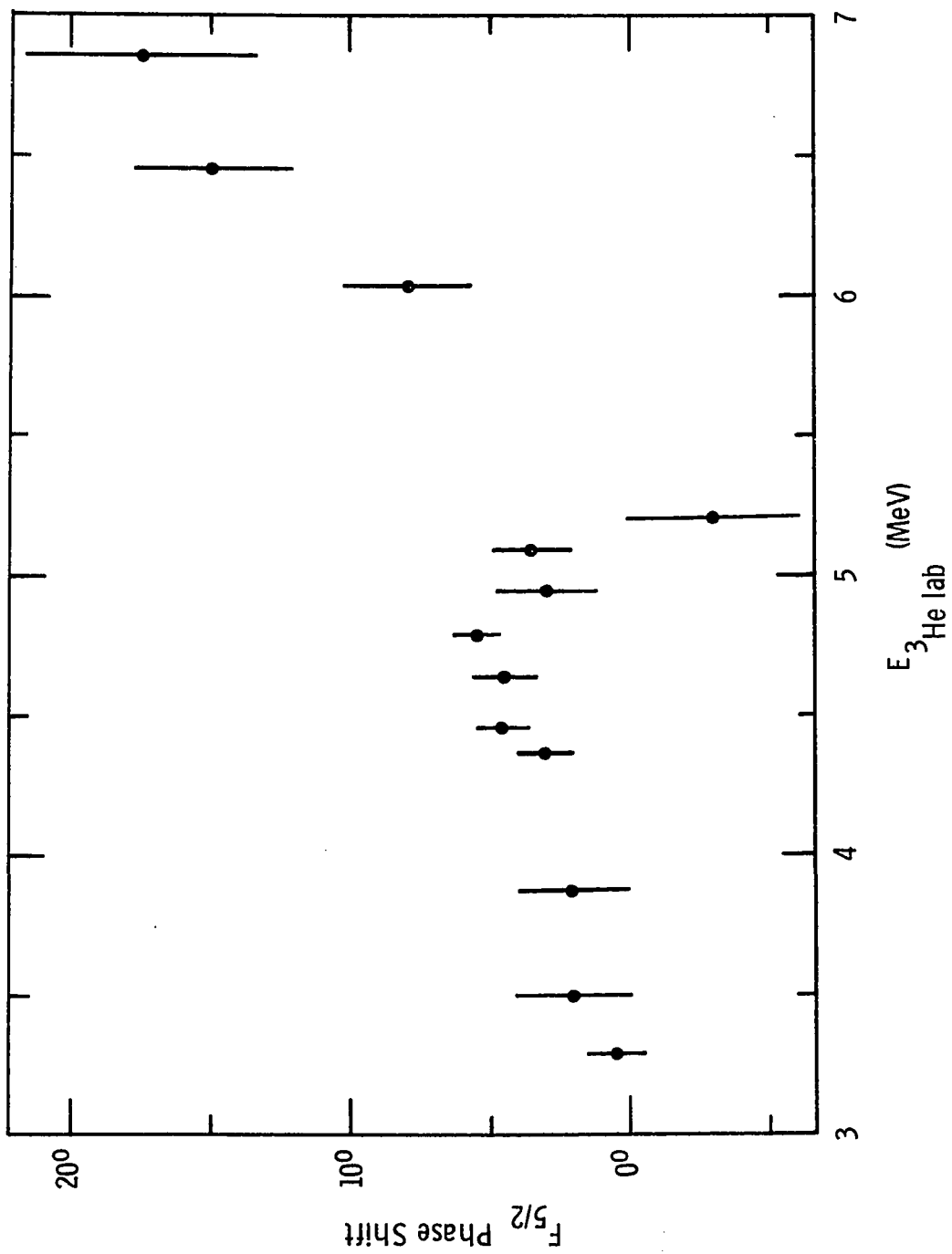


Figure 7. $F_{5/2}$ Phase Shift vs. Equivalent ^3He Laboratory Energy for ^4He Elastically Scattered from a Polarized ^3He Gas Target.

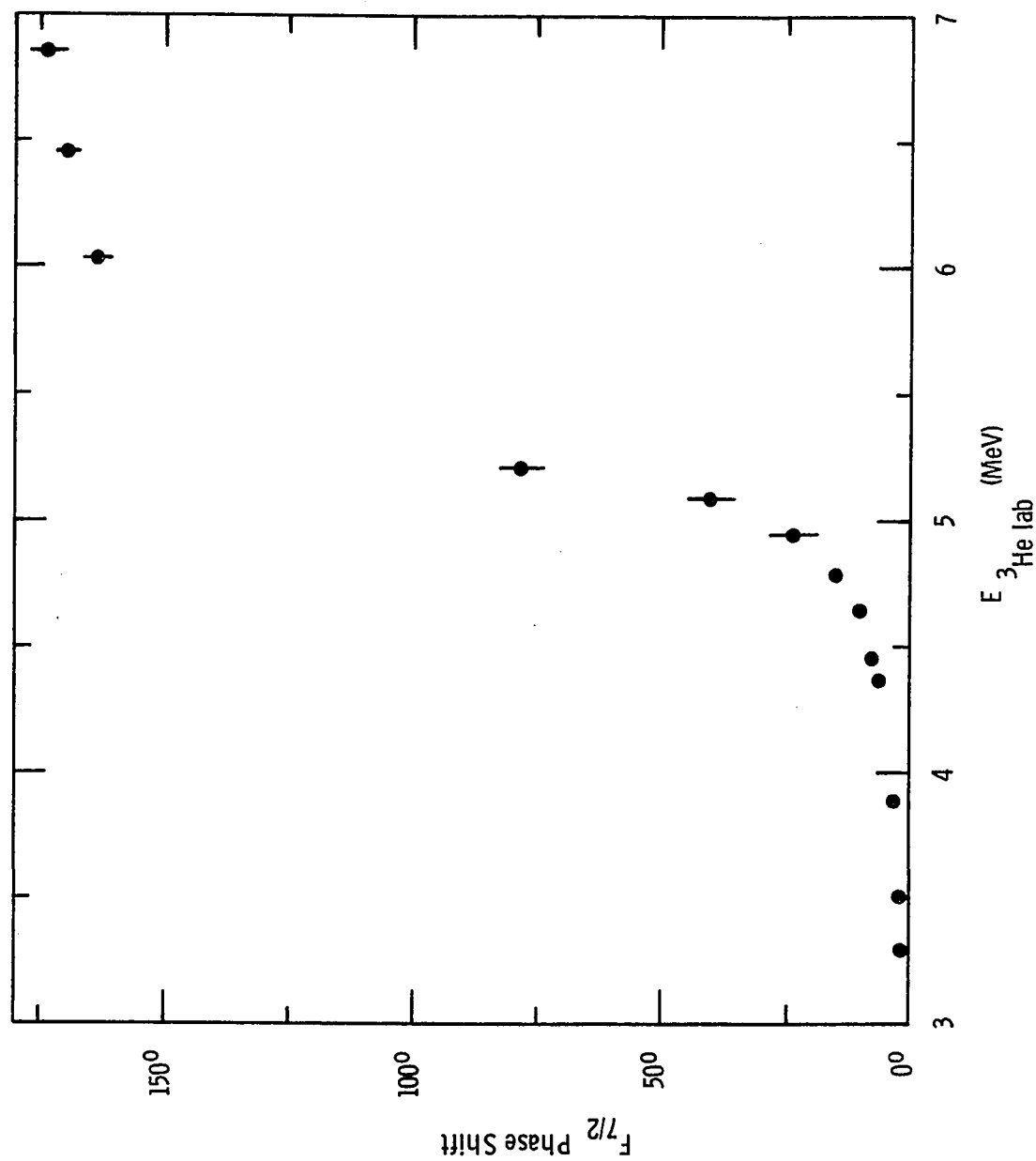


Figure 8. $F_{7/2}$ Phase Shift vs. Equivalent ^3He Laboratory Energy for ^4He Elastically Scattered from a Polarized ^3He Gas Target. Error bars not shown are less than 1° .

one with $p_{1/2} < p_{3/2}$, both of which fit their cross section data about equally well.

When the program was allowed to vary the d-waves typical phase shifts of 0° to $+2^\circ$ were found. It was felt that this reason, along with the discussion in Section III.B.2.a, gave sufficient justification for holding the d-waves constant at zero.

The f-waves are plotted in Figures 7 and 8 and exhibit no unexpected behavior compared to published results.^{15,16)}

d. Effect of Polarization Data on the Phase Shift Analysis

Because other authors have employed only cross section data in their phase shift analyses it seemed instructive to determine the effect of the use of polarization data P_3 on the phase shift searches. Figure 4 is a plot of the values of χ^2 for the $p_{3/2}$ phase shift held fixed at the values shown for $E_{^3\text{He lab}} = 4.64$ MeV. The solid curve is the result of using both cross section and polarization data while the dashed curve is the result of using cross section data alone. The solid curve is smooth and has a single minimum, which was used in Section III.B.2.a to determine the phase shift error. In contrast to this, the dashed curve has several minima, two of which are of approximately the same magnitude. This gives a possible explanation for Bar-nard et al.¹⁵⁾ finding two sets of phase shifts which fit their cross section data. In a few of the phase shift searches the plot of χ^2 had a single minimum when only

cross section data were used. For all such cases χ^2 varied very slowly as the phase shift increased or decreased from δ_0 with several very nearly equal values of χ^2 corresponding to different values of the phase shift. A slowly varying χ^2 would give an undesirably large value of the phase shift error.

The addition of polarization data to the phase shift analysis thus permits a more accurate determination of the phase shifts as well as assignment of a reasonable error. This was especially true at lower energies.

e. Effect of Systematic Cross Section
and Polarization Data Errors on the Phase Shifts

The phase shift errors in Table 5 do not include any effect due to systematic errors in either the polarization data P_3 or the cross section data. Since both types of data could contain systematic errors, the effect of systematic errors on the phase shifts was investigated.

The polarization data P_3 could be in error by as much as $\pm 15\%$ due to uncertainty about the proper value of the parameter f , which are discussed in Section III.A. Multiplying P_3 by 0.85 (corresponding to $f \approx 0.5$) and by 1.1 (corresponding to $f \approx 0.9$) and repeating the phase shift search procedure for both cases had a negligible effect on the phase shifts, usually a few tenths of a degree. The phase shift errors were not affected.

The cross section data reported by Spiger and Tombrello¹⁶⁾ are about 10% greater than those reported by

Barnard et al.¹⁵⁾ Multiplying the cross section data of Barnard by 1.1 and repeating the phase shift search procedure in the range for which their cross section data were used resulted in an average decrease of 3° in the s- and p-waves and an average increase of 1° in the f-waves. Again the phase shift errors were not affected.

3. Nuclear Level Parameters

A single level parameterization of the s- and p-wave phase shifts was made using the R-matrix formalism of Lane and Thomas⁸²⁾ for the phase shifts and the formulas of Jackson and Blatt⁸³⁾ and Buck et al.⁸⁴⁾ for the Coulomb functions. The formulation and the computer program used to perform this analysis are described in Appendix D. For the s-wave the results are plotted as the solid curve in Figure 5 and represent hard sphere phase shifts for a radius of 2.8 fermis. The fits to the p-wave phase shifts are shown as the solid curves in Figure 6.

For both the s- and p-waves the fits to the experimental data are reasonably good. However, no reasonable fits to the f-wave phase shifts could be obtained using the single level formalism. It is quite possible that this failure of the single level formula could be remedied by including additional levels in the formalism.

Values of the nuclear level parameters and their errors have been determined for the $^2P_{1/2}$ and $^2P_{3/2}$ states in the ^7Be system. The method employed was similar to that of the phase shift analysis. The value of the resonance

energy $E_R^{52})$ is presumed to be accurately known and was held constant. The remaining two parameters, the nuclear reaction radius r and the reduced width γ^2 were uniformly varied over a large range. The technique was to vary γ^2 by constant increments over a large range for a given r . Next r was incremented by a constant and the same γ^2 -range repeated. The program was not required to fit the data as in the preceding paragraph, but rather to compute only values of χ^2 and γ^2/γ_0^2 for each value of r and γ^2 , where γ_0^2 is the Wigner limit⁵¹⁾ ($=3\hbar^2/2m_r r^2$) for r , and m_r is the reduced mass. For each value of r a minimum χ^2 was found during the χ^2 stepping process. From this set of minimum χ^2 -values and corresponding parameters r and γ^2/γ_0^2 , the acceptable values r_0 and $(\gamma^2/\gamma_0^2)_0$ were found. As in the case of the phase shifts, the acceptable values are defined as those corresponding to the smallest χ^2 of the set, namely χ_0^2 .

To assign errors to r and γ^2/γ_0^2 a procedure very similar to that used for the phase shift errors was followed, Section III.B.2.a. The likelihood of the best fit r_0 and $(\gamma^2/\gamma_0^2)_0$ was taken as L_0 , equation (1). The errors in r and γ^2/γ_0^2 were defined as those values which reduced the likelihood function L_0 to L_1 , equation (2), corresponding to one standard deviation away from the best fit. With $\chi_1^2 = \chi_0^2 + 1$ as in equation (3), a closed curve is thus defined in r - γ^2/γ_0^2 space for constant χ_1^2 . Such a closed curve or contour is plotted in Figure 9 for the $^2P_{1/2}$ state in ^7Be . From this contour the two extreme values of r , r_H and r_L ,

corresponding to the two ends of the constant x_1^2 contour were used to compute the error in r :

$$r_+ = |r_H - r_0|$$

$$r_- = |r_0 - r_L|$$

Similar relations were used to compute $(\gamma^2/\gamma_0^2)_\pm$ from $(\gamma^2/\gamma_0^2)_H$ and $(\gamma^2/\gamma_0^2)_L$.

In Figure 9 the contour of constant $x_2^2 = x_0^2 + 2$ is shown as the outer contour. This corresponds to the values of the level parameters two standard deviations away from the best fit. The dot inside the inner contour denotes the coordinates r_0 and $(\gamma^2/\gamma_0^2)_0$ at x_0^2 .

In Figure 10 the x_1^2 and x_2^2 contours are plotted for the $^2P_{3/2}$ state in ^7Be and the dot denotes the coordinates at the best fit.

The errors in r and γ^2/γ_0^2 assigned in the foregoing manner do not include any contribution from systematic errors discussed in Section III.B.2.e.

It should be pointed out that only the eight phase shifts up through 4.95 MeV were used to produce the contours shown in Figures 9 and 10. If all 13 phase shifts were used the value of x_0^2 was no less than three times that for the eight lower energy phase shifts. This gave values of $r \approx 4.5$ fm and $\gamma^2/\gamma_0^2 \approx 0.1$, the latter of which appears to be too small. As a point of information $x_0^2(^2P_{1/2})$ was 8.90 and $x_0^2(^2P_{3/2})$ was 4.11.

Table 6. Nuclear Level Parameters for the $^2P_{1/2}$ and $^2P_{3/2}$ States in ^7Be . The values of the resonance energy E_R and J^π are from reference 52). The errors shown for the radius r and ratio of reduced width to Wigner limit γ^2/γ_0^2 do not include any contribution from the systematic errors discussed in Section III.B.2.e.

<u>State</u>	<u>J^π</u>	<u>$E_R(\text{MeV})$</u>	<u>$r(\text{fm})$</u>	<u>γ^2/γ_0^2</u>
$^2P_{1/2}$	$1/2^-$	-1.155	$3.51 \begin{smallmatrix} + 0.28 \\ - 0.22 \end{smallmatrix}$	$0.283 \begin{smallmatrix} + 0.049 \\ - 0.079 \end{smallmatrix}$
$^2P_{3/2}$	$3/2^-$	-1.587	$3.22 \begin{smallmatrix} + 0.23 \\ - 0.27 \end{smallmatrix}$	$0.295 \begin{smallmatrix} + 0.048 \\ - 0.060 \end{smallmatrix}$

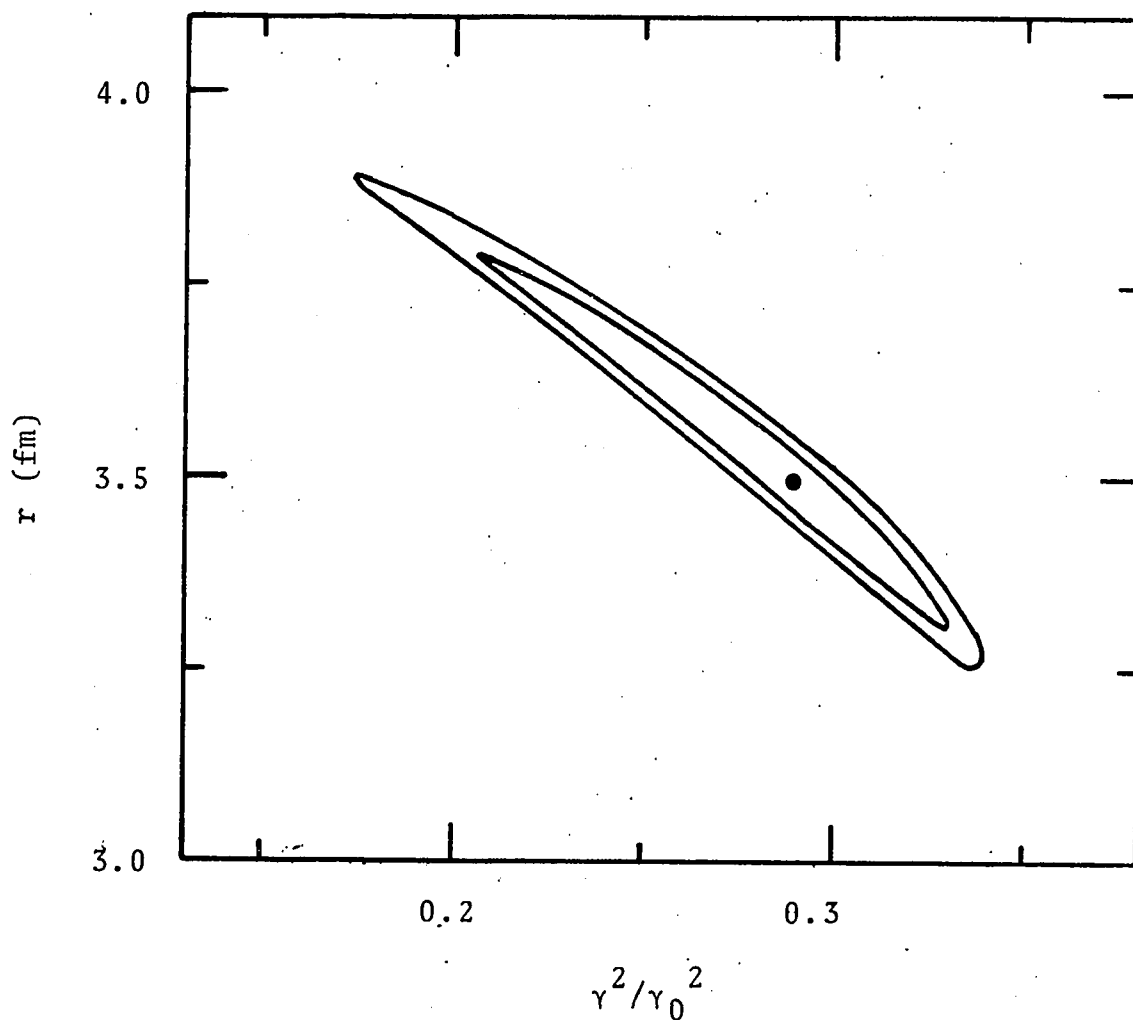


Figure 9. Contours of Constant χ^2 in Parameter Space Used to Determine Nuclear Level Parameters r_0 , $(\gamma^2/\gamma_0^2)_0$, and Errors for ${}^2P_{1/2}$ State in ${}^7\text{Be}$. The inner and outer contours represent constant χ^2 corresponding to values of the level parameters one and two standard deviations, respectively, from the best fit at χ_0^2 . The dot denotes the coordinates r_0 and $(\gamma^2/\gamma_0^2)_0$ at the best fit.

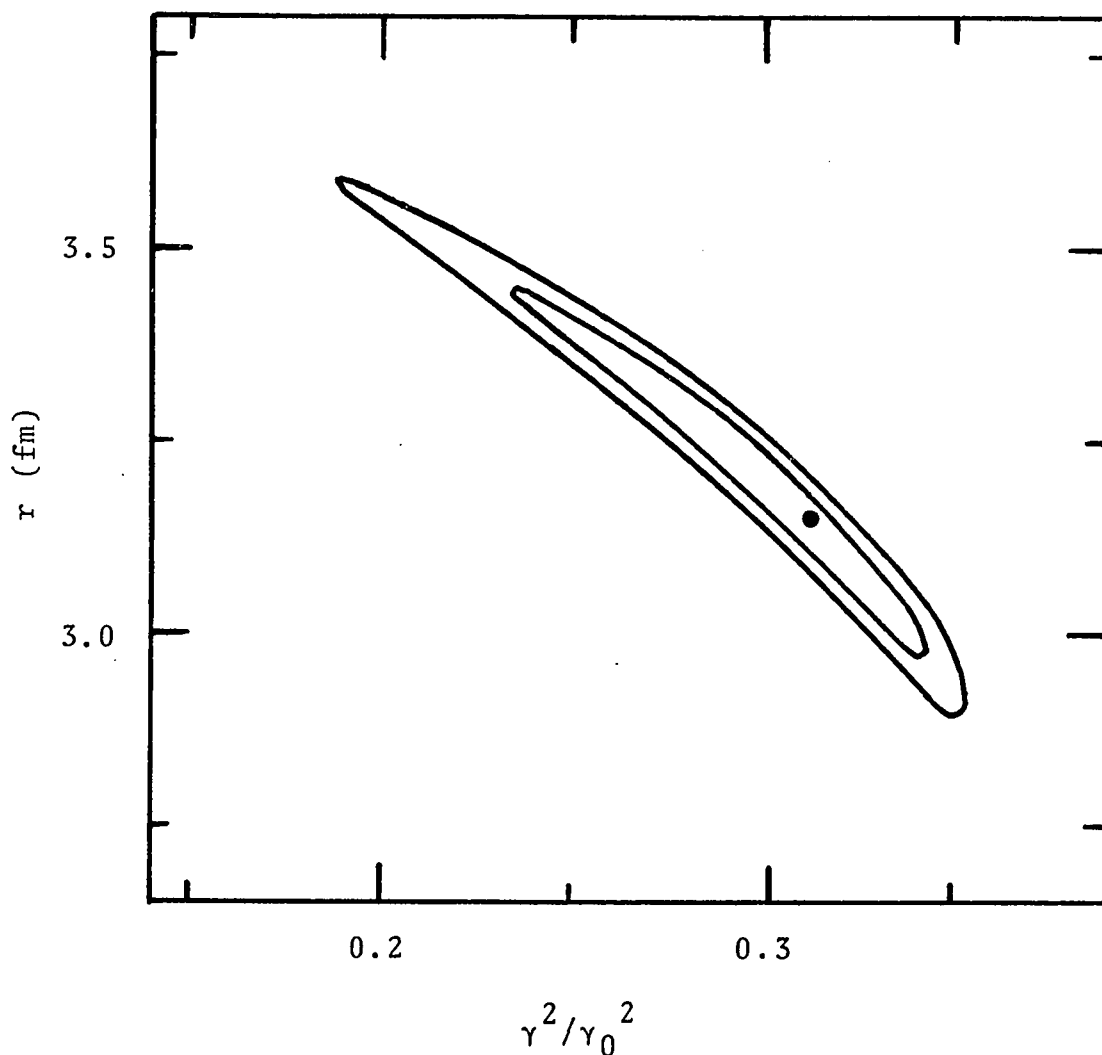


Figure 10. Contours of Constant χ^2 in Parameter Space Used to Determine Nuclear Level Parameters r_0 , $(\gamma^2/\gamma_0^2)_0$, and Errors for ${}^2P_{3/2}$ State in ${}^7\text{Be}$. The inner and outer contours represent constant χ^2 corresponding to values of the level parameters one and two standard deviations, respectively, from the best fit at χ_0^2 . The dot denotes the coordinates r_0 and $(\gamma^2/\gamma_0^2)_0$ at the best fit.

Table 6 gives the values of r_0 and $(\gamma^2/\gamma_0^2)_0$ and their errors. The values of E_R are the excitation energies of the two lowest lying states in ${}^7\text{Be}$ ($3/2^-$ and $1/2^-$) and are referenced to the ${}^3\text{He}$ - ${}^4\text{He}$ threshold as zero.⁵²⁾

C. Scattering of ${}^3\text{He}$ from a Polarized ${}^3\text{He}$ Gas Target

1. ${}^3\text{He}$ - ${}^3\text{He}$ Elastic Scattering

The experimental asymmetry A and reaction analyzing power P_3 have been measured for ${}^3\text{He}$ elastically scattered from a polarized ${}^3\text{He}$ gas target at $\theta_{\text{cm}} = 60.0^\circ$ for 12 bombarding energies between 4.33 and 9.83 MeV. Table 7 gives A and P_3 and in Figure 11 the values of P_3 and ΔP_3 are plotted as a function of ${}^3\text{He}$ bombarding energy. The error ΔP_3 does not include any effect due to systematic error in the target polarization discussed in Section III.A.

P_3 is small, of the order of -2% to +2%, except for two points at 8.77 and 9.83 MeV where it is about -8%. Sufficient data were taken at each energy to produce at least two values of P_3 and from these a weighted average was computed as explained in Appendix B.

There is reason to doubt the values of P_3 at 9.79 and 9.83 MeV (Table 7 and Figure 11) because they are of the opposite sign. This in turn leads one to question the value of P_3 at 8.77 MeV because the values on each side of this are much smaller, though of the same sign.

The instrumental asymmetry A_0 was calculated at each energy and was found to be no larger than 0.4% which is considered good. As can be seen from Table 7 the data on the two runs were taken at alternating energy values and tend to agree well except at the two points previously noted.

No background correction was made because the scattered particle peaks were well defined and background events were no more than 1.5% of the total events under a given peak. The correction for 1.5% background causes a negligible change in A and P_3 compared to the statistical errors.

2. ^3He - ^3He Inelastic Scattering

The experimental asymmetry A and reaction analyzing power P_3 have been measured for the breakup protons produced by the inelastic reaction $^3\text{He}(^3\text{He},p)^5\text{Li}$ (ground state) at $\theta_{\text{lab}} = 30.0^\circ$. These results are given in Table 8 and P_3 with error bars ΔP_3 is plotted as a function of ^3He bombarding energy in Figure 12. The error ΔP_3 does not include any effect due to systematic error in the target polarization discussed in Section III.A.

The Q -value for this reaction is 10.89 MeV and as a result the maximum proton energy for the experiment was about 17.8 MeV. In order to register the ejected protons on the pulse height analyzer it was necessary to degrade their energy by placing a 0.013 in. aluminum plate in front of each detector. In addition to moving the peak to a lower energy this had the effect of causing a large spread in energy for the detected protons.

Tables 7 and 8. Experimental Asymmetry A and Reaction Analyzing Power P_3 for ^3He Scattered from a Polarized ^3He Gas Target. The sequence numbers allow correlation of A and P_3 with the target polarization p in Tables 2 and 3. The ^3He bombarding energy in MeV is shown, accurate to ± 20 keV. Where several data exist at a single energy point a weighted average (denoted by $\langle \rangle$) is computed for A, the statistical error ΔA , P_3 and ΔP_3 as explained in Appendix B. ΔP_3 does not include any systematic error due to uncertainty in f (Section III.A.). Each table is identified by its run number, the center-of-mass or laboratory angle, and the nuclear reaction being carried out during the run.

Table 7. Experimental Asymmetry and Reaction Analyzing Power, Runs 1 and 3, ${}^3\text{He}({}^3\text{He}, {}^3\text{He}){}^3\text{He}$, $\theta_{\text{cm}} = 60.0^\circ$. The corresponding target polarization data are given in Table 2.

Seq.	Energy	A	<u><A></u>	<u>ΔA</u>	Run 1	<u>P₃</u>	<u><P₃</u>	<u>ΔP_3</u>	<u><ΔP_3></u>
1	4.89	0.0164		0.0066		0.1310		0.0531	
16		-0.0015		0.0024		-0.0136		0.0216	
17		0.0017		0.0029		0.0155		0.0260	
18		-0.0030		0.0022		-0.0258		0.0188	
2	6.01	-0.0002	-0.0005	0.0033	0.0014	-0.0015	-0.0048	0.0252	0.0121
3		-0.0038		0.0038		-0.0305		0.0300	
11		0.0003		0.0022		0.0021		0.0144	
12		-0.0055		0.0021		-0.0400		0.0154	
4	7.11	0.0011	-0.0024	0.0039	0.0013	0.0088	-0.0165	0.0303	0.0092
13		0.0010		0.0025		0.0080		0.0194	
14		0.0001		0.0024		0.0008		0.0197	
15		-0.0028		0.0020		-0.0224		0.0159	
5	8.21	-0.0077	-0.0006	0.0033	0.0012	-0.0607	-0.0054	0.0263	0.0098
6		0.0048		0.0031		0.0407		0.0263	
10		0.0017		0.0037		0.0148		0.0325	
19		-0.0012		0.0025		-0.0102		0.0209	
26		0.0032		0.0031		0.0264		0.0256	
27		-0.0014		0.0031		-0.0116		0.0254	
7	9.25	-0.0120	-0.0001	0.0044	0.0012	-0.1030	-0.0016	0.0378	0.0104
8		-0.0063		0.0043		-0.0573		0.0397	
9		-0.0069		0.0044		-0.0627		0.0397	
20		0.0053		0.0041		0.0436		0.0341	
21		-0.0047		0.0040		-0.0418		0.0355	
28		0.0009	-0.0032	0.0032	0.0016	0.0076	-0.0263	0.0264	0.0140

Table 7 (Continued).

Seq.	Energy	A	$\langle A \rangle$	ΔA	Run 1 (Cont.)		$\overline{P_3}$	$\langle P_3 \rangle$	$\overline{\Delta P_3}$	$\langle \Delta P_3 \rangle$
22	9.79	0.0077		0.0040			0.0583		0.0303	
23		0.0083		0.0042			0.0754		0.0382	
24		0.0132		0.0037			0.1193		0.0337	
25		-0.0045		0.0037			-0.0359		0.0301	
29		0.0023		0.0033			0.0195		0.0275	
30		-0.0013		0.0033			-0.0102		0.0264	
31		-0.0005		0.0034			-0.0043		0.0282	
			0.0031		0.0013			0.0240		0.0113
Run 3										
4	4.33	0.0008		0.0030			0.0069		0.0257	
5		0.0034		0.0029			0.0296		0.0249	
6		-0.0081		0.0032			-0.0651		0.0258	
1	5.48	0.0045		0.0029		0.0017	0.0275	-0.0085	0.0176	0.0147
2		-0.0036		0.0032			-0.0265		0.0234	
3		-0.0065		0.0032			-0.0514		0.0259	
7	6.59	-0.0007		0.0036		0.0018	-0.0058	-0.0055	0.0277	0.0123
8		-0.0063		0.0034			-0.0566		0.0310	
9	7.67	0.0058		0.0036		0.0025	0.0468	-0.0284	0.0296	0.0206
10		-0.0030		0.0038			-0.0269		0.0340	
11	8.77	-0.0078		0.0037		0.0026	-0.0785	0.0150	0.0377	0.0223
12		-0.0074		0.0037			-0.0664		0.0338	
13	9.83	-0.0232		0.0039		0.0026	-0.2034	-0.0718	0.0356	0.0251
14		0.0049		0.0040			0.0416		0.0345	
			-0.0096		0.0028			-0.0770		0.0247

Table 8. Experimental Asymmetry and Reaction Analyzing Power, Run 4, ${}^3\text{He}({}^3\text{He}, p){}^5\text{Li}$ (ground state), $\theta_{\text{lab}} = 30.0^\circ$. The corresponding target polarization data are given in Table 3.

Seq.	Energy	<u>A</u>	<u><A></u>	<u>ΔA</u>	<u><ΔA></u>	<u>P₃</u>	<u><P₃></u>	<u>ΔP_3</u>	<u><ΔP_3></u>
1	6.06	0.0481		0.0162		0.4576		0.1596	
6		0.0055		0.0104		0.0568		0.1074	
7	7.16	-0.0136	0.0178		0.0087		0.1876		0.0891
8		-0.0233		0.0095		-0.1133		0.0787	
9		0.0058		0.0089		-0.2247		0.0864	
10		-0.0050		0.0079		0.0560		0.0764	
11		0.0307		0.0079		-0.0508		0.0806	
12		0.0117		0.0078		0.3157		0.0817	
				0.0081		0.1174		0.0815	
2	7.28	0.0020	0.0029		0.0034		0.0199		0.0329
3	7.79	-0.0041		0.0209		0.0186		0.1925	
4	8.23	-0.0470		0.0264		-0.0376		0.2396	
5		-0.0074		0.0305		-0.4405		0.2858	
			-0.0256			-0.0666		0.2547	
				0.0207			-0.2321		0.1908

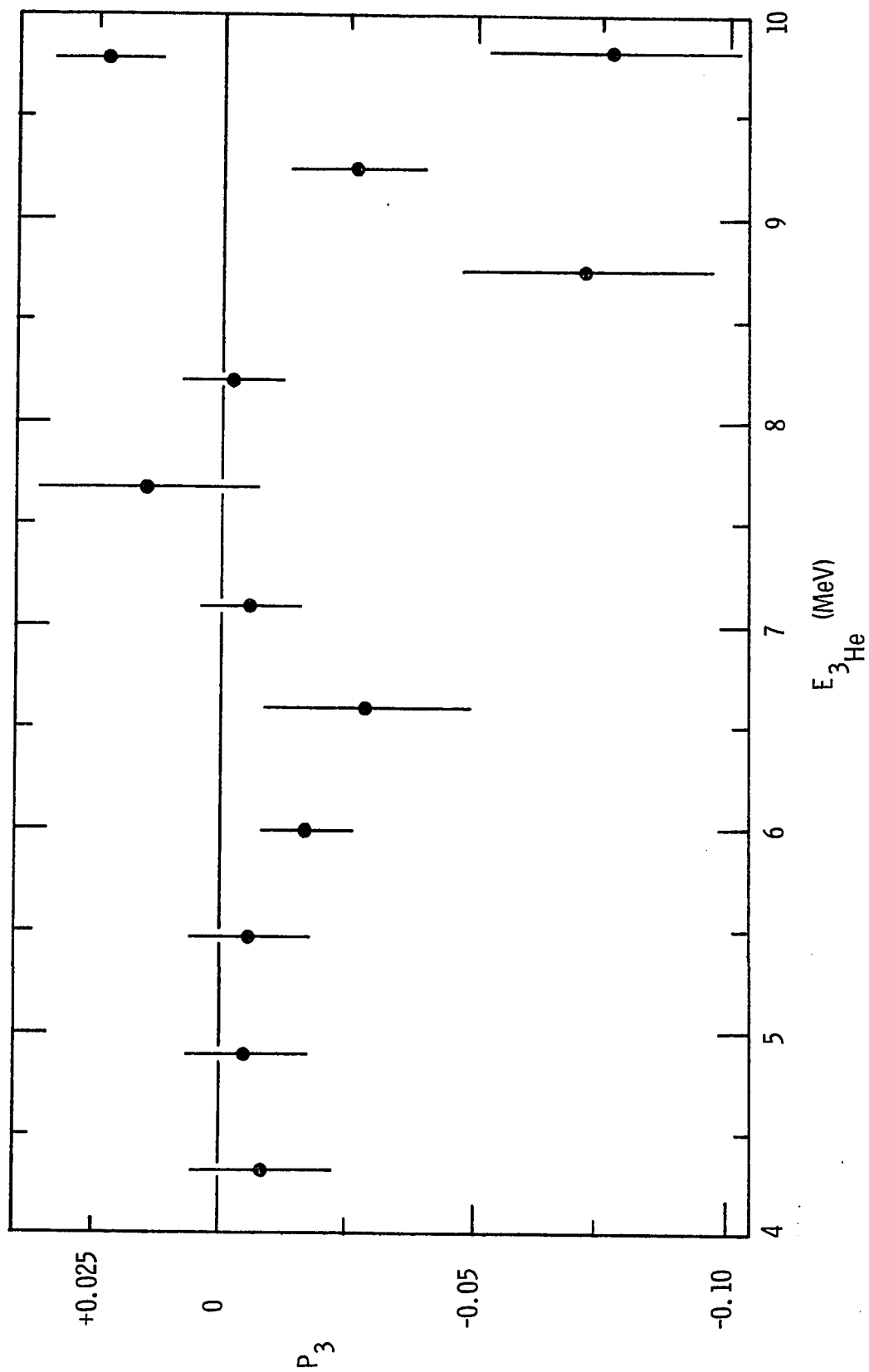


Figure 11. Reaction Analyzing Power vs. ^3He Bombarding Energy for ^3He Elastically Scattered from a Polarized ^3He Gas Target, $\theta_{\text{cm}} = 60.0^\circ$.

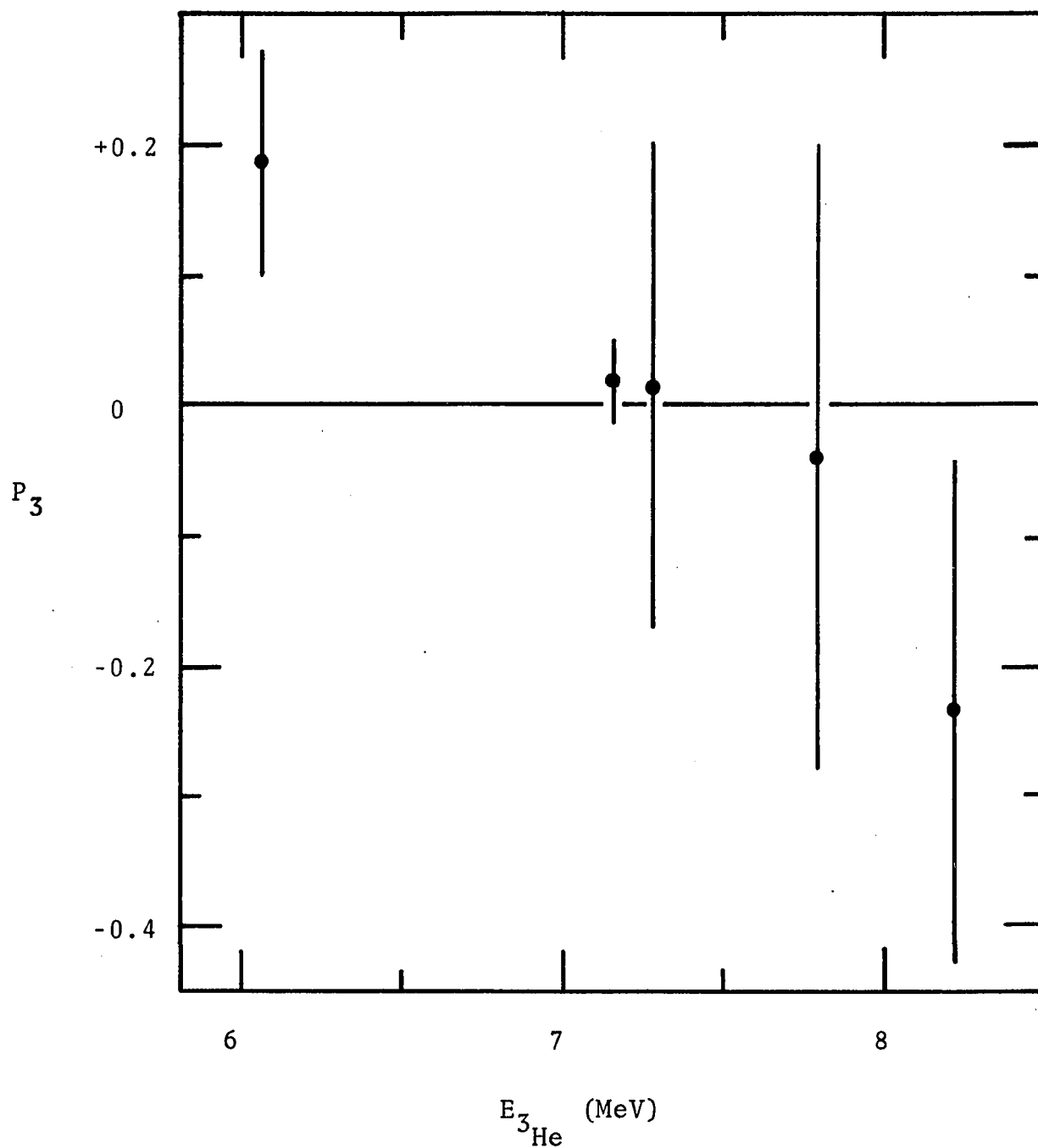


Figure 12. Reaction Analyzing Power vs. ^3He Bombarding Energy for Breakup Protons Produced by $^3\text{He}(^3\text{He},p)^5\text{Li}$ (ground state) at $\theta_{\text{lab}} = 30.0^\circ$.

The results of this experiment are inconclusive for a number of reasons. There are only five values of P_3 and with one exception these all have large errors, making it difficult to discern a definite trend. The background was large, with a maximum value of 25-30% of the total events under some peaks. By adjusting the number of counts under each peak to reduce the effect of background it was possible to get almost any desired value for P_3 from the data. Also the instrumental asymmetry A_0 was as high as 3.5%. The use of the aluminum plate to reduce the proton energy moved the peak down the energy scale to a point where background was high. This difficulty could be eliminated by using a pulse height analyzer capable of registering the higher energy particles.

IV. CONCLUSIONS AND SUGGESTIONS FOR FUTURE WORK

The inclusion of polarization data in the phase shift analysis of ^3He - ^4He elastic scattering data permits a more accurate determination of the elastic scattering phase shifts than that resulting from the use of cross section data alone. It also allows reasonable errors to be assigned to the phase shifts. This was especially true at lower bombarding energies where the phase shift errors were of the order of 1° . At higher energies ($E_{^3\text{He lab}} > 4.95 \text{ MeV}$) the data did not specify the phase shifts as accurately as at lower energies, resulting in larger errors in the phase shifts.

The s-wave phase shifts can be described by hard sphere scattering for a radius of 2.8 fm. A single level parameterization of the p-wave phase shifts gives acceptable fits to the experimental data. It also produces reasonable values of the nuclear reaction radius and ratio of reduced width to Wigner limit for the $^2P_{1/2}$ and $^2P_{3/2}$ states in ^7Be . The d-wave phase shifts were set to zero because of the absence of known d-states in the ^7Be system and the fact that even at higher energies these are zero. The f-wave phase shifts exhibit no unexpected behavior compared to published results.

The results of this experiment suggest further experimental and theoretical work. Due to the small amount of data which exists from ^3He and ^4He scattering using a polarized ^3He target, future experimental work could provide both elastic and inelastic scattering data at a number of angles and bombarding energies. More data would perhaps

better define the ${}^3\text{He}$ - ${}^4\text{He}$ elastic scattering phase shifts for $E_{{}^3\text{He lab}} > 4.95$ MeV. More data could also provide experimental verification of polarization contour maps such as Figure 3. These data could be easily obtained if a target cell with large angle windows such as is discussed in Appendix E could be perfected. Because the present data do not clearly define P_3 for the protons produced by ${}^3\text{He}({}^3\text{He}, p){}^5\text{Li}$ (ground state) this part of the experiment should be repeated and extended using a better pulse height analyzer to eliminate the problem of high background.

In the data analysis the failure of the single level formalism to fit the f-wave phase shifts needs further work. The next step is to try a two level formula. If a reasonable fit could be accomplished then level parameters for the ${}^2F_{5/2}$ and ${}^2F_{7/2}$ states in ${}^7\text{Be}$ could be determined with confidence.

No attempt was made to apply the theory of the resonating group calculations reported in the literature for ${}^3\text{He}$ - ${}^3\text{He}$ and ${}^3\text{He}$ - ${}^4\text{He}$ elastic scattering.⁸⁵⁻⁸⁷⁾ The published results which utilized the resonating group method attempted to fit only cross section data using the elastic exit channel and it is not clear whether this method has any provision for fitting polarization data also. Further investigation of this method to determine its applicability, if any, to the current work is warranted.

APPENDIX A. OPTICAL MEASUREMENT OF TARGET POLARIZATION

1. Method

Colegrove, Schearer, and Walters⁸⁾ have developed a method for optically measuring target polarization. Their method consists of an optical measurement of the metastable polarization, and because of the tight coupling between the metastable and ground state systems, this is equivalent to a measurement of the ground state polarization. The $2^3S_1 - 2^3P_0$ pumping light absorbed by the metastables for $\Delta m = +1$ and ground state polarization p is⁶⁵⁾

$$I(p) = n_1 a f(1-p) + n_2 b f(1-p) + n_3 b f p + n_4 a f p \\ + n_5 c(1-f)(1-p) + n_6 c p(1-f).$$

In this equation the various factors are:

n_i	steady state solutions for magnetic sublevel populations. See Figure 1 and reference 8).
$n_1 = n_{-3/2}$	$= n(1-p)^3 / (6+2p^2)$
$n_2 = n_5 = n_{-1/2}$	$= n(1+p)(1-p)^2 / (6+2p^2)$
$n_3 = n_6 = n_{+1/2}$	$= n(1+p)^2(1-p) / (6+2p^2)$
$n_4 = n_{+3/2}$	$= n(1+p)^3 / (6+2p^2)$
n	metastable density
p	target polarization
a, b, c	relative electric dipole transition probabilities between $2^3S_1 - 2^3P_0$ magnetic sublevels

f	ratio of pumping light intensity producing $m_F = 3/2$ to $m_F = 1/2$ transitions to total pumping light intensity
p	fraction of circularly polarized pumping light in wrong sense.

Using the values of the magnetic sublevel populations, $I(p)$ can easily be put in the form

$$I(p) = \frac{n}{6+2p^2} \{af[(1-p)^3 + 2p\rho(3+p)^2] + (1-p^2)[bf + c(1-f)][p(2\rho-1) + 1]\}. \quad (A1)$$

In the work of Colegrove, Schearer, and Walters⁸⁾ and that of Greenhow⁶³⁾ the formulas used to compute $I(p)$ are idealized cases in which complete knowledge of the transition probabilities and of the pumping light spectrum was assumed. The pumping light was also taken to be completely circularly polarized and parallel to the polarization axis. Equation (A1) is a modified form of that reported in references 8 and 63) to allow for uncertainties in transition probabilities, pumping light spectrum, and pumping light polarization.⁶⁵⁾ It is still assumed that the pumping light is parallel to the polarization axis.

In order to determine p optically the quantity

$$\frac{\delta I(p)}{I(p)} = \frac{I(p) - I(-p)}{I(p)} \quad (A2)$$

was measured, thus eliminating the unknown metastable density n . (See Figure 13.) This is the same method as that of Colegrove, et al.,⁸⁾ except that the target polarization is reversed instead of destroyed in the measurement process. $I(p)$ was measured by turning the weak electric field (which creates metastable ^3He atoms) off and noting the change in transmitted light, since there is no absorption when there are no metastable ^3He atoms. The metastable relaxation time ($\sim 2 \times 10^{-4}$ sec) is short compared to the time required to measure $I(p)$ (~ 10 sec). $\delta I(p)$ was measured by monitoring the change in transmitted light as the nuclear polarization was adiabatically reversed, following reversal of the magnetic field direction.

Physically these measurements were accomplished in the following manner. The weak electric field was switched off and on twice, providing four readings. This was necessary to minimize statistical errors, since individual signals fluctuated. This gave $I(p) = I_{b_j}$, $j = 1, 2, 3, 4$, in Figure 14. Next the magnetic field was twice reversed and restored to its original direction, giving $\delta I(p) = \delta I_j$. Finally the I_{a_j} were determined in the same manner as the I_{b_j} .

It was noted that polarization decreased during the measurement of $\delta I(p)/I(p)$ in a manner somewhat proportional to the number of times $\delta I(p)$ was measured. McSherry⁸⁸⁾ discusses this and gives three possible causes of polarization loss, namely depolarization when the ^3He spins are oriented in one direction and the ^4He light is pumping in the

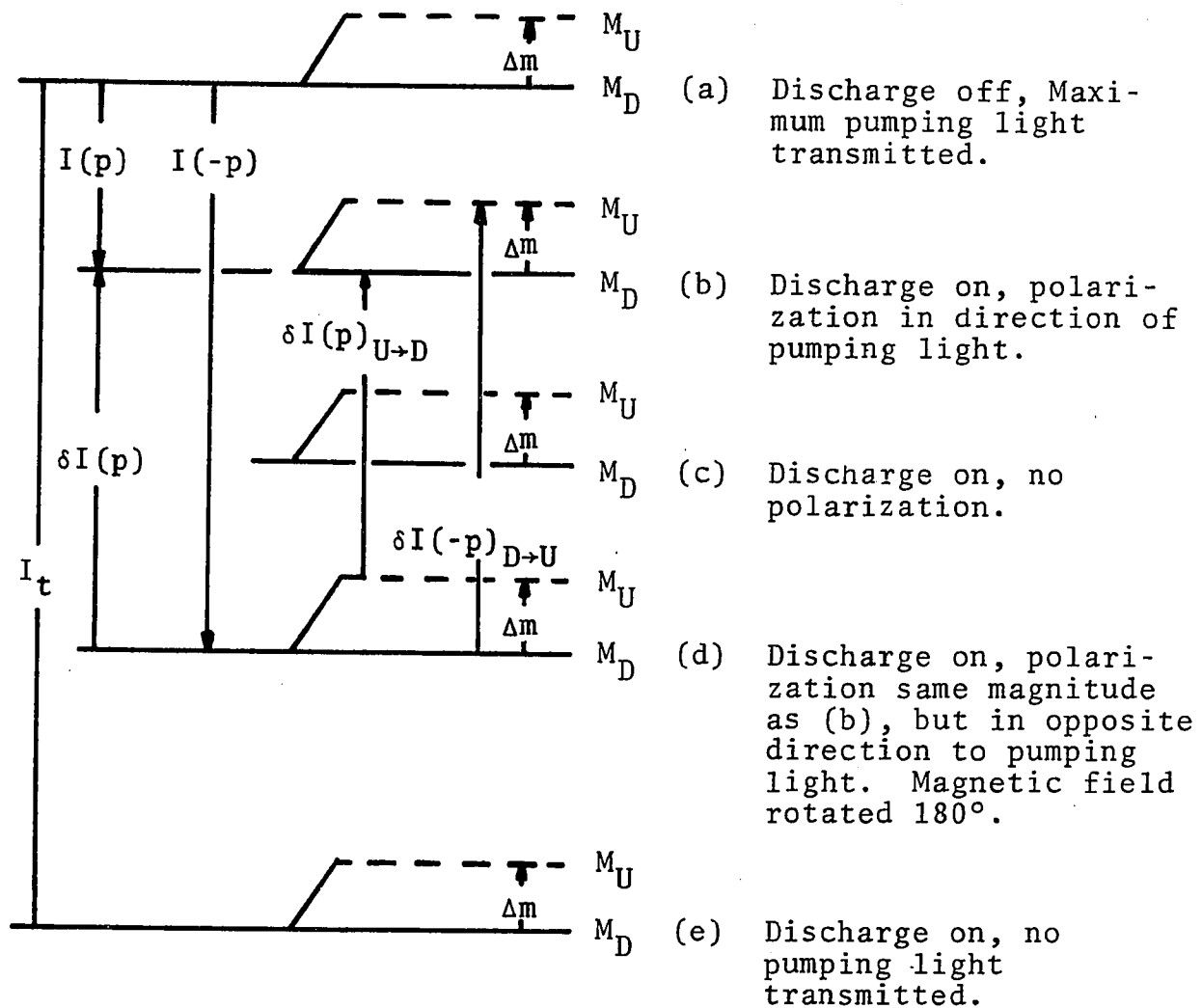


Figure 13. Optical Pumping Light Intensity Level Diagram and Interpretation of Optical Signals Observed During Measurement of Target Polarization. I_t is the maximum absorbed pumping light; M_U and M_D refer to magnetic field directions up or down. The other symbols are defined in the text. (Adapted from reference 88.)

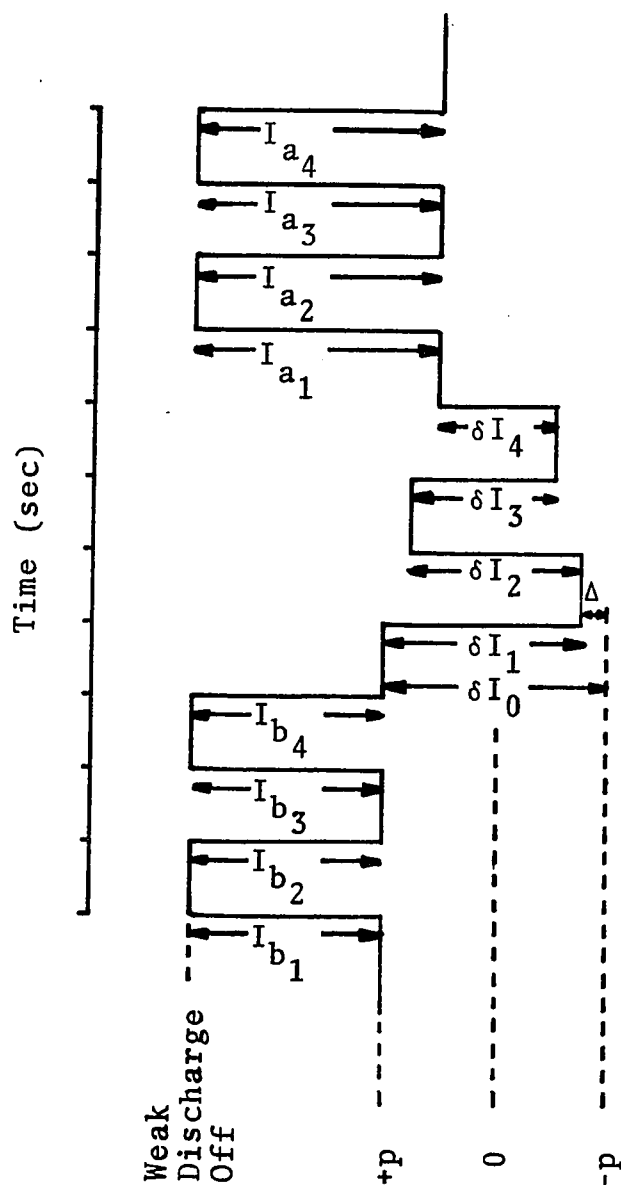


Figure 14. Idealized Optical Pumping Signals With No Repumping Used to Compute Target Polarization p . The polarization loss Δ during the measurement process is shown. See Figure 13. (Adapted from reference 88.)

opposite direction, significant increase in magnetic field gradient relaxation during rotation of the magnetic field, and nonadiabatic rotation of the magnetic field. Of these gradient relaxation is thought to be the most serious, and the only one for which corrections are made. The method is as follows.

If a loss of polarization Δ occurs during each of the four measurements of $\delta I(p)$ the average $\langle \delta I \rangle$ will be

$$\langle \delta I \rangle = \delta I_0 - 4\Delta \quad (A3)$$

where δI_0 is the true absorption signal during the measuring process. The loss in polarization can also be written

$$4\Delta = \langle I_a \rangle - \langle I_b \rangle$$

which can be combined with equation (A3) to yield

$$\frac{\delta I_0}{\langle I_b \rangle} = \frac{\langle \delta I \rangle + \langle I_a \rangle - \langle I_b \rangle}{\langle I_b \rangle} = \langle \frac{\delta I}{I} \rangle. \quad (A4)$$

$\langle \delta I/I \rangle$ was found for each combination of magnetic field direction (first letter of each of the following pairs) and target polarization direction (second letter of each pair, abbreviated UU, UD, DU, DD, and denoted by $i = 1, 2, 3, 4$, respectively). Thus

$$\langle I_b \rangle_i = \frac{1}{4} \sum_{j=1}^4 I_{b_j}$$

$$\langle I_a \rangle_i = \frac{1}{4} \sum_{j=1}^4 I_{a_j}$$

$$\langle \delta I \rangle_i = \frac{1}{4} \sum_{j=1}^4 \delta I_j.$$

The average ratio, equation (A4), for each combination is

$$\langle \frac{\delta I}{I} \rangle_i = \frac{\langle \delta I \rangle_i + \langle I_a \rangle_i - \langle I_b \rangle_i}{\langle I_b \rangle_i} \equiv T_i \quad (A4a)$$

and the average for all four combinations is

$$\langle \frac{\delta I}{I} \rangle = \frac{1}{4} \sum_{i=1}^4 \langle \frac{\delta I}{I} \rangle_i. \quad (A5)$$

As a check on the accuracy of the data I_b and I_a , the best estimates of the standard deviations for these quantities were calculated, σ_{b_i} and σ_{a_i} , respectively. These were found to be typically 1-2% except near the end of the useful life of the target cell at which time they could be as high as 15%. This was due to the fact that the polarization was small and readings from such data as Figure 14 were noisy and small in magnitude.

The error in $\langle \delta I/I \rangle_i$ is given by

$$\begin{aligned} (\Delta \langle \frac{\delta I}{I} \rangle_i)^2 &= (\Delta T_i)^2 = \left(\frac{\partial T_i}{\partial \langle \delta I \rangle_i} \Delta \langle \delta I \rangle_i \right)^2 \\ &+ \left(\frac{\partial T_i}{\partial \langle I_a \rangle_i} \Delta \langle I_a \rangle_i \right)^2 + \left(\frac{\partial T_i}{\partial \langle I_b \rangle_i} \Delta \langle I_b \rangle_i \right)^2 \end{aligned}$$

$$\Delta \left\langle \frac{\delta I}{I} \right\rangle_i = \left(\frac{\epsilon^2 + \sigma_{a_i}^2}{\langle I_b \rangle_i^2} + \frac{(\langle \delta I \rangle_i^2 + \langle I_a \rangle_i^2) \sigma_{b_i}^2}{\langle I_b \rangle_i^4} \right)^{1/2} \quad (A6)$$

where $\Delta \langle \delta I \rangle_i$ has been taken as a constant ϵ , and $\Delta \langle I_b \rangle_i$ and $\Delta \langle I_a \rangle_i$ have been replaced by their respective standard deviations, σ_{b_i} and σ_{a_i} . The constant error ϵ in reading the δI_j from the chart recorder was taken as 0.2 mm; the smallest division on the chart recorder paper was 1.0 mm. The error in the ratio $\langle \delta I/I \rangle$, equation (A5) is found using equation (A6).

$$\Delta \left\langle \frac{\delta I}{I} \right\rangle = \frac{1}{4} \sum_{i=1}^4 \Delta \left\langle \frac{\delta I}{I} \right\rangle_i \quad (A7)$$

The best estimate of the standard deviation of the $\langle \delta I/I \rangle_i$ was also calculated and found to be of the order of 10% except near the end of the cell life where it was as high as 25% for the reasons previously given. A standard deviation of 10% is not unexpected since the magnetic field had a significant effect on the ^4He lamp intensity.

Figure 14 is an idealized trace of the optical signals measured showing the polarization loss Δ and no repumping. In practice it was found that the I_{a_j} were larger than the I_{b_j} similar to Figure 14, though there was fluctuation in individual readings. Figure 13 can be interpreted as a schematic interpretation of the light absorption signals shown in Figure 14. The various parameters used in relating pumping light absorbed to the polarization are shown.

The shifts in light intensity level due to the external magnetic field effect are labeled M_U and M_D .

2. Calculation of p from $\langle \delta I/I \rangle$

It would be difficult to invert equation (A1) to find p as a function of $I(p)$. A simple and more direct approach was developed by noting that on a plot of p vs. $\delta I/I$ (which can be easily generated by equations (A1) and (A2)) the curve has a slight convex curvature⁷¹⁾ and can be approximated by a straight line in several regions. By restricting consideration to the region of $8\% \leq p \leq 15\%$, equation (A8) was found to hold

$$p = \frac{\langle \frac{\delta I}{I} \rangle - W}{S} \quad (A8)$$

where S is the slope of the p vs. $\delta I/I$ curve and W is the $\langle \delta I/I \rangle$ intercept for the region under consideration. To find the polarization corresponding to a given $\langle \delta I/I \rangle$ measurement, p was computed from equation (A8) and reduced by a constant (5×10^{-4}). This value of p was then used in equation (A2) to give a value of $\delta I(p)/I(p)$. By using a reduced p , the calculated value of $\delta I(p)/I(p)$ was initially less than the measured $\langle \delta I/I \rangle$. Then p was incremented by 5×10^{-4} and the procedure repeated until the calculated and measured values of $\delta I/I$ agreed to within 5×10^{-4} . The value of p which produced this agreement was then taken as the correct value of the optically measured target polarization p .

In order to determine an error in p , two additional computations are required. From equations (A5) and (A7) two values of the ratio $\langle \delta I / I \rangle$ were calculated

$$\langle \frac{\delta I}{I} \rangle_{\pm} = \langle \frac{\delta I}{I} \rangle \pm \Delta \langle \frac{\delta I}{I} \rangle$$

and from these the two values of polarization p_+ and p_- were computed as described in the preceding paragraph. The error Δp is then

$$\Delta p = \frac{1}{2}(p_+ - p_-).$$

3. Discussion of Optical Pumping Parameters

Colegrove et al.⁸⁾ have calculated the electric dipole transition probabilities a , b , c , assuming a 10% mixture of the 2^3P_1 wave function in the 2^3P_0 wave function. These values were used in calculating p from the optical signals. Reference 57) gives a more complete listing of these transition probabilities.

The factor f was assigned the value 0.7 in the current work. This value of f could result in a $\pm 15\%$ error in p as discussed in Section III.A. The effect of such systematic errors in the data was covered in Section III.B.2.e.

Calculations have been performed to determine the value of ρ ,⁸⁸⁾ based on data supplied by the manufacturer of the linear polarizer⁶⁹⁾ used in construction of the circular polarizer. McSherry⁸⁸⁾ reported using $\rho = 0.02 \pm 0.02$ and that this uncertainty in ρ gave errors in target polarization

no larger than those due to other sources, i.e., less than 2%. In this experiment $\rho = 0.0075$ was used.

Tables 9 and 10 summarize the constants used in calculating the target polarization p .

Table 9. Relative Electric Dipole Transition Probabilities Between Magnetic Sublevels $2^3S_1 - 2^3P_0$ in ^3He . The only Transition Probabilities shown are those for which $\Delta m = \pm 1$, representing transitions to the 2^3P_0 sublevel. (From reference 8.)

<u>Symbol</u>	<u>F</u>	<u>Magnetic Initial</u>	<u>Sublevel Final</u>	<u>Δm</u>	<u>Transition Probability</u>
a	3/2	$\pm 3/2$	$\pm 1/2$	∓ 1	0.28
b	3/2	$\pm 1/2$	$\mp 1/2$	∓ 1	0.10
c	1/2	$\pm 1/2$	$\mp 1/2$	∓ 1	0.30

Table 10. Constants Used in Computing Target Polarization from Light Absorption Signals $\langle \delta I / I \rangle$.

<u>Constant</u>	<u>Value</u>
a	0.28
b	0.10
c	0.30
f	0.70
S	6.37
W	-0.09
ρ	0.0075

APPENDIX B. EXPERIMENTAL ASYMMETRIES

1. General Information*

A nucleus with nuclear spin I can assume any one of $(2I+1)$ possible orientations with respect to some quantization axis, such as that provided by an externally supplied magnetic field. For ^3He nuclei ($I=\frac{1}{2}$) there are only two directions, parallel or antiparallel to the quantization axis. The polarization P along this axis is defined by

$$P = \frac{N_L - N_R}{N_L + N_R} \quad (\text{B1})$$

where N_L is the number of particles with spin parallel to the quantization axis and N_R is the number with spins antiparallel to the axis. The positive direction of the quantization axis, as defined by the Basel Convention⁴⁾ is

$$\hat{P} = \hat{k}_i \times \hat{k}_o \quad (\text{B2})$$

where \hat{k}_i and \hat{k}_o are unit vectors in the directions of the incident and scattered beams, respectively. Figure 15 shows relation (B2). For an unoriented beam and target experiment,

*Note. Left (L) and right (R) instead of the usual notation (up and down) is employed to be consistent with equations used later in this Appendix. The only requirement is that the quantization axis, and hence the target polarization direction, be perpendicular to the scattering plane. In this experiment the quantization axis was horizontal and perpendicular to the beam direction and the scattering plane was vertical. The two are equivalent, allowing use of the familiar left-right scattering terminology.

double scattering would be necessary in order to determine \hat{P} ; the first scattering polarizes the outgoing particles and the second scattering measures the polarization.

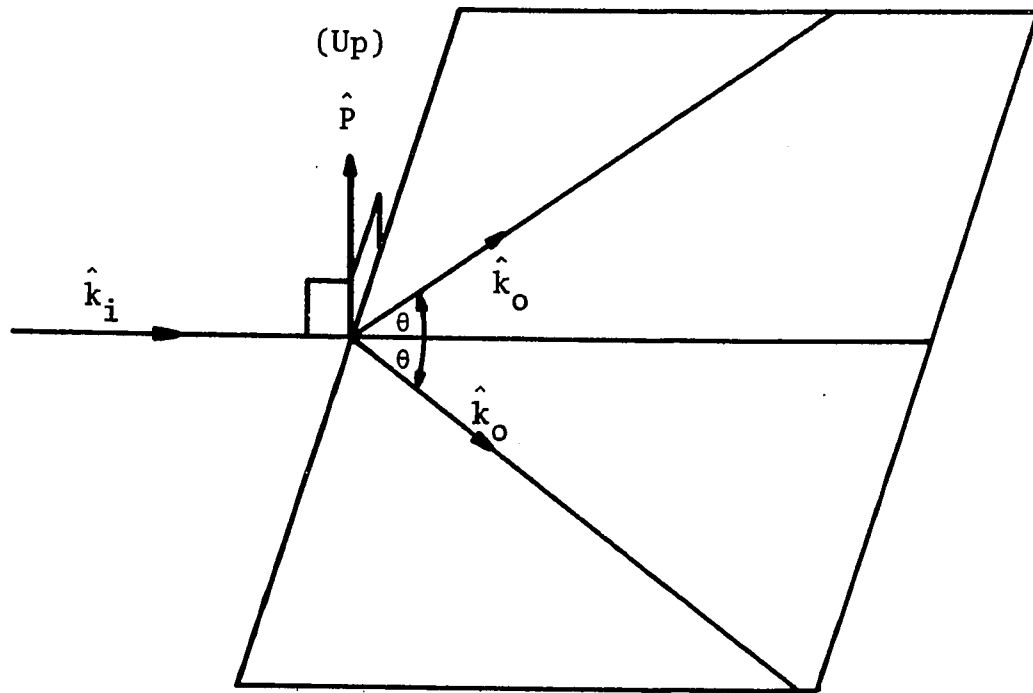
The experimental disadvantages of double scattering can be avoided by the use of a polarized beam or target to measure the cross section asymmetries, which define the reaction analyzing power A:

$$A = \frac{\sigma_L - \sigma_R}{\sigma_L + \sigma_R}. \quad (B3)$$

Here σ_L is the cross section for scattering of particles with polarization parallel to a given quantization axis and σ_R is the cross section for scattering of particles with polarization antiparallel to this axis.

Wolfenstein⁸⁹⁾ has shown that the polarizing power is equal to the analyzing power for elastic scattering if time reversal invariance holds. Comparison of equations (B1) and (B3) shows that the polarization produced in an unpolarized beam-unpolarized target experiment is equal to the cross section asymmetry or analyzing power of a polarized target-unpolarized beam experiment or a polarized beam-unpolarized target experiment.

The quantization axis of the polarized ^3He target is defined a weak external magnetic field. The up-down directions of the magnetic field are shown in Figure 15 and are consistent with the Basel Convention for \hat{P} .



- \hat{k}_i Unit vector in incident beam direction
 \hat{k}_o Unit vector in scattering direction
 \hat{P} Unit vector in target polarization direction

Figure 15. Scattering Geometry for Polarized Target Experiments.

2. Calculation of Experimental Asymmetry A

The direction of the magnetic field had a noticeable influence on the level of the optical pumping light. In order to accurately determine the reaction analyzing power, measurements were needed for all four combinations of magnetic field direction and target polarization direction. Use of all four combinations also allows one to assume that the scattering is dependent on only four different parameters which are defined in the next paragraph. Since two detectors were used, located at $\pm\theta$ on opposite sides of the beam axis, there are eight numbers or sets of counts for each energy.

The number of counts N registered by each detector is assumed to depend on four parameters, the beam integration I , the effective solid angle Ω , any unspecified magnetic field effects M (such as a shift in particle trajectories in the magnetic field), and the cross section $\sigma(\theta)$:

$$N = I\Omega M\sigma(\theta). \quad (B4)$$

Left and right scattering will occur because of the use of a polarized target. It is assumed that the left and right differential scattering cross section $\sigma_L(\theta)$ and $\sigma_R(\theta)$, respectively, for a polarized target-unpolarized beam experiment can be related to the differential cross section $\sigma(\theta)$ for an unpolarized beam-unpolarized target experiment by equation (B5).

$$\sigma(\theta) = \frac{1}{2}[\sigma_L(\theta) + \sigma_R(\theta)] \quad (B5)$$

From equations (B3) and (B5), $\sigma_L(\theta)$ and $\sigma_R(\theta)$ can be easily determined

$$\sigma_{L,R}(\theta) = \sigma(\theta)(1 \pm A) = \sigma(\theta)(1 \pm P) \quad (B6)$$

where use was made of the fact that polarizing power is equal to analyzing power in this experiment. P can be expressed in terms of the target polarization p and the reaction analyzing power P_3 for 100% target polarization,

$$P = pP_3.$$

Thus

$$\sigma_L(\theta) = \sigma(\theta)(1 + pP_3) \quad (B6a)$$

$$\sigma_R(\theta) = \sigma(\theta)(1 - pP_3) \quad (B6b)$$

and the numbers of left- and right-scattered particles are, respectively,

$$N_L = I\Omega_L M_L \sigma_L(\theta) = I\Omega_L M_L \sigma(\theta)(1 + pP_3) \quad (B4a)$$

$$N_R = I\Omega_R M_R \sigma_R(\theta) = I\Omega_R M_R \sigma(\theta)(1 - pP_3) \quad (B4b)$$

for a given combination of magnetic field direction and target polarization direction. Table 11 gives the form for all eight N 's.

In order to perform calculations using the data, $p^{(i)}$ will be expressed in terms of an average target polarization p :

Table 11. Numbers of Scattered Particles as a Function of Magnetic Field Direction \hat{M} , Target Polarization Direction \hat{P}_3 , and Scattering Angle Left or Right. The subscripts on I and the superscripts on p refer to the particular combination of \hat{M} and \hat{P}_3 . The subscripts L or R on Ω and M and the superscript L or R on P_3 refer to physical directions which remained constant throughout the experiment. The remaining subscript on M, U or D, denotes magnetic field direction. Note that N_1 , N_4 , N_5 , and N_8 correspond to left scattering (Basel Convention), but that only N_1 and N_5 represent left scattering into the detector located on the physical left of the apparatus. See Figure 15.

	<u>Scattering Angle</u>	<u>\hat{M}</u>	<u>\hat{P}_3</u>
$N_1 = I_1 \Omega_L^M \sigma(\theta) (1 + p^{(1)} P_3^L)$	Left	Up	Up
$N_2 = I_1 \Omega_R^M \sigma(\theta) (1 - p^{(1)} P_3^R)$	Right		
$N_3 = I_2 \Omega_L^M \sigma(\theta) (1 - p^{(2)} P_3^L)$	Left	Up	Down
$N_4 = I_2 \Omega_R^M \sigma(\theta) (1 + p^{(2)} P_3^R)$	Right		
$N_5 = I_3 \Omega_L^M \sigma(\theta) (1 + p^{(3)} P_3^L)$	Left	Down	Up
$N_6 = I_3 \Omega_R^M \sigma(\theta) (1 - p^{(3)} P_3^R)$	Right		
$N_7 = I_4 \Omega_L^M \sigma(\theta) (1 - p^{(4)} P_3^L)$	Left	Down	Down
$N_8 = I_4 \Omega_R^M \sigma(\theta) (1 + p^{(4)} P_3^R)$	Right		

$$p^{(i)} = p(1 + \alpha_i), \quad \sum_{i=1}^4 \alpha_i = 0 \quad (B7)$$

where i runs over the four counting periods previously described. The constants α_i arise from the fact that the optical pumping light level is dependent on the magnetic field direction. The left and right analyzing powers, P_3^L and P_3^R , respectively, can be written in terms of the analyzing power P_3 for 100% target polarization.

$$P_3^L = P_3(1 + \beta) \quad (B8a)$$

$$P_3^R = P_3(1 - \beta) \quad (B8b)$$

The constant β allows for such geometrical effects as differences in mean scattering angle for the two detectors. In equations (B7) and (B8) α_i and β are usually small.

The ratio R of left- to right-scattered events can now be formed using equations (B7) and (B8) and Table 11,

$$R = \frac{N_1 N_4 N_5 N_8}{N_2 N_3 N_6 N_7} = \left(\frac{1 + pP_3}{1 - pP_3} \right)^4 [1 + f(\alpha_i, \beta, pP_3)] \quad (B9)$$

where $f(\alpha_i, \beta, pP_3)$ contains second and higher order terms in α_i, β, pP_3 . Neglecting such terms, equation (B9) yields the reaction analyzing power.

$$P_3 = \frac{A}{P} = \frac{1}{P} \left(\frac{R^{\frac{1}{4}} - 1}{R^{\frac{1}{4}} + 1} \right) \quad (B10)$$

It should be noted that any effects due to beam integration I ,

effective solid angle Ω , and magnetic field M have been cancelled out.

The statistical error ΔA in the experimental asymmetry $A = pP_3$ was computed from equation (B11) assuming no background correction.

$$\Delta A = \Delta(pP_3) = \frac{\partial A}{\partial R} \Delta R = \frac{R^{\frac{1}{4}} \Delta R}{2R(R^{\frac{1}{4}} + 1)^2} = \frac{R^{\frac{1}{4}}}{2(R^{\frac{1}{4}} + 1)^2} \left[\sum_{i=1}^8 \frac{1}{N_i} \right]^{\frac{1}{2}} \quad (\text{B11})$$

Here ΔR is defined by equation (B13). The error in P_3 , excluding any systematic error discussed in Section III.A., is

$$\Delta P_3 = \frac{1}{p} [(\Delta A)^2 + P_3^2 (\Delta p)^2]^{\frac{1}{2}}.$$

3. Instrumental Asymmetry A_0

A measure of the departure of the experimental apparatus from complete symmetry is found by forming the ratio R_0 such that all terms--beam integration, solid angle, magnetic field effects, and polarization--cancel.

$$R_0 = \frac{N_1 N_4 N_6 N_7}{N_2 N_3 N_5 N_8}$$

This should give R_0 the value unity in an ideal case if the correct dependence on the scattering parameters has been assumed and the data are consistent. Thus the variation of the instrumental asymmetry from zero should give an estimate of any systematic errors in the data and hence its quality.

$$A_0 = \frac{R_0^{\frac{1}{4}} - 1}{R_0^{\frac{1}{4}} + 1}$$

Two other types of asymmetry can be computed for experiments such as this. These are the magnetic field asymmetry A_M and the modified solid angle asymmetry $A_{\Omega M}$. Their definition is included here for completeness only. In practice the experimental asymmetry A and the instrumental asymmetry A_0 are the ones usually given.

4. Magnetic Field Asymmetry A_M

The magnetic field asymmetry A_M is an indication of the scattering asymmetry due to any magnetic field effect. It is necessary to assume that such an effect is reversed when the direction of the magnetic field is reversed, i.e., it depends on the magnetic field direction:

$$\frac{M_{LU}}{M_{LD}} = \frac{M_{RD}}{M_{RU}} \quad (B12)$$

The ratio R_M is formed such that all effects except those due to the magnetic field cancel.

$$R_M = \frac{N_1 N_3 N_6 N_8}{N_2 N_4 N_5 N_7} = \left(\frac{M_{LU}}{M_{LD}} \frac{M_{RD}}{M_{RU}} \right)^2 = \left(\frac{M_{LU}}{M_{LD}} \right)^4 = \left(\frac{M_{RD}}{M_{RU}} \right)^4$$

The magnetic field asymmetry is then

$$A_M = \frac{M_{LU} - M_{LD}}{M_{LU} + M_{LD}} = \frac{M_{RD} - M_{RU}}{M_{RD} + M_{RU}} = \frac{R_M^{\frac{1}{4}} - 1}{R_M^{\frac{1}{4}} + 1}.$$

5. Modified Solid Angle Asymmetry $A_{\Omega M}$

The solid angle asymmetry arises from differences in solid angle seen by the two detectors or from differences in detector efficiency. In this experiment it is not possible to compute a solid angle asymmetry from the information available. It is, however, possible to compute an asymmetry which indicates the combined effect of solid angle and magnetic field on the relative scattering, which will be denoted by $A_{\Omega M}$.

The ratio $R_{\Omega M}$ of the left-to-right solid angles is formed.

$$R_{\Omega M} = \frac{N_1 N_3 N_5 N_7}{N_2 N_4 N_6 N_8} = \left(\frac{\Omega_L}{\Omega_R}\right)^4 \left(\frac{M_{LU}}{M_{RU}}\right)^2 \left(\frac{M_{LD}}{M_{RD}}\right)^2$$

By using equation (B12), $R_{\Omega M}$ can be put in the form

$$R_{\Omega M} = \left(\frac{\Omega_L}{\Omega_R} \frac{M_{LD}}{M_{RU}}\right)^4 = \left(\frac{\Omega_L}{\Omega_R} \frac{M_{LU}}{M_{RD}}\right)^4$$

which has the same value for either magnetic field direction U or D. For simplicity a slight change in notation is made by deleting the reference to the magnetic field direction. Thus

$$R_{\Omega M} = \left(\frac{\Omega_L M_L}{\Omega_R M_R} \right)^4$$

and from this the modified angle asymmetry is computed.

$$A_{\Omega M} = \frac{\Omega_L M_L - \Omega_R M_R}{\Omega_L M_L + \Omega_R M_R} = \frac{R_{\Omega M}^{\frac{1}{4}} - 1}{R_{\Omega M}^{\frac{1}{4}} + 1}$$

6. Weighted Average and Weighted Average Error

For Duplicate Measurements

When several measurements of an asymmetry a were made at a given energy a weighted average of these values is computed and reported as the asymmetry at that energy. This average weighs most heavily those measurements with the smallest errors and vice versa. The weighted average $\langle a \rangle$ for n measurements of a is

$$\langle a \rangle = \frac{\sum_{i=1}^n w_i a_i}{\sum_{i=1}^n w_i} = \frac{\sum_{i=1}^n \frac{a_i}{(\Delta a_i)^2}}{\sum_{j=1}^n (\Delta a_j)^{-2}}$$

where the weighting factor w_i is

$$w_i = \frac{(\Delta a_i)^{-2}}{\sum_{j=1}^n (\Delta a_j)^{-2}}$$

From the error Δa_i the average error $\langle \Delta a \rangle$ is given by

$$\langle \Delta a \rangle = \left[\sum_{i=1}^n (\Delta a_i)^{-2} \right]^{-\frac{1}{2}}.$$

7. Background Correction

When the background is level in a spectrum, the accuracy of the background level is determined by the number of counts on either side of the peak under consideration. In Figure 16 the measured quantities F_B , F_A , and $N + F_N$ are shown. The accuracy of $F_B + F_A$ determines the accuracy of the level of F_N , and to the uncertainty in $(F_B + F_A)$ must be added the statistical uncertainty in F_N , namely $F_N^{\frac{1}{2}}$. Denote the total uncertainty in F_N by ΔF_N . Then

$$\left(\frac{\Delta F_N}{F_N} \right)^2 = \left(\frac{(F_B + F_A)^{\frac{1}{2}}}{F_B + F_A} \right)^2 + \left(\frac{F_N^{\frac{1}{2}}}{F_N} \right)^2 = \frac{1 + \gamma}{\gamma F_N}$$

where

$$\gamma = \frac{F_B + F_A}{F_N} = \frac{\text{background counts determining background level}}{\text{background under peak}}$$

In the same manner, the total uncertainty in N is given by

$$\left(\frac{\Delta N}{N} \right)^2 = \frac{1}{N^2} [(F_N + N)^{\frac{1}{2}}]^2 + (\Delta F_N)^2 = \frac{1}{N} \left[1 + \rho \left(\frac{1+2\gamma}{\gamma} \right) \right]$$

where

$$\rho = \frac{F_N}{N} = \frac{\text{background under peak}}{\text{true counts under peak}}$$

Summing over all peaks in a data set gives the statistical uncertainty in the ratio R , equation (B9).

$$\left(\frac{\Delta R}{R}\right) = \left(\sum_{i=1}^8 \frac{1}{N_i} \left[1 + \frac{\rho_i}{\gamma_i} (1+2\gamma_i)\right]\right)^{\frac{1}{2}}$$

When there is no background, $\rho_i = 0$ and $\gamma_i = \infty$, giving the result

$$\left(\frac{\Delta R}{R}\right) = \left(\sum_{i=1}^8 \frac{1}{N_i}\right)^{\frac{1}{2}} \quad (\text{B13})$$

which was used in equation (B11).

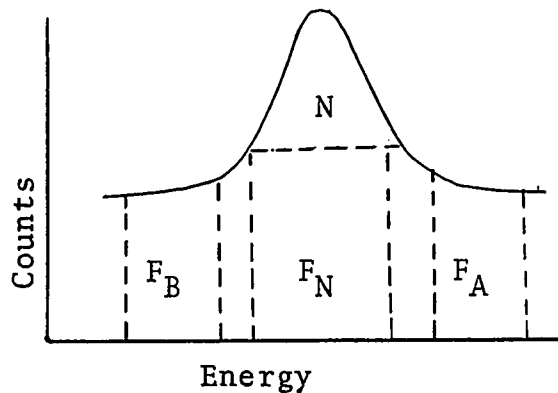


Figure 16. Spectrum With Level Background

F_B = background counts below peak

F_N = background counts under peak

F_A = background counts above peak

N = true counts under peak

APPENDIX C. PHASE SHIFT ANALYSIS: ELASTIC SCATTERING OF CHARGED SPIN $\frac{1}{2}$ PARTICLES FROM SPIN 0 PARTICLES

1. Differential Cross Section Equations*

The total wave function ψ for the elastic scattering of uncharged spinless particles is well known

$$\psi = \psi_{\text{in}} + \psi_{\text{out}} = \frac{i}{\sqrt{v}} [e^{ikz} + \frac{e^{ikr}}{r} A(\theta)]$$

where the first term in the brackets represents an incoming plane wave and the second term an outgoing spherical wave with angular dependence $A(\theta)$. The differential cross section for this case is $|A(\theta)|^2$.

For the case of charged particles with spin, the formula will be quite similar except that the incident and scattered waves will be distorted by the Coulomb field and the wave function will contain the internal spin coordinates of the separate particles.

Consider now the case of two particles in a spherically symmetric potential. The Schroedinger equation is separable and the wave function of the relative motion of the two particles is

*This derivation of expressions for the differential cross section follows closely those given by Lane and Thomas⁸²⁾ and Rich.⁹⁰⁾ Rich's development is based in part on that of Lane and Thomas.

$$\psi \sim r_{\alpha}^{-1} U_{\alpha s \ell}(r_{\alpha}) i^{\ell} Y_{\ell}^m(\Omega_{\alpha}).$$

In this equation α denotes the pair of particles 1 and 2 and

- r_{α} = radial coordinate from particle 1 to particle 2
- $U_{\alpha s \ell}(r_{\alpha})$ = solution to the radial equation of relative motion of the pair α
- ℓ = relative angular momentum of the pair (with z component m)
- s = channel spin of the pair (with z component ν)
- $Y_{\ell}^m(\Omega_{\alpha})$ = normalized spherical harmonics
- Ω_{α} = direction from particle 1 to particle 2.

The radial equation is

$$\left[\frac{d^2}{dr_{\alpha}^2} - \frac{\ell(\ell+1)}{r_{\alpha}^2} - \frac{2M_{\alpha}}{\hbar^2} (V_{\alpha s \ell} - E_{\alpha}) \right] U_{\alpha s \ell}(r_{\alpha}) = 0$$

which can easily be put in the dimensionless form

$$\left[\frac{d^2}{d\rho_{\alpha}^2} - \frac{\ell(\ell+1)}{\rho_{\alpha}^2} + \frac{2\eta_{\alpha}}{\rho_{\alpha}} - 1 \right] U_{\alpha s \ell}(\rho_{\alpha}) = 0 \quad (C1)$$

by using the following:

$$\rho_{\alpha} = k_{\alpha} r_{\alpha} = \text{dimensionless independent variable}$$

$$M_{\alpha} = \frac{M_1 M_2}{M_1 + M_2} = \text{reduced mass}$$

$$v_{\alpha} = \frac{\hbar k_{\alpha}}{M_{\alpha}} = \text{relative velocity of the two particles}$$

$$E_{\alpha} = \frac{1}{2} M_{\alpha} v_{\alpha}^2 = \text{energy of relative motion, } E_{\alpha} > 0 \\ \text{is assumed in this analysis}$$

$$k_{\alpha} = \left(\frac{2M_{\alpha} E_{\alpha}}{\hbar^2} \right)^{1/2} = \text{wave number}$$

$$\eta_{\alpha} = \frac{z_1 z_2 e^2}{\hbar v_{\alpha}} = \text{Coulomb field parameter.}$$

In the asymptotic region of large ρ_{α} there are two linearly independent solutions to equation (C1) representing incoming (I) and outgoing (O) waves:

$$\begin{aligned} I_{\alpha\ell} &\sim \exp[-i(\rho_{\alpha} - \eta_{\alpha} \log 2\rho_{\alpha} - \frac{1}{2}\ell\pi + \sigma_{\alpha 0})] \\ O_{\alpha\ell} &\sim \exp[i(\rho_{\alpha} - \eta_{\alpha} \log 2\rho_{\alpha} - \frac{1}{2}\ell\pi + \sigma_{\alpha 0})]. \end{aligned} \quad (C2)$$

For applications a more convenient form of equation (C2) is useful, those regular ($F_{\alpha\ell}$) and irregular ($G_{\alpha\ell}$) at the origin.

$$\begin{aligned} F_{\alpha\ell} &\sim \sin(\rho_{\alpha} - \eta_{\alpha} \log 2\rho_{\alpha} - \frac{1}{2}\ell\pi + \sigma_{\alpha\ell}) \\ G_{\alpha\ell} &\sim \cos(\rho_{\alpha} - \eta_{\alpha} \log 2\rho_{\alpha} - \frac{1}{2}\ell\pi + \sigma_{\alpha\ell}) \end{aligned} \quad (C3)$$

The relation between equations (C2) and (C3) is

$$\begin{aligned} I_{\alpha\ell} &= (G_{\alpha\ell} - iF_{\alpha\ell})\exp(i\omega_{\alpha\ell}) \\ O_{\alpha\ell} &= (G_{\alpha\ell} + iF_{\alpha\ell})\exp(-i\omega_{\alpha\ell}) \end{aligned} \quad (C4)$$

where

$$\omega_{\alpha\ell} = \sigma_{\alpha\ell} - \sigma_{\alpha 0} = \sum_{n=1}^{\ell} \tan^{-1}\left(\frac{\eta_{\alpha}}{n}\right)$$

$\sigma_{\alpha\ell}$ = Coulomb phase shift corresponding to
relative angular momentum ℓ with
 $\omega_{\alpha 0} = 0$.

The complete channel wave functions for $E_{\alpha} > 0$ for the incoming and outgoing waves of unit flux crossing any sphere centered at the origin in the $(\alpha s \ell v m)$ channel scheme are⁸²⁾

$$\begin{aligned} I_{\alpha s \ell v m} &= i^{\ell} Y_{\ell}^m \frac{I_{\alpha \ell}}{r_{\alpha} \sqrt{v_{\alpha}}} \psi_{\alpha s v} \\ O_{\alpha s \ell v m} &= i^{\ell} Y_{\ell}^m \frac{O_{\alpha \ell}}{r_{\alpha} \sqrt{v_{\alpha}}} \psi_{\alpha s v} \end{aligned} \quad (C5)$$

where

$$\psi_{\alpha s v} = \phi_{\alpha s} \chi_s^v = \sum_{v=i_1+i_2} (I_1 I_2 i_1 i_2 | s v) \psi_{\alpha_1 I_1 i_1} \psi_{\alpha_2 I_2 i_2}$$

= channel wave function composed of products of
wave functions of internal states of particles
1 and 2

$\phi_{\alpha s}$ = product of wave function of separate particles

χ_s^v = product of spin functions of separate particles.

The general solution ψ in the asymptotic region can be expressed as a linear combination of the linearly independent $I_{\alpha s \ell v m}$ and $O_{\alpha s \ell v m}$ waves.⁸²⁾

$$\Psi = \sum_c B_c [I_c - \sum_{c'} U_{cc'} O_{c'}] \quad (C6)$$

Here c stands for $\alpha s \ell v m$, c' for $\alpha' s' \ell' v' m'$, and $U_{cc'}$, the collision or scattering function, is the amplitude of the unit flux outgoing wave $O_{c'}$, which is associated with the unit flux incident wave I_c . The B_c are at this point unspecified coefficients of the incoming waves. Now add to and subtract from (C6) the function ψ' which is proportional to the regular function $F_{\alpha \ell}$

$$\psi' = \sum_{cc'} B_c [I_c - O_c \exp(2i\omega_c)] \delta_{cc'} \quad (C7)$$

which gives the general solution Ψ :

$$\Psi = \psi' + \sum_{cc'} B_c [\delta_{cc'} \exp(2i\omega_c) - U_{cc'}] O_{c'}. \quad (C8)$$

This eliminates any explicit reference to the incoming waves. By choosing the coefficients B_c properly ψ' will represent an incident plane wave of particles of only type α with channel spin s and z -component v and disturbed by only the Coulomb field. The correct form is ⁸²⁾

$$B_c \equiv B_{\alpha s \ell v 0} = \frac{i\sqrt{\pi}}{k_\alpha} (2\ell+1)^{\frac{1}{2}} \quad (C9)$$

with all others being zero.

Consider now the first term in equation (C8), namely ψ' , equation (C7). By using equations (C4), (C5), (C9),

and the fact that $Y_\ell^0 = \left(\frac{2\ell+1}{4\pi}\right)^{1/2} P_\ell(\cos\theta)$, a single term $\psi'_{\alpha s v}$ (corresponding to a pair α) in equation (C7) can be written

$$\psi'_{\alpha s v} = \frac{1}{k_\alpha \sqrt{v_\alpha}} \sum_\ell i^\ell (2\ell+1) \exp(i\omega_{\alpha\ell}) \left(\frac{F_{\alpha\ell}}{r_\alpha}\right) P_\ell(\cos\theta_\alpha) \psi_{\alpha s v}. \quad (C7a)$$

Schiff⁹¹⁾ gives a form of equation (C7a) which will be more useful for our purposes:

$$\begin{aligned} \psi'_{\alpha s v} \sim \frac{1}{\sqrt{v_\alpha}} \{ [1 - \frac{\eta_\alpha^2}{ik_\alpha(r_\alpha - z_\alpha)}] \exp[i(k_\alpha z_\alpha - \eta_\alpha \log k_\alpha(r_\alpha - z_\alpha) - \sigma_{\alpha 0})] \\ + \frac{i\sqrt{\pi}}{r_\alpha k_\alpha} f(\theta_\alpha) \exp[i(\rho_\alpha - \eta_\alpha \log 2\rho_\alpha + \sigma_{\alpha 0})] \} \psi_{\alpha s v} \end{aligned} \quad (C7b)$$

where

$$f(\theta_\alpha) = \frac{i\eta_\alpha}{2\sqrt{\pi}} \csc^2(\frac{1}{2}\theta_\alpha) \exp[i\eta_\alpha \log \csc^2(\frac{1}{2}\theta_\alpha)]. \quad (C7c)$$

Note that the second term in equation (C7b) is of the form $\rho^{-1} \exp(i\rho)$ and is thus an outgoing spherical wave. Later use will be made of this fact.

We return now to the second term in equation (C8), a single term of which will be denoted by $\psi''_{\alpha s v}$. By employing equations (C2), (C5), (C8), (C9), and noting that $i^\ell \exp(-i\ell\frac{1}{2}\pi) = 1$ we may write

$$\begin{aligned} \psi''_{\alpha s v} = \frac{i\sqrt{\pi}}{k_\alpha} \sum_{\ell \ell' \alpha' s' v' m'} \frac{(2\ell+1)^{1/2}}{r_{\alpha'} \sqrt{v_{\alpha'}}} \exp[i(\rho_{\alpha'} - \eta_{\alpha'} \log 2\rho_{\alpha'} + \sigma_{\alpha' 0})] \\ \times [\exp(2i\omega_{\alpha' \ell'}) \delta_{\alpha s \ell v 0}^{\alpha' s' \ell' v' m'} - U_{\alpha s \ell v 0}^{\alpha' s' \ell' v' m'}] Y_{\ell'}^{m'} \psi_{\alpha' s' v' m'}. \end{aligned} \quad (C8a)$$

Equation (C8a) can be changed from the $(\alpha s l v m)$ scheme to the $(\alpha s l J M)$ scheme by substituting ⁸²⁾

$$U_{\alpha s l v}^{\alpha' s' l' v' m'} = \sum_{J M} (s l v 0 | J M) U_{\alpha s l}^{\alpha' s' l'} (s' l' v' m' | J M).$$

Thus

$$\begin{aligned} \psi_{\alpha s v}'' &= \frac{i\sqrt{\pi}}{k_{\alpha}} \sum_{\substack{\alpha' l l' \\ s' J M m'}} \frac{(2l+1)^{\frac{1}{2}}}{r_{\alpha'} \sqrt{v_{\alpha'}}} (s l v 0 | J M) (s' l' v' m' | J M) Y_{\ell}^{m'} \\ &\times \exp[i(\rho_{\alpha}, -\eta_{\alpha}, \log 2\rho_{\alpha}, +\sigma_{\alpha, 0})] \\ &\times [\exp(2i\omega_{\alpha, \ell'}) \delta_{\alpha s l}^{\alpha' s' l'} - U_{\alpha s l}^{\alpha' s' l'}] \psi_{\alpha' s' v'}. \end{aligned} \quad (C8b)$$

Note that equation (C8b) is outgoing. Now we consider only the outgoing part of equation (C8), i.e., equation (C8b) and the second term in equation (C7b), the part containing $f(\theta_{\alpha})$.

$$\begin{aligned} \psi_{\alpha s v}^{\text{out}} &= \psi_{\alpha s v}^{\text{out}} + \psi_{\alpha s v}''^{\text{out}} \\ &= \frac{i\sqrt{\pi}}{k_{\alpha} \sqrt{v_{\alpha}}} \frac{f(\theta_{\alpha})}{r_{\alpha}} \exp[i(\rho_{\alpha}, -\eta_{\alpha}, \log 2\rho_{\alpha}, +\sigma_{\alpha, 0})] \psi_{\alpha s v} \\ &+ \frac{i\sqrt{\pi}}{k_{\alpha}} \sum_{\substack{\alpha' l l' \\ s' J M m'}} \frac{(2l+1)^{\frac{1}{2}}}{r_{\alpha'} \sqrt{v_{\alpha'}}} (s l v 0 | J M) (s' l' v' m' | J M) Y_{\ell}^{m'} \psi_{\alpha' s' l'} \\ &\times \exp[i(\rho_{\alpha}, -\eta_{\alpha}, \log 2\rho_{\alpha}, +\sigma_{\alpha, 0})] \\ &\times [\exp(2i\omega_{\alpha, \ell'}) \delta_{\alpha s l}^{\alpha' s' l'} - U_{\alpha s l}^{\alpha' s' l'}] \} \end{aligned}$$

$$\begin{aligned}
\Psi_{\alpha s v \text{ out}} &= \frac{i\sqrt{\pi}}{k_{\alpha}} \sum_{\substack{\alpha' \ell \ell' \\ s' J M m'}} \frac{1}{r_{\alpha'} \sqrt{v_{\alpha'}}} \exp[i(\rho_{\alpha'} - \eta_{\alpha'}, \log 2\rho_{\alpha'} + \sigma_{\alpha', 0})] \\
&\times f(\theta_{\alpha'}) \delta_{\alpha s v \alpha' s' v'} + (2\ell+1)^{\frac{1}{2}} (s \ell v 0 | J M) (s' \ell' v' m' | J M) Y_{\ell'}^{m'} \\
&\times [\exp(2i\omega_{\alpha' \ell'}) \delta_{\alpha s \ell \alpha' s' \ell'} - U_{\alpha s \ell \alpha' s' \ell'}^J] \chi_{v' \alpha' s' \ell'}^{s'} \phi_{\alpha' s'}
\end{aligned}$$

Now let

$$\Psi_{\alpha s v \text{ out}} = \sum_{\alpha' s'} R(r_{\alpha'}) A_{\alpha s v \alpha' s' v'}(\Omega_{\alpha'}) \phi_{\alpha' s'}$$

where

$$R(r_{\alpha'}) = \frac{1}{r_{\alpha'} \sqrt{v_{\alpha'}}} \exp[i(\rho_{\alpha'} - \eta_{\alpha'}, \log 2\rho_{\alpha'} + \sigma_{\alpha', 0})].$$

By using the orthonormality of the $\phi_{\alpha' s'}$,

$$\int \phi_{\alpha'' s''} \phi_{\alpha' s'} dq_{\alpha''} = \delta_{\alpha'' s'', \alpha' s'},$$

$A_{\alpha s v \alpha' s' v'}$ may be written

$$\begin{aligned}
A_{\alpha s v \alpha' s' v'}(\Omega_{\alpha'}) &= \frac{i\sqrt{\pi}}{k_{\alpha}} \sum_{\substack{\ell \ell' \\ J M m'}} f(\theta_{\alpha'}) \delta_{\alpha s v \alpha' s' v'} \\
&+ (2\ell+1)^{\frac{1}{2}} (s \ell v 0 | J M) (s' \ell' v' m' | J M) Y_{\ell'}^{m'} \\
&\times [\exp(2i\omega_{\alpha' \ell'}) \delta_{\alpha s \ell \alpha' s' \ell'} - U_{\alpha s \ell \alpha' s' \ell'}^J] \chi_{v' \alpha' s' \ell'}^{s'}.
\end{aligned}$$

Next $f(\theta_{\alpha'})$ is replaced by its value, equation (C7c), and removed from inside the brackets since it is not summed over.

$$\begin{aligned}
A_{\alpha s v \alpha' s' v'}(\Omega_{\alpha'}) &= -\frac{\eta}{2k_{\alpha}} \csc^2(\tfrac{1}{2}\theta_{\alpha}) \exp[i\eta_{\alpha} \log \csc^2(\tfrac{1}{2}\theta_{\alpha})] \chi_v^s \\
&+ \frac{i/\pi}{k_{\alpha}} \sum_{\ell \ell' JM m'} (2\ell+1)^{\frac{1}{2}} (s \ell v 0 | JM) (s' \ell' v' m' | JM) Y_{\ell}^{m'} \\
&\times [\exp(2i\omega_{\alpha' \ell'}) \delta_{\alpha s \ell \alpha' s' \ell'} - U_{\alpha s \ell \alpha' s' \ell'}^J] \chi_{v'}^{s'}
\end{aligned}$$

The differential cross section is then given by

$$\sigma_{\alpha s v \alpha' s' v'} = |A_{\alpha s v \alpha' s' v'}(\Omega_{\alpha'})|^2.$$

The differential cross section for the $\alpha s \rightarrow \alpha' s'$ collision in which the beam is unpolarized and the final spin directions are not separately observed is obtained by averaging over the incident spin directions v and summing over the final spin directions v' .

$$\sigma_{\alpha s, \alpha' s'} = \left(\frac{1}{2s+1}\right) \sum_{vv'} \sigma_{\alpha s v \alpha' s' v'}$$

The differential cross section for the $\alpha \rightarrow \alpha'$ collision, without regard to channel spin s or s' , is found by averaging over the possible values of s and summing over the possible values of s'

$$\sigma_{\alpha, \alpha'} = \sum_{s, s'} \frac{2s+1}{(2I_1+1)(2I_2+1)} \sigma_{\alpha s, \alpha' s'} \quad (C10)$$

where I_1 and I_2 are the spins of the two interacting particles and the numerical factor in equation (C10) is the statistical weight of the channel spin s . Thus

$$\begin{aligned}
\sigma_{\alpha, \alpha'} &= \frac{1}{(2I_1+1)(2I_2+1)} \sum_{s s'} \sum_{v v'} \sigma_{\alpha s v} \sigma_{\alpha' s' v'} \\
&= \frac{1}{(2I_1+1)(2I_2+1)} \sum_{s v} \left| \sum_{s' v'} A_{\alpha s v} A_{\alpha' s' v'} (\Omega_{\alpha'}) \right|^2 \quad (C11)
\end{aligned}$$

where the sum over $s'v'$ was taken inside the absolute value brackets because these subscripts are on the amplitude factor $A(\Omega_{\alpha'})$.

Now to specialize these results to the case of elastic scattering ($\alpha = \alpha'$) of a spin $\frac{1}{2}$ particle from a spin 0 particle. Conservation of momentum and parity require that $\ell = \ell'$ and $s = s' = \frac{1}{2}$. Also the sums over s and s' reduce to a single term. Equation (C11) then becomes

$$\sigma_{\alpha, \alpha} = \frac{1}{2} \sum_v \left| \sum_{v'} A_{\alpha s v} A_{\alpha s v'} (\Omega_{\alpha'}) \right|^2. \quad (C12)$$

Let

$$\begin{aligned}
f_s^v &= \sum_{v'} A_{\alpha s v} A_{\alpha s v'} = -\frac{\eta_{\alpha}}{2k_{\alpha}} \csc^2(\frac{1}{2}\theta_{\alpha}) \exp[i\eta_{\alpha} \log \csc^2(\frac{1}{2}\theta_{\alpha})] \chi_s^v \\
&\quad + \frac{i\sqrt{\pi}}{k_{\alpha}} \sum_{\ell m'} (2\ell+1)^{\frac{1}{2}} (s \ell v 0 | JM) (s' \ell v' m' | JM) Y_{\ell}^{m'} \\
&\quad \times [\exp(2i\omega_{\ell}) - U_{s\ell}^J] \chi_{s'}^{v'}. \quad (C13)
\end{aligned}$$

By noting that $m' = v - v'$, $M = v$, and $s = \frac{1}{2}$, equation (C13) becomes

$$\begin{aligned}
f_{\frac{1}{2}}^v &= \frac{-\eta}{2k} \csc^2(\frac{1}{2}\theta) \exp[i\eta \log \csc^2(\frac{1}{2}\theta)] \chi_{\frac{1}{2}}^v \\
&+ \frac{i\sqrt{\pi}}{k} \sum_{\substack{J \\ v'}} (2\ell+1)^{\frac{1}{2}} (\frac{1}{2}\ell v 0 | Jv) (\frac{1}{2}\ell v', v-v' | Jv) Y_{\ell}^{v-v'} \\
&\times [\exp(2i\omega_{\ell}) - U_{\frac{1}{2}, \ell}^J] \chi_{\frac{1}{2}}^{v'} \quad (C14)
\end{aligned}$$

where unnecessary subscripts have been eliminated. In equation (C14) the first term on the right is known as the Rutherford contribution to the scattering amplitude and the second term is the nuclear contribution. We note that $J = \ell \pm \frac{1}{2}$ so there will be two terms in (C14) due to the sum over J . Also the sum over v' gives two terms for each value of J . By carrying out explicitly the sums over J and v' , multiplying by $2k$ and using the vector addition coefficients in Table 12, equation (C14) for $v = \frac{1}{2}$ becomes

$$\begin{aligned}
2kf_{\frac{1}{2}}^{\frac{1}{2}} &= \{-\eta \csc^2(\frac{1}{2}\theta) \exp[i\eta \log \csc^2(\frac{1}{2}\theta)] \\
&+ 2i\sqrt{\pi} \sum_{\ell} (2\ell+1)^{\frac{1}{2}} Y_{\ell}^0 \{ (\frac{\ell+1}{2\ell+1}) [\exp(2i\omega_{\ell}) - U_{\frac{1}{2}, \ell}^{\ell+\frac{1}{2}}] \\
&+ (\frac{\ell}{2\ell+1}) [\exp(2i\omega_{\ell}) - U_{\frac{1}{2}, \ell}^{\ell-\frac{1}{2}}] \} \} \chi_{\frac{1}{2}}^{\frac{1}{2}} \\
&+ [2i\sqrt{\pi} \sum_{\ell} (\frac{\ell(\ell+1)}{2\ell+1})^{\frac{1}{2}} Y_{\ell}^1 (U_{\frac{1}{2}, \ell}^{\ell-\frac{1}{2}} - U_{\frac{1}{2}, \ell}^{\ell+\frac{1}{2}})] \chi_{\frac{1}{2}}^{-\frac{1}{2}}. \quad (C15)
\end{aligned}$$

If we let the coefficient of $\chi_{\frac{1}{2}}^{\frac{1}{2}}$ be f_c and that of $\chi_{\frac{1}{2}}^{-\frac{1}{2}}$ be f_i , equation (C15) is

$$2kf_{\frac{1}{2}}^{\frac{1}{2}} = f_c \chi_{\frac{1}{2}}^{\frac{1}{2}} + f_i \chi_{\frac{1}{2}}^{-\frac{1}{2}}. \quad (C15a)$$

Table 12. Vector addition coefficients for Spin $\frac{1}{2}$ + Spin 0.

(From reference 92).

$$(\frac{1}{2}, \ell, \frac{1}{2}, 0 \mid \ell + \frac{1}{2}, \frac{1}{2}) = (\frac{\ell+1}{2\ell+1})^{\frac{1}{2}} \quad (\frac{1}{2}, \ell, \frac{1}{2}, 0 \mid \ell - \frac{1}{2}, \frac{1}{2}) = -(\frac{\ell}{2\ell+1})^{\frac{1}{2}}$$

$$(\frac{1}{2}, \ell, -\frac{1}{2}, 1 \mid \ell + \frac{1}{2}, \frac{1}{2}) = (\frac{\ell}{2\ell+1})^{\frac{1}{2}} \quad (\frac{1}{2}, \ell, -\frac{1}{2}, 1 \mid \ell - \frac{1}{2}, \frac{1}{2}) = (\frac{\ell+1}{2\ell+1})^{\frac{1}{2}}$$

$$(\frac{1}{2}, \ell, -\frac{1}{2}, 0 \mid \ell + \frac{1}{2}, -\frac{1}{2}) = (\frac{\ell+1}{2\ell+1})^{\frac{1}{2}} \quad (\frac{1}{2}, \ell, -\frac{1}{2}, 0 \mid \ell - \frac{1}{2}, -\frac{1}{2}) = (\frac{\ell}{2\ell+1})^{\frac{1}{2}}$$

$$(\frac{1}{2}, \ell, \frac{1}{2}, -1 \mid \ell + \frac{1}{2}, -\frac{1}{2}) = (\frac{\ell}{2\ell+1})^{\frac{1}{2}} \quad (\frac{1}{2}, \ell, \frac{1}{2}, -1 \mid \ell - \frac{1}{2}, -\frac{1}{2}) = -(\frac{\ell+1}{2\ell+1})^{\frac{1}{2}}$$

The factor f_c is the so-called coherent scattering amplitude and represents particles in which no spin change has occurred while f_i is the incoherent scattering amplitude and represents particles that have had a spin change. In the same manner $f_{\frac{1}{2}}^{-\frac{1}{2}}$ is

$$\begin{aligned}
 2kf_{\frac{1}{2}}^{-\frac{1}{2}} = & \left[-\eta \csc^2(\tfrac{1}{2}\theta) \exp[i\eta \log \csc^2(\tfrac{1}{2}\theta)] \right. \\
 & + 2i\sqrt{\pi} \sum_{\ell} (2\ell+1)^{\frac{1}{2}} Y_{\ell}^0 \left\{ \frac{\ell+1}{2\ell+1} [\exp(2i\omega_{\ell}) - U_{\frac{1}{2},\ell}^{\ell+\frac{1}{2}}] \right. \\
 & + \left. \left(\frac{\ell}{2\ell+1} \right) [\exp(2i\omega_{\ell}) - U_{\frac{1}{2},\ell}^{\ell-\frac{1}{2}}] \right\} \chi_{\frac{1}{2}}^{-\frac{1}{2}} \\
 & + \left. \left[2i\sqrt{\pi} \sum_{\ell} \left(\frac{\ell(\ell+1)}{2\ell+1} \right)^{\frac{1}{2}} Y_{\ell}^{-1} (U_{\frac{1}{2},\ell}^{\ell-\frac{1}{2}} - U_{\frac{1}{2},\ell}^{\ell+\frac{1}{2}}) \right] \chi_{\frac{1}{2}}^{\frac{1}{2}} \right]. \quad (C16)
 \end{aligned}$$

If we note that $Y_{\ell}^{-1} = -\exp(-2i\phi) Y_{\ell}^1$ the coefficients of $\chi_{\frac{1}{2}}^{\pm\frac{1}{2}}$ in equation (C16) are similar to those in equation (C15). Thus

$$2kf_{\frac{1}{2}}^{-\frac{1}{2}} = f_c \chi_{\frac{1}{2}}^{-\frac{1}{2}} - \exp(-2i\phi) f_i \chi_{\frac{1}{2}}^{\frac{1}{2}}. \quad (C16a)$$

Since the spin functions χ_s^v are orthonormal and both $f_{\frac{1}{2}}^{\pm\frac{1}{2}}$ contribute equally to the cross section, equation (C12) becomes

$$\sigma_{\alpha\alpha}(\theta) = \frac{1}{2} \sum_v |f_{\frac{1}{2}}^v|^2 = \frac{1}{4k^2} [|f_c|^2 + |f_i|^2]. \quad (C12a)$$

For the general case (inelastic and elastic scattering), the collision function $U_{\frac{1}{2},\ell}^J$ can be written

$$U_{\frac{1}{2},\ell}^{\ell\pm\frac{1}{2}} = \alpha^{\pm} \exp[2i(\omega_{\alpha} + \delta_{\ell}^{\pm})]$$

where α and δ are the imaginary and real parts, respectively, of the phase shift. For elastic scattering $\alpha^\pm = 1$ and thus

$$f_c = -\eta \csc^2(\tfrac{1}{2}\theta) \exp[i\eta \log \csc^2(\tfrac{1}{2}\theta)] + 2 \sum_{\ell} P_{\ell}(\cos \theta) \exp(2i\omega_{\ell}) \times [(\ell+1) \exp(i\delta_{\ell}^+) \sin \delta_{\ell}^+ + \ell \exp(i\delta_{\ell}^-) \sin \delta_{\ell}^-] \quad (C17)$$

$$f_i = 2 \sum_{\ell} P'_{\ell}(\cos \theta) \exp(2i\omega_{\ell}) [\exp(i\delta_{\ell}^+) \sin \delta_{\ell}^+ - \exp(i\delta_{\ell}^-) \sin \delta_{\ell}^-]. \quad (C18)$$

In equations (C17) and (C18) use was made of the following:

$$Y_{\ell}^0 = \left(\frac{2\ell+1}{4\pi}\right)^{\frac{1}{2}} P_{\ell}(\cos \theta)$$

$$Y_{\ell}^1 = -\left[\frac{2\ell+1}{4\pi\ell(\ell+1)}\right]^{\frac{1}{2}} \sin \theta \frac{dP_{\ell}(\cos \theta)}{d(\cos \theta)} = \left[\frac{2\ell+1}{4\pi\ell(\ell+1)}\right]^{\frac{1}{2}} P'_{\ell}(\cos \theta)$$

$$P'_{\ell}(\cos \theta) = \frac{dP_{\ell}(\cos \theta)}{d\theta}$$

$P_{\ell}(\cos \theta)$ = Legendre polynomial of order ℓ .

2. Spin Polarization Equations⁹³⁾

In order to obtain a system that is either partially polarized or unpolarized, the spin states must be added incoherently, i.e., the probabilities rather than the amplitudes are additive. For a system of partially polarized spin $\frac{1}{2}$ particles the polarization along a given axis is defined as the difference between the normalized probabilities of finding polarization parallel or anti-parallel to that axis.

Normally for a system of spin $\frac{1}{2}$ -particles the spin state is taken as $\begin{pmatrix} a_n \\ b_n \end{pmatrix}$ and is a superposition of n spin states, each of which can be represented by a Pauli spinor. In view of the definition of the coherent f_c and incoherent f_i scattering amplitudes given in Appendix C, $\begin{pmatrix} f_c \\ f_i \end{pmatrix}$ equally well defines the spin state. The probability amplitudes for finding the spin in the $\pm z$ direction are, respectively

$$\begin{pmatrix} 1 & 0 \end{pmatrix} \begin{pmatrix} f_c \\ f_i \end{pmatrix} = f_c$$

$$\begin{pmatrix} 0 & 1 \end{pmatrix} \begin{pmatrix} f_c \\ f_i \end{pmatrix} = -f_i.$$

Thus the polarization along the z axis is

$$P_z = \frac{|f_c|^2 - |f_i|^2}{|f_c|^2 + |f_i|^2}.$$

In a similar manner the probability amplitudes for spin along $\pm x$ are

$$\begin{pmatrix} 1 & \pm 1 \end{pmatrix} \begin{pmatrix} f_c \\ f_i \end{pmatrix} = (f_c \pm f_i).$$

Then the polarization along the x axis is

$$P_x = \frac{|f_c + f_i|^2 - |f_c - f_i|^2}{|f_c + f_i|^2 + |f_c - f_i|^2} = \frac{2\text{Re}(f_c^* f_i)}{|f_c|^2 + |f_i|^2}.$$

The probability amplitudes for spin along $\pm y$ are

$$(1 \mp i) \begin{pmatrix} f_c \\ f_i \end{pmatrix} = (f_c \mp if_i)$$

and the polarization along y is

$$P_y = \frac{|f_c - if_i|^2 + |f_c + if_i|^2}{|f_c - if_i|^2 + |f_c + if_i|^2} = \frac{2\text{Im}(f_c^* f_i)}{|f_c|^2 + |f_i|^2} . \quad (\text{C19})$$

The Basel Convention⁴⁾ defines the direction of the polarization of the scattered particles as being perpendicular to the scattering plane. (See equation (B2) and Figure 15.) Traditionally the z axis is taken as the beam axis and if the x axis is chosen to lie in the scattering plane the y axis is then parallel to the polarization vector \hat{P} in Figure 15. This convention was followed in the present work, hence equation (C19) gives the magnitude of the polarization.

APPENDIX D. SINGLE LEVEL PARAMETERIZATION OF THE PHASE SHIFTS

This appendix is based on a computer program STARS written by Dr. E. V. Hungerford of Rice University and is essentially a description of the computational method employed by that program. Since no usage document or formal program writeup existed for STARS, this Appendix was written to meet that need as well as to explain the method employed in deriving a fit to the experimental ^3He - ^4He elastic scattering phase shifts.

The formulation of the problem is given in three main sources, Lane and Thomas,⁸²⁾ Jackson and Blatt,⁸³⁾ and Buck et al.,⁸⁴⁾ which will be referenced as necessary to denote the origin of equations and computational techniques. First, the variational method for determining the theoretical phase shifts will be given. Then the method of solving the Schroedinger equation, calculation of Coulomb functions, and equations used to compute the phase shifts will be presented.

1. Variational Method for Determining the Theoretical Phase Shifts

The program will vary any selected combination of the three resonance parameters reduced width γ^2 , resonance energy E_R , and nuclear reaction radius r to fit theoretically determined phase shifts to experimental phase shifts. Required input information consists of the experimental phase shifts and their corresponding energy values, a weighting

factor for each phase shift, the χ -value, and several control parameters. The termination conditions must be specified and may be either a maximum number of iterations or a χ^2 per data point which must be met.

First a set of theoretical phase shifts $\vec{\theta}^{(1)}$ is computed using the initial conditions \vec{P} . \vec{P} is an N-dimensional vector containing the initial values of the N parameters to be varied, where $1 \leq N \leq 3$. \vec{P} is of the form

$$\vec{P} = \vec{P}(x)$$

where x represents any combination of the parameters γ^2 , E_R , and r. To be consistent with the iterative nature of the calculations, the superscript on $\vec{\theta}^{(1)}$ will be changed to (n) to denote the value of the vector \vec{P} from which $\vec{\theta}$ was computed. Thus for the n^{th} calculation of the theoretical phase shifts the notation is

$$\vec{\theta}^{(n)}(\vec{P}^{(n)}) . \quad (D1)$$

Note that $\vec{\theta}^{(n)}$ is an E-dimensional vector where E is the number of experimental phase shifts.

Next, in order to calculate a derivative, a single component i of $\vec{P}^{(n)}$ is perturbed by an amount

$$\Delta P_i^{(n)} = P_i^{(n)} S_i \quad (D2)$$

where S_i is the variational step size for parameter i (one of the varied parameters γ^2 , E_R , or r). A new set of theoretical phase shifts is computed using the vector

$$\vec{p}'^{(n)} = \vec{p}^{(n)} + \Delta \vec{p}^{(n)}.$$

Note that all other $N-1$ components of $\vec{p}^{(n)}$ are unaltered. This procedure is repeated for all N parameters, resulting in N sets of theoretical phase shifts computed from perturbed parameters. These are collected to form a matrix of dimension $N \times E$, and denoted by

$$\underline{\theta}'^{(n)}(\vec{p}'^{(n)}).$$

The derivative matrix \underline{F} can now be found. The ij element of \underline{F} is

$$F_{ij} = \frac{\theta'_{ij}^{(n)} - \theta_j^{(n)}}{\Delta p_i^{(n)}}.$$

Next, the matrix \underline{B} is computed, an element of which is

$$B_{ij} = \sum_{k=1}^E \frac{F_{ik} F_{jk}}{W_k^2}.$$

Note that \underline{B} is just the matrix product of \underline{F} with \underline{F} transpose where each element in \underline{F} and \underline{F} transpose has been normalized by the weighting factor W_k corresponding to each experimental phase shift. ($W_k = 1$ for all k was used in this analysis.) The dimension of \underline{F} is $N \times E$ and that of \underline{B} is N^2 .

An N -dimensional vector \vec{A} is formed as follows

$$A_j = \sum_{k=1}^E \frac{[\theta_{jk}^{(n)} - \theta_k^{(n)}]}{\Delta P_j^{(n)}} \frac{[\theta_k^{(n)} - \theta_k^{(e)}]}{W_k^2}$$

$$A_j = \sum_{k=1}^E F_{jk} \frac{[\theta_k^{(n)} - \theta_k^{(e)}]}{W_k^2}$$

where the $\theta_k^{(e)}$ are the experimental phase shifts. The matrix \underline{B} is inverted by the Crout method⁹⁴⁾ and from \underline{B}^{-1} and \vec{A} the perturbation vector is computed:

$$\Delta P_j^{(n+1)} = \sum_{k=1}^E B_{jk}^{-1} A_k.$$

In matrix notation this is

$$\Delta \vec{P}^{(n+1)} = \underline{B}^{-1} \vec{A}.$$

$\Delta \vec{P}^{(n+1)}$ will be used as the variation of $\vec{P}^{(n)}$ from which the phase shifts for the next iteration will be determined if for all parameters varied i ,

$$S_i \geq S_i' \quad (D3)$$

where

$$S_i' = \left| \frac{\Delta P_i^{(n+1)}}{P_i^{(n)}} \right|. \quad (D4)$$

In this case

$$\vec{P}^{(n+1)} = \vec{P}^{(n)} - \Delta \vec{P}^{(n+1)}. \quad (D5)$$

If equation (D3) does not hold for any i , i.e., if

$$S_i < S'_i$$

then the quantity

$$y = |S_k/S'_k|,$$

where S'_k is the largest of the N values of S'_i given by equation (D4), is used to modify $\vec{\Delta P}^{(n+1)}$. The vector $\vec{P}^{(n+1)}$ in this case is

$$\vec{\Delta P}^{(n+1)} = \vec{P}^{(n)} - y\vec{\Delta P}^{(n+1)}. \quad (D5a)$$

This has the effect of reducing the magnitude of the variation since $y < 1$. Thus the variation on \vec{P} for the next iteration is determined by the larger of the pair S_k, S'_k . This procedure prevents the step size for any parameter i from exceeding the maximum initial value specified for any of the N parameters being varied.

Using the vector $\vec{P}^{(n+1)}$, equation (D5) or equation (D5a), an updated set of phase shifts is computed, analogous to $\vec{\theta}^{(n)}(\vec{P}^{(n)})$, equation (D1).

$$\vec{\theta}^{(n+1)}(\vec{P}^{(n+1)}) \quad (D1a)$$

Then χ^2 per data point is computed using the latest phase shifts:

$$\frac{\chi^2}{E} = \frac{1}{E} \sum_{j=1}^E \left(\frac{\theta_j^{(e)} - \theta_j^{(n+1)}}{W_j} \right)^2$$

If $\chi^2/E \leq \epsilon$, the termination tolerance, or if the maximum number of iterations has been achieved, the values of the

phase shifts given by equation (D1a) are accepted and the program expects more data for a subsequent case. If neither termination condition is met, another iteration is performed beginning at equation (D2) with $\Delta P_i^{(n)}$ replaced by $\Delta P_i^{(n+1)}$ or $y\Delta P_i^{(n+1)}$. This procedure is repeated until a termination criterion is met.

2. Calculation of the Phase Shifts from the Parameter Vector

$\vec{P} = \vec{P}(\gamma^2, E_R, r)$ and the Solutions to the Schroedinger Equation

a. Solutions to the Schroedinger Equation

In order to calculate the theoretical phase shifts for a given ℓ -value and energy, the solutions to the radial part of the Schroedinger equation must be determined:

$$\left[\frac{d^2}{d\rho^2} - \frac{\ell(\ell+1)}{\rho^2} + \frac{2\eta}{\rho} \right] U(\rho) = 0$$

where ρ , η , ℓ , and $U(\rho)$ were defined in Appendix C. The asymptotic solutions are of the form

$$\begin{aligned} F_0(\rho) &\sim \sin(\rho - \eta \log 2\rho - \frac{1}{2}\ell\pi + \delta_\ell) \\ G_0(\rho) &\sim \cos(\rho - \eta \log 2\rho - \frac{1}{2}\ell\pi + \delta_\ell) \end{aligned}$$

where $F(\rho)$ is regular at the origin and $G(\rho)$ is irregular and δ_ℓ is the Coulomb phase shift for relative angular momentum ℓ . Three distinctions are made in the manner in which the solutions to the Schroedinger equation are determined.

(1). Vanishing Coulomb Field

First we consider the case of the vanishing Coulomb field, $\eta = 0$, for which the irregular solutions with $\ell = 0$ are spherical Bessel and Neumann functions.

$$\begin{aligned} G_0(\rho) &= \cos \rho \\ G'_0(\rho) &= -k \sin \rho \end{aligned}$$

Using equations given by Buck et al.,⁸⁴⁾ the regular functions $F_\ell(\rho)$ are computed downward in ℓ using the recursion relation (D6) known as Miller's method. For some large $\ell > \ell_{\max}$, $F_{\ell+1}(\rho) = 0$ and $\alpha F_\ell(\rho) = \epsilon$, where ϵ is a very small number and α is a constant yet to be determined.

$$\begin{aligned} F_{\ell-1}(\rho) &= \frac{\ell}{(\eta^2 + \ell^2)^{\frac{1}{2}}} \left\{ (2\ell+1) \left[\frac{\ell}{\ell(\ell+1)} + \frac{1}{\rho} \right] F_\ell(\rho) \right. \\ &\quad \left. - \frac{[\eta^2 + (\ell+1)^2]^{\frac{1}{2}}}{\ell+1} F_{\ell+1}(\rho) \right\} \end{aligned} \quad (D6)$$

Here ℓ_{\max} was taken as 26, $F_{\ell+1}(\rho) = F_{31}(\rho) = 0$, and $F_\ell(\rho) = F_{30}(\rho) = 10^{-38}$. With all the $F_\ell(\rho)$ down to $F_0(\rho)$ so determined, $F'_0(\rho)$ can be found from

$$F'_0(\rho) = k \left[\left(\eta + \frac{1}{\rho} \right) F_0(\rho) - (\eta^2 + 1)^{\frac{1}{2}} F_1(\rho) \right].$$

The constant α must satisfy the Wronskian

$$\alpha = \frac{k}{F'_0(\rho) G_0(\rho) - F_0(\rho) G'_0(\rho)}.$$

The $F_\ell(\rho)$ are each multiplied by α for all ℓ up through ℓ_{\max}

where ℓ_{\max} is that value of ℓ for which $\alpha F_{\ell_{\max}}(\rho) < 10^{-35}$ and $\alpha F_{\ell_{\max}-1}(\rho) \geq 10^{-35}$.

Sufficient information is now available to determine $F'_{\ell}(\rho)$, $G_{\ell}(\rho)$, and $G'_{\ell}(\rho)$, where $1 \leq \ell \leq \ell_{\max}$ and ℓ_{\max} was defined at the end of the preceding paragraph. Between equations (D6) and (D7) the term in $F_{\ell+1}$ can be eliminated

$$\left[\frac{\eta}{\ell+1} + \frac{\ell+1}{\rho}\right]F_{\ell}(\rho) - F'_{\ell}(\rho) = \frac{[\eta^2 + (\ell+1)^2]^{\frac{1}{2}}}{\ell+1} F_{\ell+1}(\rho) \quad (D7)$$

to give $F'_{\ell}(\rho)$ as a function of $F_{\ell-1}(\rho)$ and $F_{\ell}(\rho)$,

$$F'_{\ell}(\rho) = \frac{(\eta^2 + \ell^2)^{\frac{1}{2}}}{\ell} F_{\ell-1}(\rho) - \left(\frac{\eta}{\ell} + \frac{\ell}{\rho}\right)F_{\ell}(\rho). \quad (D8)$$

The $G_{\ell}(\rho)$ and $G'_{\ell}(\rho)$ obey the same recursion relations as the $F_{\ell}(\rho)$ and $F'_{\ell}(\rho)$, with $F_{\ell}(\rho)$ replaced by $G_{\ell}(\rho)$ and $F'_{\ell}(\rho)$ by $G'_{\ell}(\rho)$. Thus equation (D8) gives $G'_{\ell}(\rho)$ and equation (D7) can be solved to yield $G_{\ell+1}(\rho)$. Since $F_0(\rho)$, $F'_0(\rho)$, $G_0(\rho)$, and $G'_0(\rho)$ have been previously determined, the required functions can be generated for increasing values of ℓ . For each ℓ -value the following Wronskian must be satisfied to within 10^{-4} :

$$F'_{\ell}(\rho)G_{\ell}(\rho) - F_{\ell}(\rho)G'_{\ell}(\rho) = 1.$$

If it is not satisfied the Coulomb functions are incorrect and an error message occurs. At this point it is up to the user to determine the cause of the difficulty and to correct it. If the Wronskian is satisfied for all ℓ up through ℓ_{\max} the theoretical phase shifts are calculated as outlined in Section D.1.

(2). Non-vanishing Coulomb Field and ρ Small

Second we consider the case of $\eta \neq 0$ and ρ small, $\rho \leq 0.1$.
If further

$$\tau \equiv \frac{r}{R} > 0.21,$$

where

$$R = \frac{\hbar^2}{2m_r e^2},$$

the functions $F(r)$ and $G(r)$ are calculated in the same manner as for $\eta \neq 0$ and $\rho \geq 0.1$ presented in Section D.2.a.(3).

If, on the other hand, $\rho \leq 0.1$ and

$$\tau \equiv \frac{r}{R} \leq 0.21$$

the functions $F(r)$ and $G(r)$ are calculated from formulas given by Jackson and Blatt:⁸³⁾

$$\begin{aligned} F_0(r) &= C\rho\{L_1(r) - \frac{\rho}{6}L_2(r) + \frac{\rho^4}{120}[\frac{10}{9}L_3(r) - \frac{1}{9}]\dots\} \\ G_0(r) &= \frac{1}{C}[H_1(r) - \frac{\rho}{2}M(r) + \frac{\rho^4}{24}N(r)] \\ &\quad + \frac{1}{C}h(\eta)\tau\{L_1(r) - \frac{\rho}{6}L_2(r) + \frac{\rho^4}{120}[\frac{10}{9}L_3(r) - \frac{1}{9}] - \dots\} \end{aligned}$$

where

$$\begin{aligned} L_1(r) &= 1 + \frac{\tau}{2} + \frac{\tau^2}{12} + \frac{\tau^3}{144} + \dots \\ L_2(r) &= 1 + \frac{\tau}{3} + \frac{\tau^2}{24} + \frac{\tau^3}{360} + \dots \\ L_3(r) &= 1 + \frac{\tau}{4} + \frac{\tau^2}{40} + \frac{\tau^3}{720} + \dots \end{aligned}$$

$$H_1(r) = 1 + T(\log T + 2\eta - 1) + \frac{T^2}{2}(\log T + 2\eta - \frac{5}{2}) \\ + \frac{T^3}{12}(\log T + 2\eta - \frac{10}{3}) + \dots$$

$$H_2(r) = 1 - T - \frac{T^2}{2}(\log T + 2\eta - \frac{3}{2}) - \frac{T^3}{6}(\log T + 2\eta - \frac{17}{6}) \dots$$

$$H_3(r) = 1 - \frac{T}{2} + \frac{T^2}{4} + \frac{T^3}{12}(\log T + 2\eta - \frac{11}{6}) + \dots$$

$$H_4(r) = 1 - \frac{T}{3} + \frac{T^2}{12} - \frac{T^3}{36} + \dots$$

$$M(r) = \frac{2}{3T}[L_1(r) - H_2(r)]$$

$$N(r) = \frac{4}{3T}\{L_2(r) + \frac{2}{T}H_3(r) + \frac{12}{5T^2}[H_4(r) - L_1(r)]\}$$

$$C = \frac{2\pi\eta}{\exp(2\pi\eta) - 1}$$

$$h(\eta) = \eta^2 \sum_{n=1}^N \frac{1}{n(n^2 + \eta^2)} - \log \eta - \gamma$$

In the equation for $h(\eta)$ N is that value of n for which

$$\left| 1 - \frac{\sum_{i=1}^{n-1} \frac{1}{i(i^2 + \eta^2)}}{\sum_{j=1}^n \frac{1}{j(j^2 + \eta^2)}} \right| \leq 10^{-4}$$

and $\gamma = 0.57722$ = Euler's constant.

In order to compute the derivatives $F'_0(r)$ and $G'_0(r)$, r is incremented by $\Delta r = 0.25$ fm and the procedure above repeated. Then

$$F'_0(r) = \frac{F_0(r+\Delta r) - F_0(r)}{k\Delta r}$$

$$G'_0(r) = \frac{G_0(r+\Delta r) - G_0(r)}{k\Delta r}.$$

The functions and their derivatives must then satisfy the Wronskian to within 10^{-4}

$$F'_0(r)G_0(r) - F_0(r)G'_0(r) = 1$$

and if they do, $G'_0(r)$ is multiplied by k . Then the remaining $F_\ell(\rho)$, $F'_\ell(\rho)$, $G_\ell(\rho)$, $G'_\ell(\rho)$ are computed beginning with equation (D6) of the preceding case ($\eta = 0$), Section D.2.a.(1). If the Wronskian is not satisfied, the procedure outlined in Section D.2.a.(3). is followed.

(3). Non-vanishing Coulomb Field and ρ Large

Third we consider the case of $\eta \neq 0$ and ρ large, $\rho \geq 0.1$. In this instance the Coulomb phase shifts δ_ℓ for large ℓ are

$$\begin{aligned} \delta_\ell(\eta) = & \phi(\ell + \frac{1}{2}) + \eta(\log \beta - 1) - \frac{1}{\beta} \left(\frac{\sin \phi}{12} - \frac{\sin 3\phi}{360\beta^2} \right. \\ & \left. + \frac{\sin 5\phi}{1260\beta^4} - \frac{\sin 7\phi}{1680\beta^6} + \frac{\sin 9\phi}{1188\beta^8} - \dots \right) \end{aligned} \quad (D9)$$

where

$$\phi = \tan^{-1} \left(\frac{\eta}{\ell+1} \right) \quad \text{and} \quad \beta = [\eta^2 + (\ell+1)^2]^{\frac{1}{2}}.$$

For $\ell = 50$ equation (D9) is used to compute δ_{50} and then the recursion relation

$$\delta_\ell(\eta) = \delta_{\ell+1} - \tan^{-1} \left(\frac{\eta}{\ell+1} \right)$$

allows the remaining phase shifts down to δ_0 to be determined.

The irregular functions $G_0(\rho)$ and $G'_0(\rho)$ are now calculated as follows

$$\begin{aligned} G_0(\rho) &= s \cos \theta - t \sin \theta \\ G'_0(\rho) &= S \cos \theta - T \sin \theta \end{aligned} \quad (D10)$$

where

$$\theta = -\eta \log 2\rho + \rho + \delta_0 \quad (D11)$$

and

$$s = \sum_{n=0}^{19} s_n, \quad t = \sum_{n=0}^{19} t_n, \quad S = \sum_{n=0}^{19} S_n, \quad T = \sum_{n=0}^{19} T_n. \quad (D12)$$

The individual terms appearing in the sums of equations (D12) are found from the following recursion relations starting with $r = r_0 + 0.1$, where r_0 is the initial radius:

$$\begin{aligned} s_{n+1} &= A_n s_n - B_n t_n, & t_{n+1} &= A_n t_n + B_n s_n, \\ S_{n+1} &= A_n S_n - B_n T_n - \frac{s_{n+1}}{\rho}, & T_{n+1} &= A_n T_n + B_n S_n - \frac{t_{n+1}}{\rho} \end{aligned}$$

with

$$A_n = \frac{(2n+1)\eta}{2\rho(n+1)}, \quad B_n = \frac{n^2 - n(n+1)}{2\rho(n+1)},$$

and the initial values

$$\begin{aligned} s_0 &= 1, & s_1 &= \frac{\eta}{2\rho}, & t_0 &= 0, & t_1 &= \frac{\eta^2}{2\rho}, \\ S_0 &= 0, & S_1 &= \frac{\eta^3 - \eta^2}{2\rho^2} - \frac{\eta}{2\rho^2}, & T_0 &= 1 - \frac{\eta}{\rho}, & T_1 &= \frac{-\eta^2}{\rho^2} + \frac{\eta}{2\rho}. \end{aligned}$$

The sums were required to satisfy the Wronskian to within 10^{-4}

$$sT - St = 1. \quad (D13)$$

If the Wronskian was not satisfied, a value of r given by

$$r = r_0 + 2 + 0.1$$

(in fm) is used and the sums recomputed using the new value of ρ . This procedure is repeated until the Wronskian is satisfied at some value

$$r = r_0 + 2m + 0.1 \quad (D14)$$

where m is the integral number of times r was incremented by 2 fm. At this point the value of r is in the asymptotic region. $G_0(\rho)$ and $G'_0(\rho)$ are now computed using equations (D10)-(D12).

Next with

$$r = r_0 + 2m \quad (D15)$$

the sums, equations (D12), are recomputed and the Wronskian, equation (D13), rechecked. Presumably r is large enough that the Wronskian will be satisfied on the first attempt. If it is not, the procedure resulting in $G_0(\rho)$ and $G'_0(\rho)$ at a value given by equation (D14) is repeated until r is large enough that the Wronskian will be satisfied at a value given by both equations (D14) and (D15). When this occurs, two pairs of values $G_0(\rho)$ and $G'_0(\rho)$ are computed. This is necessary because $G_0(\rho)$ and $G'_0(\rho)$ are to be numerically integrated backward from $r = r_0 + 2m$ to $r = r_0$.

The integration method employed is described by Fox and Goodwin⁹⁵⁾ and uses their recurrence relation, equation (D16). For $\ell = 0$, the Schroedinger equation is

$$\frac{d^2 u(\rho)}{d\rho^2} = \left(\frac{2\eta}{\rho} - 1\right)u(\rho)$$

or

$$y'' = fy$$

where

$$f = \left(\frac{2\eta}{\rho} - 1\right)$$

and the recurrence relation can be applied:

$$\left(1 - \frac{h^2}{12}f_1\right)y_1 = \left(2 + \frac{5h^2}{6}f_0\right)y_0 - \left(1 - \frac{1h^2}{12}f_{-1}\right)y_{-1} \quad (D16)$$

with $y_0 = G_0(r=r_0+2m)$ and $y_{-1} = G_0(r=r_0+2m+0.1)$. The error term Δ (not shown) is neglected over the range of integration considered here. The integration step size h is held constant at -0.1 fm and the subscripts on f denote three successive evaluations of

$$f = \frac{2\eta k}{r} - k^2$$

for contiguous values of r differing only by $\Delta r = 0.1$ fm.

Thus

$$f_1 = \frac{2\eta k}{r-\Delta r} - k^2, \quad f_0 = \frac{2\eta k}{r} - k^2, \quad f_{-1} = \frac{2\eta k}{r+\Delta r} - k^2.$$

Equation (D16) gives a new value of the function

$y_1 = y_1(r - \Delta r)$ starting with the values $y_0 = y_0(r)$ and $y_{-1} = y_{-1}(r + \Delta r)$. Decrementing r by Δr gives a new value of f_1 and the process can be repeated beginning with y_1 and y_0 . This procedure ultimately yields $y(r=r_0) = G_0(r=r_0)$. To

find $G'_0(r=r_0)$ the relation below is used.

$$G'_0(r_0) = G'_0(r+2m) - \frac{h}{3} \left[\sum_{n=1}^{10m} (4y_{2n-1}f_{2n-1} + 2y_{2n}f_{2n}) - G_0(r_0)f_{20m} \right]$$

In this equation

$$f_j = \frac{2\eta k}{r_0 + 2m - j\Delta r} - k^2$$

and $\Delta r = h = 0.1$, which gives

$$f_{20m} = \frac{2\eta k}{r_0 + 2m - 20m(0.1)} - k^2 = \frac{2\eta k}{r_0} - k^2.$$

The value of y in the relation for $G'_0(r_0)$ is

$$y_j = G_0(r=r_0 + 2m - j\Delta r).$$

At this point $G_0(r=r_0)$ and $G'_0(r=r_0)$ have been determined, and to obtain the remaining $G_\ell(r=r_0)$, $G'_\ell(r=r_0)$, and all the $F_\ell(r=r_0)$ and $F'_\ell(r=r_0)$, the procedure described for the case of $\eta = 0$ is used beginning with equation (D6), Section D.2.a.(1).

b. Calculation of Theoretical Phase Shifts

Lane and Thomas discuss extensively the relation between the collision function U and the R function. No attempt will be made here to repeat their derivation, but instead the results of their treatment will be briefly summarized to obtain the expression for the phase shifts.

The collision function U was defined in Appendix C as the amplitude of the unit flux outgoing wave associated with the unit flux incident wave. Essentially the R function takes account of all interactions occurring inside of nuclei, both

inside the compound nucleus and inside the nuclei of separated pairs. R is defined by

$$R = \sum_{\lambda} \gamma_{\lambda}^2 / (E_{\lambda} - E) \quad (D17)$$

where γ_{λ} is defined as a reduced width amplitude. At certain real energies E_{λ} the radial solutions U_{λ} to the Schroedinger equation will have a vanishing first derivative at the boundary $r = a$. These energies E_{λ} are the eigenvalues belonging to the eigenfunctions U_{λ} . In equation (D17) E is the excitation energy.

The collision function can be expressed in terms of the R function by requiring that the internal (u_{ℓ}) and external (I_{ℓ}, O_{ℓ}) wave functions and their first derivatives be continuous at the boundary $r = a$. Lane and Thomas accomplish this by equating the logarithmic derivatives at the boundary:

$$\frac{u_{\ell}}{\rho_{\ell} u'_{\ell}} = R_{\ell} = \frac{I_{\ell} - U_{\ell} O_{\ell}}{\rho_{\ell} (I'_{\ell} - U'_{\ell} O'_{\ell})} \quad (D18)$$

where I_{ℓ} and O_{ℓ} were defined in Appendix C as $I_{\alpha\ell}$ and $O_{\alpha\ell}$, equations (C4). Solving equation (D18) for U_{ℓ} yields

$$U_{\ell} = \frac{I_{\ell}}{O_{\ell}} \left(\frac{1 - L_{\ell}^* R_{\ell}}{1 - L_{\ell} R_{\ell}} \right) \quad (D19)$$

where

$$L_{\ell} = (\rho_{\ell} O'_{\ell} / O_{\ell})_{r=a} = S_{\ell} + iP_{\ell}$$

$$S_{\ell} = [\rho_{\ell} (F_{\ell} F'_{\ell} + G_{\ell} G'_{\ell}) / (F_{\ell}^2 + G_{\ell}^2)]_{r=a}$$

$$P_{\ell} = [\rho_{\ell} / (F_{\ell}^2 + G_{\ell}^2)]_{r=a}$$

The asterisk on L above denotes complex conjugation and the apostrophe on I_{ℓ} and O_{ℓ} denotes the first derivative with respect to r. Also only positive energy channels are considered in this discussion. S_{ℓ} and P_{ℓ} will be more fully defined in a subsequent paragraph.

In equation (D19) the term I_{ℓ}/O_{ℓ} can be easily put in the form

$$I_{\ell}/O_{\ell} = \exp[2i(\omega_{\ell} - \phi_{\ell})],$$

where

$$\phi_{\ell} = \tan^{-1}(F_{\ell}/G_{\ell}),$$

by using equations (C4) for I_{ℓ} and O_{ℓ} . In a similar manner the remaining factor in equation (D19) can be written

$$\frac{1 - L_{\ell}^* R_{\ell}}{1 - L_{\ell} R_{\ell}} = \exp(2i\beta_{\ell})$$

where

$$\beta_{\ell} = \tan^{-1} \left(\frac{R_{\ell} P_{\ell}}{1 - R_{\ell} S_{\ell}} \right).$$

The collision function is then written in terms of the phase shift θ_{ℓ} .

$$U_{\ell} = \exp(2i\theta_{\ell}) = \exp[2i(\beta_{\ell} - \phi_{\ell} + \omega_{\ell})]$$

In the foregoing results β_{ℓ} is known as the resonance

contribution to the phase shift and ϕ_ℓ is called the hard sphere scattering phase shift.

If the excitation energy E is close to one of the energy level positions E_λ the contribution to R_ℓ from all terms in equation (D17) except λ can be neglected. Thus

$$R_\ell \approx \gamma_{\lambda\ell}^2 / (E_\lambda - E)$$

and the one-level approximation for the phase shift θ_ℓ is

$$\theta_\ell = \tan^{-1} \left[\frac{\gamma_\ell^2 P_\ell / (F_\ell^2 + G_\ell^2)}{E_R - \gamma_\ell^2 P_\ell \frac{(F_\ell F'_\ell + G_\ell G'_\ell)}{(F_\ell^2 + G_\ell^2)} - E} \right] - \phi_\ell \quad (D20)$$

where E_R was used in place of E_ℓ to be consistent with the notation of Section III.B.3.

In equation (D20) the second term in the denominator is $-\gamma_\ell^2 S_\ell$ and represents the amount the resonance energy is shifted from the eigenvalue position E_λ , and is known as the shift factor. The numerator in equation (D20) is $\gamma_\ell^2 P_\ell$ and is equal to $\frac{1}{2}\Gamma_\ell$, the level width, which determines how fast the phase changes when E passes through the resonance energy at $E = E_R - \gamma_\ell^2 S_\ell$. P_ℓ is called the penetration factor because it represents the probability of a particle reaching the nuclear surface.

APPENDIX E. RESULTS OF SOME OPTICAL PUMPING TESTS ON CELLS
CONTAINING ALUMINUM AND BRASS PARTS

This experiment was originally planned to permit low energy scattering (≥ 3 MeV) scattering of ^3He and ^4He from a polarized ^3He target. The original target cell was designed with large angle windows which would have allowed scattered particles to be detected over the continuous laboratory angular range of 30° to 150° on both sides of the beam. Aluminum foil 0.15 mil thick was to have been used as the window material. Since such thin foils would not support a pressure differential of 1 atm the cell was to have been mounted inside a vacuum chamber which was designed and built for this purpose. Reference 1) gives a complete description of the cell and vacuum chamber. Unfortunately, this design did not work as planned.

The large angle cell had a brass center section and pyrex cylinders for ends. Indium gaskets were used between the pyrex and brass parts and between the foil windows and the brass center section. The cell was approximately 1 in. I.D. \times 3 in. tall and about 40% of its interior surface area was formed by aluminum foil and brass. Even though this cell could be made leak-free, polarization was never attained, apparently because the brass parts continued to outgas. The continuum in the discharge spectrum could never be completely eliminated. At one point during the attempted cleanup the cell showed a characteristic hydrogen discharge after it had been evacuated and left closed overnight. This was very

unusual in view of the fact that the assembled cell had never been in contact with hydrogen. The only possible explanation is that the stock from which the brass part was fabricated had at some time been placed in contact with hydrogen. It is known that hydrogen can be adsorbed in copper, a major constituent of brass.

Since the combination brass-glass cell would not polarize, some tests were performed to isolate the cause. A piece of aluminum foil comparable in size to the total used on the large angle cell above was sealed inside a spherical pyrex bulb. In a similar bulb a piece of brass from the same stock as the brass center section of the large angle cell was sealed. The surface area of the brass constituted about 40% of the combined interior surface area of the test cell and the enclosed brass sample. A third control cell was simultaneously tested with the two containing metal samples. The three were attached to the vacuum system and cleaned in a similar manner. All three cells were filled with approximately 4 torr of ^3He . The results were as follows. The polarization in the cell containing aluminum foil was optically measured at 5.4%, the cell containing brass would not polarize, and the polarization in the control cell was 7.6%. One other test was performed with a similar cell containing a brass sample comprising about 8% of the interior surface area of the cell and brass together. This brass sample was taken from the same stock as in the previous

test. This cell was cleaned and filled to about 4 torr of ^3He in the usual fashion and it attained 5.9% polarization.

These tests suggest two conclusions: The presence of brass or aluminum in contact with ^3He in an optical pumping environment has a detrimental effect on the maximum attainable polarization and the presence of brass with sufficiently large surface area in contact with ^3He in an optical pumping environment will entirely prevent polarization. These results stand in contrast to those of Phillips et al.⁶⁾ whose target cell was fabricated of brass walls with pyrex ends to permit passage of the ^4He pumping light. Their reported polarization of 8.5% (optically measured) was lower than the 10-15% obtained with cells made largely of pyrex. No definite explanation for their cell achieving polarization can be made; however, the volume of their cell was considerably larger than either the test cells or the large angle brass and pyrex cell. There is no evidence at this point to indicate that volume has any effect on polarization.

There appears to be little in the literature on the effects of various materials in contact with ^3He in an optical pumping cell. Gamblin and Carver⁹⁾ reported that mercury caused no noticeable change in the polarization but that in one test rubidium significantly decreased the spin lattice relaxation time and hence would reduce polarization. Colegrove et al.⁸⁾ report that experiments with aluminum foil, Havar foil,⁹⁶⁾ brass, and aluminum inside optical pumping cells had no serious effect on metastable relaxation

time. This latter report disagrees with the tests described in the preceding paragraphs.

The commercially available so-called nonferrous metals such as aluminum, brass, and copper contain from a fraction of a percent to 1% or 2% iron, depending on the alloy. This is a possible explanation of why the test cells containing these metals showed low or no polarization, since magnetic field gradients reduce metastable relaxation times, resulting in diminution of polarization.⁸⁾ An interesting study would be to test a wide range of truly nonferrous metal alloys in contact with ^3He in an optical pumping environment. Fitzsimmons et al.⁹⁷⁾ have reported such a study on various types of glass containers and they propose a model to explain their results.

APPENDIX F. ENERGY CALIBRATION FOR THE EXPERIMENT

A new 90° energy analyzing magnet was installed on the 5.5 MeV Van de Graaff accelerator prior to performing this experiment. In order to calibrate the new magnet, the $^{40}\text{Ca}(p,p)^{40}\text{Ca}$ reaction was chosen since the energy of the sharp resonance at $E_p = 4.681$ MeV is accurately known. A nuclear magnetic resonance technique was used to measure the strength of the magnetic field. Calibration data were taken at 5 kHz intervals in the vicinity of the resonance, which represents energy intervals of less than 5 keV. The uncertainty in the NMR frequency should be no more than a fraction of a percent, and it is thus estimated that the calibration energy is known to better than ± 5 keV.

It is known that the optics of the new magnet system do not restrict the beam entering the magnet to a small ray which is truly vertical at all energies. (The exit beam is in the horizontal direction.) It is estimated that the entering beam can be off the vertical by not more than 2°. If for a magnetic field B particles of energy E are deflected exactly 90°, then for particles to undergo a deflection of $90^\circ \pm 2^\circ$ the bombarding energy E would have to change by $\Delta E = \pm 12$ keV.

It is then concluded that the new magnet system can define the bombarding energy to better than ± 20 keV, which will be quoted as the energy uncertainty for this experiment.

REFERENCES

1. W. R. Boykin, M. A. Thesis, Rice University, unpublished (1968)
2. P. D. Miller and G. C. Phillips, Phys. Rev. 112, 2048 (1958)
3. G. C. Phillips and P. D. Miller, Phys. Rev. 115, 1268 (1959)
4. Proceedings of the First International Symposium on the Polarization Phenomena of Nucleons, Basel, 1960, Ed. P. Huber and K. P. Meyer, Helv. Phys. Acta, Suppl. 6, 436 (1961)
5. R. Chiba, H. E. Conzett, H. Morinaga, N. Mutsuro, K. Shoda, and M. Kimura, Bull. Amer. Phys. Soc. 3, 419 (1958)
6. G. C. Phillips, R. R. Perry, P. M. Windham, G. K. Walters, L. D. Schearer, and F. D. Colegrove, Phys. Rev. Lett. 9, 502 (1962)
7. G. K. Walters, F. D. Colegrove, and L. D. Schearer, Phys. Rev. Lett. 8, 439 (1962)
8. F. D. Colegrove, L. D. Schearer, and G. K. Walters, Phys. Rev. 132, 2561 (1963)
9. R. L. Gamblin and T. R. Carver, Phys. Rev. 138, A946 (1965)
10. T. A. Tombrello and P. D. Parker, Phys. Rev. 130, 1112 (1963)
11. H. D. Holmgren and K. L. Johnson, Phys. Rev. 113, 1556 (1959)
12. P. D. Parker and R. W. Kavanagh, Phys. Rev. 131, 2578 (1963)
13. T. A. Tombrello and P. D. Parker, Phys. Rev. 131, 2582 (1963)
14. K. Nagatani, M. R. Dwarakanath, and D. Ashery, Nucl. Phys. A128, 325 (1969)
15. A. C. L. Barnard, C. M. Jones, and G. C. Phillips, Nucl. Phys. 50, 629 (1964)
16. R. J. Spiger and T. A. Tombrello, Phys. Rev. 163, 964 (1967)

17. M. Ivanovich, P. G. Young, and G. G. Ohlsen, Nucl. Phys. A110, 441 (1968)
18. P. Schwandt, B. W. Ridley, S. Hayakawa, L. Put, and J. J. Kraushaar, Phys. Lett. 30B, 30 (1969)
19. A. D. Bacher, H. E. Conzett, R. de Swiniarski, H. Meiner, F. G. Resmini, and T. A. Tombrello, Bull. Amer. Phys. Soc. 14, 851 (1969)
20. C. G. Jacobs, Jr., and R. E. Brown, Phys. Rev. C 1, 1615 (1970)
21. R. E. Brown, E. E. Gross, and A. van der Woude, Phys. Rev. Lett. 25, 1346 (1970)
22. J. S. Vincent, E. T. Boschitz, and R. E. Warner, Bull. Amer. Phys. Soc. 12, 17 (1967)
23. T. A. Cahill and P. C. Martens, Bull. Amer. Phys. Soc. 14, 553 (1969)
24. D. D. Armstrong, L. L. Catlin, P. W. Keaton, Jr., and L. R. Veaser, Phys. Rev. Lett. 23, 135 (1969)
25. D. M. Hardy, R. J. Spiger, S. D. Baker, Y. S. Chen, and T. A. Tombrello, Phys. Lett. 31B, 355 (1970)
26. D. M. Hardy, R. J. Spiger, S. D. Baker, Y. S. Chen, and T. A. Tombrello, to be published. This report will contain a more complete analysis of the data reported in reference 25).
27. W. R. Boykin, D. M. Hardy, and S. D. Baker, Proceedings of the Third International Symposium on the Polarization Phenomena of Nucleons, Madison, 1970, to be published. See also Bull. Amer. Phys. Soc. 15, 1694 (1970). These two references are preliminary reports of the present work. A more complete report has been prepared for publication.
28. W. S. McEver, T. B. Clegg, J. M. Joyce, E. J. Ludwig, and R. L. Walter, Phys. Lett. 31B, 560 (1970)
29. G. C. Phillips, Proceedings of the Second International Symposium on the Polarization Phenomena of Nucleons, Karlsruhe, 1965, Ed. P. Huber and H. Schopper (Birkhauser Verlag, Basel und Stuttgart, 1966)
30. W. M. Good, W. E. Kunz, and C. D. Moak, Phys. Rev. 83, 845 (1951)
31. E. Almqvist, K. W. Allen, J. T. Dewan, and T. P. Pepper, Phys. Rev. 91, 1022 (1953)

32. W. M. Good, W. E. Kunz, and C. D. Moak, Phys. Rev. 94, 87 (1954)
33. D. J. Bredin, J. B. A. England, D. Evans, J. S. C. McKee, P. V. March, E. M. Mosinger, and W. T. Toner, Proc. Roy. Soc. (London) A258, 202 (1960)
34. B. H. Bransden and R. A. H. Hamilton, Proc. Phys. Soc. 76, 987 (1960)
35. J. L. Gammel, J. E. Brolley, Jr., L. Rosen, and L. Stewart, Proceedings of the First International Conference on Nuclear Structure, Ed. D. Bromley (Univ. of Toronto Press, 1960) pp. 215-217
36. W. T. Leland, J. E. Brolley, Jr., and L. Rosen, Bull. Amer. Phys. Soc. 10, 51 (1965)
37. T. A. Tombrello and A. D. Bacher, Phys. Rev. 130, 1108 (1963)
38. Van Nen-Min, V. N. Novatskii, G. M. Osetinsky, Tsen Nay-Gun, and I. A. Chepurchenko, Yadernaya Fizika (USSR) 3, 1064 (1966) (In Russian)
39. A. D. Bacher, T. A. Tombrello, E. A. McClatchie, and F. Resmini, Bull. Amer. Phys. Soc. 13, 1366 (1968)
40. A. D. Bacher, R. J. Spiger, and T. A. Tombrello, Nucl. Phys. A119, 481 (1968)
41. J. G. Jenkin, W. D. Harrison, and R. E. Brown, Phys. Rev. C 1, 1622 (1970)
42. R. W. Zurmuhle, Nucl. Phys. 72, 225 (1965)
43. J. P. Aldridge, III, B. H. Wildenthal, and D. H. Youngblood, Revs. Mod. Phys. 37, 430 (1965)
44. A. D. Bacher and T. A. Tombrello, Revs. Mod. Phys. 37, 433 (1965)
45. E. W. Blackmore and J. B. Warren, Phys. Rev. Lett. 16, 520 (1966)
46. E. W. Blackmore and J. B. Warren, Canad. J. Phys. 46, 233 (1968)
47. W. D. Harrison, W. E. Stephens, T. A. Tombrello, and H. Winkler, Phys. Rev. 160, 752 (1967)
48. K. P. Artjomov, V. J. Chuev, V. Z. Goldberg, A. A. Ogloblin, V. P. Rudakov, and J. N. Serikov, Phys. Lett. 12, 53 (1964)

49. R. J. Slobodrian, J. S. C. McKee, W. F. Tivol, D. J. Clark, and T. A. Tombrello, Phys. Lett. B25, 19 (1967)
50. R. J. Slobodrian, J. S. C. McKee, D. J. Clark, W. F. Tivol, and T. A. Tombrello, Nucl. Phys. A101, 109 (1967)
51. T. A. Tombrello and R. J. Slobodrian, Nucl. Phys. A111, 236 (1968)
52. T. Lauristen and F. Azenberg-Selove, Nucl. Phys. 78, 1 (1966)
53. T. Teichmann and E. P. Wigner, Phys. Rev. 87, 123 (1952)
54. J. M. Daniels, Oriented Nuclei (Academic Press, New York, 1965)
55. R. A. Bernheim, Optical Pumping: An Introduction (W. A. Benjamin, Inc., New York, 1965)
56. W. A. Fitzsimmons and G. K. Walters, Phys. Rev. Lett. 19, 943 (1967)
57. L. D. Schearer, Ph. D. Thesis, Rice University, unpublished (1966)
58. L. D. Schearer and G. K. Walters, Phys. Rev. 139, A1398 (1965)
59. F. D. Colegrove and P. A. Franken, Phys. Rev. 119, 680 (1960)
60. M. A. Bouchiat, T. R. Carver, and C. M. Varnum, Phys. Rev. Lett. 5, 373 (1960)
61. F. D. Colegrove, L. D. Schearer, and G. K. Walters, Phys. Rev. 135, A353 (1964)
62. L. D. Schearer, F. D. Colegrove, and G. K. Walters, Phys. Rev. Lett. 10, 108 (1963)
63. R. C. Greenhow, Phys. Rev. 136, A660 (1960)
64. von U. Rohrer, P. Huber, C. Leeman, and H. Schieck, Helv. Phys. Acta 41, 436 (1968)
65. S. D. Baker, D. H. McSherry, and D. O. Findley, Phys. Rev. 178, 1616 (1969)
66. An oscillator which has been successfully used is described on drawing B452610, J. W. Miller Co., 5917 South Main, Los Angeles, Calif. 90003. It employs the Miller 4525 high voltage transformer. The drawing is supplied with the transformer.

67. D. O. Findley, M. A. Thesis, Rice University, unpublished (1967)
68. M. K. Salomaa, Nucl. Inst. and Methods 15, 113 (1962)
69. Type HR linear polarizer and 280-M optical retarder available from the Polaroid Corp., Rochester, N. Y.
70. Infrared detector available from Infrared Industries, Waltham, Mass.
71. D. H. McSherry, M. A. Thesis, Rice University, unpublished (1967)
72. Sentinel brand glass pipe, $\frac{1}{4}$ in. nominal I.D., available from Sentinel Glass Co., Hatboro, Pa.
73. Nuclear Data Tables, Part 3 (United States Atomic Energy Commission, 1960) p. 22
74. D. M. Hardy, M. A. Thesis, Rice University, unpublished (1968)
75. Indium wire available from Indium Corp. of America, Utica, N. Y.
76. J. B. Marion and F. C. Young, Nuclear Reaction Analysis, Graphs and Tables (North Holland Publishing Co., Amsterdam, 1968) pp. 15 and 19
77. L. C. Northcliffe, Phys. Rev. 120, 1744 (1960)
78. Tesla coil available from Electro Technic Products, Chicago, Ill. 60640
79. Rf energy source for cell cleanup, Raytheon Model CMD5 Diathermy Generator, 2450 MHz
80. ^3He obtained from Mound Laboratory, Miamisburg, Ohio
81. H. Cramér, Mathematical Methods of Statistics (Princeton University Press, Princeton, N. J., 1951) The likelihood function was also used by S. D. Baker and J. A. McIntyre, Phys. Rev. 161, 1200 (1967)
82. A. M. Lane and R. G. Thomas, Revs. Mod. Phys. 30, 257 (1958)
83. J. D. Jackson and J. M. Blatt, Revs. Mod. Phys. 22, 77 (1950)
84. B. Buck, R. N. Maddison, and P. E. Hodgson, Phil. Mag. 5, 1181 (1960)

85. Y. C. Tang, E. Schmid, and K. Wildermuth, Phys. Rev. 131, 2631 (1963)
86. D. R. Thompson and Y. C. Tang, Phys. Rev. 159, 806 (1967)
87. R. E. Brown and Y. C. Tang, Phys. Rev. 176, 1235 (1968)
88. D. H. McSherry, Ph. D. Thesis, Rice University, unpublished (1969)
89. L. Wolfenstein and J. Ashkin, Phys. Rev. 85, 947 (1952)
90. W. F. Rich, Ph. D. Thesis, Rice University, unpublished (1967)
91. L. I. Schiff, Quantum Mechanics (McGraw-Hill Book Co., Inc., New York, 1949) pp. 116-119
92. E. U. Condon and G. H. Shortley, The Theory of Atomic Spectra (Cambridge University Press, 1959) p. 76
93. S. DeBenedetti, Nuclear Reactions (John Wiley & Sons, New York, 1964) pp. 235-236
94. K. S. Kunz, Numerical Analysis (McGraw Hill Book Co., Inc., New York, 1957) pp. 235-237
95. L. Fox and E. T. Goodwin, Proc. Camb. Phil. Soc. 45, 373 (1949)
96. Havar foil is the trade name used by the Hamilton Watch Co, Lancaster, Pa., for a high tensile strength spring steel alloy.
97. W. A. Fitzsimmons, L. L. Tankersley, and G. K. Walters, Phys. Rev. 179, 156 (1969)

ACKNOWLEDGEMENTS

The author is grateful to Dr. G. C. Phillips for his role as research director on this project and wishes to thank him for his many contributions.

It is a pleasure to thank Dr. S. D. Baker for serving as thesis director and for his encouragement and guidance during both the experimental phase of the work and in the data analysis.

Appreciation is expressed to the Physics Department Shop personnel for constructing parts of the apparatus: Messrs. P. DeVries, J. Flick, and E. Harmening. Mr. Ed Preston of the Glass Shop constructed the pyrex target cell.

The author sincerely appreciates the fellowship aid provided by the United States Atomic Energy Commission.

Thanks are also due to the management of the NASA Manned Spacecraft Center for a leave of absence and in particular to Mr. M. T. Cunningham and Mr. E. H. Brock for their assistance in this matter. The use of the UNIVAC 1108 computer is appreciated.

The use of Dr. E. V. Hungerford's single level computer program STARS is acknowledged.

Gratitude is due my parents for their recognition of the value of education and for encouraging their children to continue in school.

To my family is due an especial "thank you" for their support and understanding. Without the assistance of my wife Mary Ann this work could not have been completed.